Role of Cytosolic Phospholipase $A_2\alpha$ in Neutrophil Chemotaxis

by

Fatima Javed

A dissertation submitted in partial fulfillment
of the requirements for the degree of
Doctor of Philosophy
(Cell and Developmental Biology)
in the University of Michigan
2023

Doctoral Committee:

Professor Billy Tsai, Chair
Professor Carole A. Parent
Professor Marc Peters-Golden
Professor Lois Wiesman

Fatima Javed

fjaved@umich.edu

ORCID iD: 0000-0002-5939-8039

Dedication

To my parents: Mama and Papa Javed:

Thank you for supporting me in this endeavor. You had only seen the negative side of doing a Ph.D. and did not know what it would entail, but you still supported me in chasing my passion for science and helped me through whenever I needed it.

To my brother and sister: Zain and Hoori:

As desi kids, we have a few cards that help us get our way with our parents. Thank you for using yours to help me convince mama and papa Javed to pursue this field. Thank you for always being there for me, listening to my rants, going off tangents, and helping me find papers and brainstorm ideas.

To my husband: Jeremy

Thank you for being there for me from the start of this adventure, picking me up when I was down, and celebrating the small wins throughout this journey, even when we were miles apart. I am genuinely grateful to have found you. I am super excited about the surprises that our next adventure in Milwaukee will bring.

Acknowledgments

First, I want to thank my mentor, Dr. Carole Parent, for her support and guidance throughout my Ph.D. career. Under your guidance, I learned how to think and work as an independent scientist. I am truly grateful for the opportunity you gave me by accepting me as a young graduate student in your lab. Thank you.

Second, thank you to all the friends I made during my graduate career. A special thank you to my closest friends Dr. Kenny Trieu, Cyrina Ostgaard, and Dr. Ashley Velez Delgado. My graduate school journey was made a whole lot better having you guys as my support.

I thank the members of the Parent Lab at the University of Michigan. To Peilin Shen – Peilin, you are the best lab manager! Thank you for everything that you do for us, from isolating neutrophils to keeping the lab stocked and booking a conference room for me whenever I wanted; thank you. To Dr. Shuvasree SenGupta – Sree, thank you for being my second mentor in the lab. Thank you for being there for me, listening to me, and advising me whenever I needed help. Thank you for not getting too annoyed with me when I asked 100 questions in a day. But most importantly, thank you for being a great friend and introducing me to masala chai and goose egg curry. To Dr. Lauren Hein – Lauren, we started our Ph.D. journey together, and are ending it together. This journey was made a whole lot better by having you by my side. Thank you for listening to my endless rants when the experiments decided not to work. Thank you for getting me into knitting and crocheting. I did not realize the amount of math that goes into it! To Kristen Loesel – Kristen, you joined the lab a year after I joined but quickly became a good friend. Thank you for making countless fiber mats for me, especially when troubleshooting that part of my

project. Thank you for helping me out whenever I needed it and sharing the cutest pictures and videos of your niece Amina. They always put a smile on my face! To Dr. Subhash Ayra – Subhash, thank you for teaching me how to do good science and sharing delicious meals with the lab. It is always fun talking with you about the food from our home countries. To Yang, I am so glad that doing your masters in our lab did not scare you away and that you decided to stay with us to continue your Ph.D. training. Thank you for sharing all the yummy Chinese treats with us during lab meetings. To Sam, thank you for teaching me what being a vegan means. It's not for me, but I learned a lot from you. Thank you for dropping everything and helping me analyze the microchannel data. I appreciate your help with that. You are going to be a senior grad student soon; I hope you enjoy your time here while doing good and rigorous science. Good Luck!

I also thank the members of my dissertation committee. Thank you for all the valuable input you have given me during my Ph.D. training. I am only here with your help and guidance.

Additionally, I thank Dr. Mara Duncan. Mara – I am grateful that you took a chance on a 22-year-old, fresh college graduate, taught her how to pipette correctly, and maintain sterility while doing bench science, and taught her how to clone. I have gotten pretty good at that! Thank you for teaching me how to think critically about science and considering our research when reading the journal articles.

I also thank my big sib – Jorge Y. Martínez Márquez. Jorge – thank you for being my mentor throughout my graduate career. Thank you for helping me troubleshoot cloning and listening to me rant whenever I have a terrible day. Thank you for being there for me. Also, thank you for including me in your family. Bárbara – you make the best cookies! You will always have me as a loyal customer, requesting to make cookies for all occasions.

A big thank you to the RELATE and Developing Future Biologists programs at the University of Michigan. Thank you for introducing me to science communication and how to apply it in life. I have learned so much from these programs in the two short years I was a part of these groups.

Finally, a huge thank you to the CDB administrative team. Thank you for all that you do behind the scenes for the department. Thank you for organizing and hosting different departmental events. It is always fun to see everyone together. A special thank you to Kristen Hug and Dr. Jacqueline Popma for always being there and helping me with anything I need. Thank you.

Table of Contents

List of Tables

List of Figures

Abstract

In the event of infection or injury, patrolling neutrophils directionally migrate to the inflamed or damaged site and initiate a dramatic swarm-like recruitment of distant neutrophils by secreting the secondary chemoattractant leukotriene B4 (LTB4) – a process knowns as a neutrophil signal relay. Studies from the Parent group have demonstrated that disruptions in LTB4 production, secretion, or sensing, lead to attenuated neutrophil response. In this context, I first studied how LTB4 is packaged in chemotaxing neutrophils. In collaboration with Dr. Subhash Arya (a post-doctoral fellow), I showed that LTB4-containing exosomes originate at ceramide-rich lipid-ordered microdomains at the nuclear envelope (NE). Additionally, I showed that these exosomes are distinct from the CD63-positive, canonical exosomes.

In this dissertation, I also investigated the role of cPLA2α in neutrophil chemotaxis. cPLA2α mediated arachidonic acid (AA) release is the rate-limiting step in LTB4 biogenesis. I found that inhibition or depletion of cPLA2α from the neutrophils significantly decreases LTB4 production. Using under agarose chemotaxis assays, I found that cPLA2α regulates neutrophil chemotaxis in a chemoattractant-dependent manner. I found that cPLA2α-/- cells have no defects in migration toward fMLF but have strong defects in migration toward C5a, LTB4, and IL-8.

Upon further investigation of the role of cPLA2α in neutrophil chemotaxis, I found that cPLA2α is localized to both the cytosol and nucleus of the neutrophil. Additionally, I demonstrated that cPLA2α is not involved in the generation of the ceramide-rich lipid-ordered microdomains or exosomes. It is, however, present in the exosomes and required for LTB4 generation. I also provide evidence and propose that the nuclear pool cPLA2α translocates to the immerging ILV and is

required for LTB4 generation. Finally, I discovered that cPLA2α regulated nuclear morphology in chemotaxing neutrophil-like cells and observed that the nuclei of cPLA2α-/- cells are unable to squeeze through tight (≤3μm) spaces. The doctoral research presented here reveals a novel mechanism by which LTB4-containing exosomes are generated and how cPLA2α mediates LTB4 production and illuminates the multiple functions of cPLA2α in neutrophil biology.

Chapter 1 The Multifaceted Functions of Cytosolic Phospholipase $A_2\alpha$

1.1 Introduction

Phospholipases (PL) are a superfamily of enzymes that catalyze the hydrolysis of cellular phospholipids. Phospholipids are the main components of cellular membranes and are composed of a triglyceride backbone, with two hydrophobic fatty acid chains attached to a hydrophilic phosphate head group. The PL superfamily is divided into five sub-groups based on the site of hydrolysis on the phospholipid backbone (Haas and Stanley 2007). Phospholipase A_1 (PLA1, Figure 1.1, blue), A_2 (PLA_2, Figure 1.1, grey), and B catalyze the hydrolysis of the fatty acid chains attached to the triglyceride at *sn-1, sn-2,* or both positions, respectively (Haas and Stanley 2007). On the other hand, Phospholipase C (PLC, Figure 1.1, orange) and D (PLD, Figure 1.1, gold) catalyze the hydrolysis at the phosphate group of the phospholipid (Haas and Stanley 2007). These PLAs perform various and diverse essential tasks in cells. Additionally, they mediate the generation of various bioactive lipids including, but not limited to, inositol-1-4-5-triphosphate (IP3), diacylglycerol (DAG) and arachidonic acid (AA) (Haas and Stanley 2007, Dennis, Cao et al. 2011, Stahelin 2016). In this chapter, I will focus on the functions of the PLA_2 class of phospholipase enzymes.

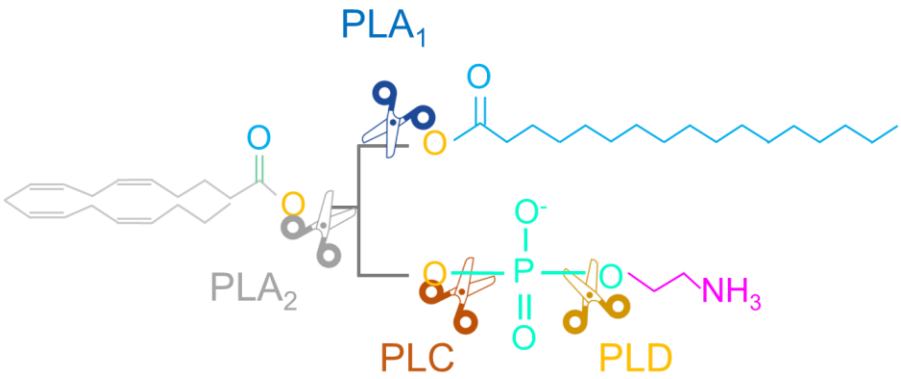

Figure 1.1: Sites of action of various phospholipase enzymes.

The structure of phosphatidylethanolamine (PE) with arachidonic acid at the *sn-2* position is shown with the sites of hydrolysis by PLA_1, PLA_2, PLC, and PLD enzymes. The PLB enzyme is not visualized here as this enzyme has both PLA_1 and PLA_2 activity.

1.2 Phospholipase A_2 (PLA_2) enzymes

The PLA_2 family of enzymes is divided into six diverse groups based on their characteristics (Burke and Dennis 2009). Groups I-III, V, IX-XIV are known as the Secretory PLA_2 ($sPLA_2$). Secretory PLA_2 are secreted outside cells and therefore act in the extracellular matrix (ECM) (Burke and Dennis 2009, Dennis, Cao et al. 2011). Group IV PLA_2 enzymes are known as the Cytosolic PLA2 ($cPLA_2$) enzymes. Their activities are calcium (Ca^{2+}) dependent. Calcium-independent PLA2 ($iPLA_2$) makes up group VI of PLA_2 enzymes. Unlike $cPLA_2$ enzymes, $iPLA_2$ enzymes do not require Ca2+ for activation. However, they are regulated by protein-protein interactions (Stahelin 2016). Group VII and VIII PLA_2 enzymes are called platelet-activating factor acetylhydrolase (PAF-AH). These enzymes are either secreted (Group VIIA) or act intercellularly (Group VIIB) (Stahelin 2016). Group XV PLA_2 enzymes have optimal enzymatic activity at pH 4.5 and have been reported to localize in the lysosome. Hence, this class of enzymes is called Lysosomal PLA_2 ($LPLA_2$) (Dennis, Cao et al. 2011). $LPLA_2$ enzymes are highly

expressed in alveolar macrophages and play a critical role in the hydrolysis and clearance of lung surfactants (Abe, Hiraoka et al. 2004, Stahelin 2016). Originally characterized as a tumor suppressor (Jin, Okamoto et al. 2007, Uyama, Morishita et al. 2009), Adipose-specific PLA_2 ($AdPLA_2$) was later characterized as Group GXVI PLA_2 enzyme (Duncan, Sarkadi-Nagy et al. 2008, Uyama, Morishita et al. 2009, Dennis, Cao et al. 2011), which is highly expressed in adipose tissue and adipocytes (Duncan, Sarkadi-Nagy et al. 2008) and have been reported to have both PLA_1 and PLA_2 activities (Uyama, Morishita et al. 2009). This information is summarized in Table 1.1.

Table 1.1.Phospholipase A_2 superfamily (adapted from (Dennis, Cao et al. 2011))

Type	Group	Subgroup	Molecular Mass (kDa)	Catalytic residues
$sPLA_2$	GI	A, B	13-15	His/Asp
	GII	A, B, C, D, E, F	13-17	
	GIII		15-18	
	GV		14	
	GIX		14	
	GX		14	
	GXI	A, B	12-13	
	GXII	A, B	19	
	GXIII		<10	
	GXIV		13-19	
$cPLA_2$	GIV	α, β, γ, δ, ε, ζ	60-114	Ser/Asp
$iPLA_2$	GVI	β, γ, δ, ε, ζ, η	85-90	Ser/Asp
PAF-AH	GVII	A (Lp- PLA_2) B (PAH-AH II)	40-45	Ser/His/Asp
	GVIII	α_1, α_2, β	26-40	
$LPLA_2$	GXV		45	Ser/His/Asp
$AdPLA_2$	GXVI		18	His/Cys

1.3 Cytosolic Phospholipase A_2

Members of the Cytosolic Phospholipase A_2 group have a high affinity for releasing arachidonic acid (AA) at the *sn-2* position of the triglyceride. AA is a precursor lipid to many inflammatory and anti-inflammatory bioactive lipids, including but not limited to leukotrienes and

prostaglandins. This group is further divided into six subtypes: cPLA$_2$α, cPLA$_2$β, cPLA$_2$γ, cPLA$_2$δ, cPLA$_2$ε, and cPLA$_2$ζ (Dennis, Cao et al. 2011; Leslie 2015). These isoforms share only 30% sequence homology with no redundancy in their activity known to date (Ohto, Uozumi et al. 2005, Leslie 2015). Except for cPLA$_2$γ, all cPLA$_2$ enzymes have an N-terminal, Ca^{2+} binding C2 domain and a C-terminal, α/β hydrolase domain containing the Serine (Ser)/Aspartic Acid (Asp) catalytic dyad (Figure 1.2) (Dessen, Tang et al. 1999). The two domains are connected by a small hinge region, allowing flexibility (Dessen, Tang et al. 1999). cPLA$_2$γ only contains the α/β hydrolase domain and hence is the only cPLA$_2$ isoform that is Ca2+ independent (Dessen, Tang et al. 1999). Table 1.2 summarizes the properties of the different cPLA$_2$ isoforms.

Table 1.2 summarizes the properties of the different cPLA$_2$ isoforms.

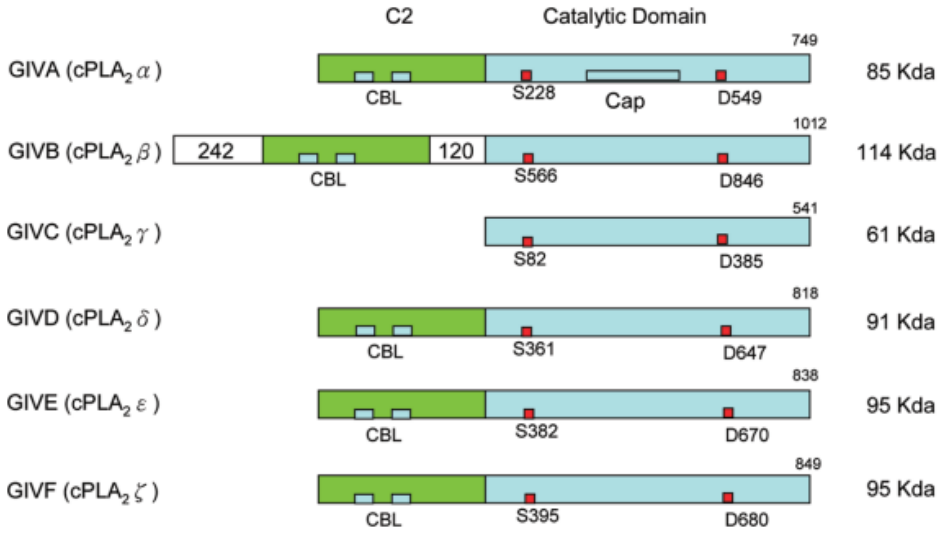

Figure 1.2: Schematic representation of Group IV cPLA$_2$s. Calcium binding loops (CBL) and active sites (red square) are shown (Dennis, Cao et al. 2011).

Table 1.2 Isoforms of $cPLA_2$ with their expression profiles, substrates, chromosomal localization, and genetic knockout mouse availability (Adapted from (Dennis, Cao et al. 2011))

$cPLA_2$ Isoform	**Most abundant expression tissue**	**Size (KDa)**	**Active site residues**	**Substrate**	**Chromosomal localization**	**Genetic knockout mouse available?**
$cPLA_2\alpha$	Ubiquitously expressed	85	Ser 228/ Asp 549	PC, PE, PI, high specificity towards *sn-2* AA	1q31.1	Yes
$cPLA_2\beta$	Pancreas, Liver, Heart, Brain	100-114	Ser 538/ Asp 566	PC, PE	15q15.1	No
$cPLA_2\gamma$	Heart, Skeletal muscle	61	Ser 82/ Asp 385	PC	19q13.33	No
$cPLA_2\delta$	Placenta	91	Ser 361/ Asp 647	PC, PE	15q15.1	No
$cPLA_2\varepsilon$	Heart, Skeletal muscle, Testis, Thyroid	95	Ser 383/ Asp 670	PC, PE	15q15.1	No
$cPLA_2\zeta$	Thyroid	95	Ser 395/ Asp 680	PC, PE	15q15.1	No

Of these isoforms, $cPLA_2\alpha$ has been most frequently studied as it is ubiquitously expressed in most human tissues (Dennis, Cao et al. 2011, Leslie 2015). $cPLA_2\alpha$ has been implicated in various cellular functions, including maintaining lipid homeostasis and membrane curvature (Leslie 2015), membrane trafficking (Brown, Chambers et al. 2003, Leslie, Gangelhoff et al. 2010), biogenesis of lipid droplets (Guijas, Rodriguez et al. 2014) and in the formation of lipid microdomains (Klapisz, Masliah et al. 2000, Guijas, Rodriguez et al. 2014). $cPLA_2\alpha$ has also been reported to be involved in various specialized functions in innate immune cells, such as degranulation and phagocytosis (Nakatani, Uozumi et al. 2000, Dabral and van den Bogaart 2021).

1.4 Structure and regulation of cPLA$_2$α

cPLA$_2$α was cloned and sequenced in 1991 (Sharp, White et al. 1991). There is ~95% homology in murine and human cPLA$_2$α suggesting similarities in function and regulation (Clark, Lin et al. 1991). cPLA$_2$α can hydrolyze phosphatidylinositol (PI), sphingolipids, and phosphatidylethanolamine (PE). However, cPLA$_2$α has the highest specificity towards phosphatidylcholine (PC) containing *sn-2* positioned AA (Dessen, Tang et al. 1999, Evans and Leslie 2004). Crystallization of cPLA$_2$α revealed an N-terminal C2 domain and a C-terminal catalytic domain (**Figure 1.3**) (Dessen, Tang et al. 1999). The C2 domain of cPLA$_2$α contains three Ca^{2+} binding loops. Ca^{2+} binding to the C2 domain of cPLA$_2$α increases its hydrophobicity and induces a conformational change in the protein, which allows cPLA$_2$α to translocate and interact with membrane lipids (Nalefski, McDonagh et al. 1998, Evans, Spencer et al. 2001, Evans and Leslie 2004). Various biochemical assays have demonstrated that the C2 domain of cPLA$_2$α is required for its translocation to intracellular membranes such as the Golgi apparatus, endoplasmic reticulum (ER), and the nuclear envelope (NE) (Nalefski, Slazas et al. 1997, Evans and Leslie 2004). However, translocation to the internal membranes is insufficient to activate the catalytic activity of cPLA$_2$α (Tucker, Ghosh et al. 2009). The combination of protein-protein interactions and phosphorylations is required for proper cPLA$_2$α activation.

The conformational change induced by the interaction of Ca^{2+} with the C2 domain of cPLA$_2$α exposes the tyrosine 464 (W464) residue on the catalytic domain. This residue helps orient and stabilize the interaction of cPLA$_2$α with the membrane, allowing the active site to interact with phospholipids (Nalefski, McDonagh et al. 1998, Tucker, Ghosh et al. 2009). Various phosphorylation sites and basic residues are also important for cPLA$_2$α activity (Tucker, Ghosh et al. 2009). It is currently thought that at steady state, cPLA$_2$α is bound to P11(S100A10)-Annexin

at position serine 727 (S727), inhibiting its activity (Wu, Angus et al. 1997, Hefner, Borsch-Haubold et al. 2000, Tian, Wijewickrama et al. 2008). Upon stimulation, the activation of the PKC pathway potentially dissociates the inhibitory complex at S727 by phosphorylating that site (Clark, Lin et al. 1991, Nemenoff, Winitz et al. 1993, Tian, Wijewickrama et al. 2008). The parallel activation of the MAPK pathway, leading to either ERK1/2 or P38 activation, phosphorylates serine 505 (S505), which is essential for cPLA$_2$α activity (**Figure 1.4**) (Lin, Wartmann et al. 1993, Nemenoff, Winitz et al. 1993, Gijon, Spencer et al. 2000, Tian, Wijewickrama et al. 2008).

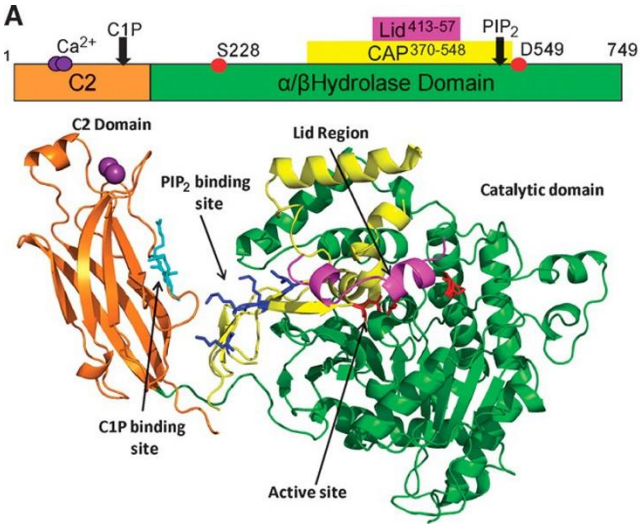

Figure 1.3: Crystal structure of cPLA$_2$α.

The crystal structure of cPLA$_2$α was adapted from (Burke and Dennis 2009) demonstrating the two domain structure: C2 and α/β hydrolase domain, and highlighting the critical residues on cPLA$_2$α

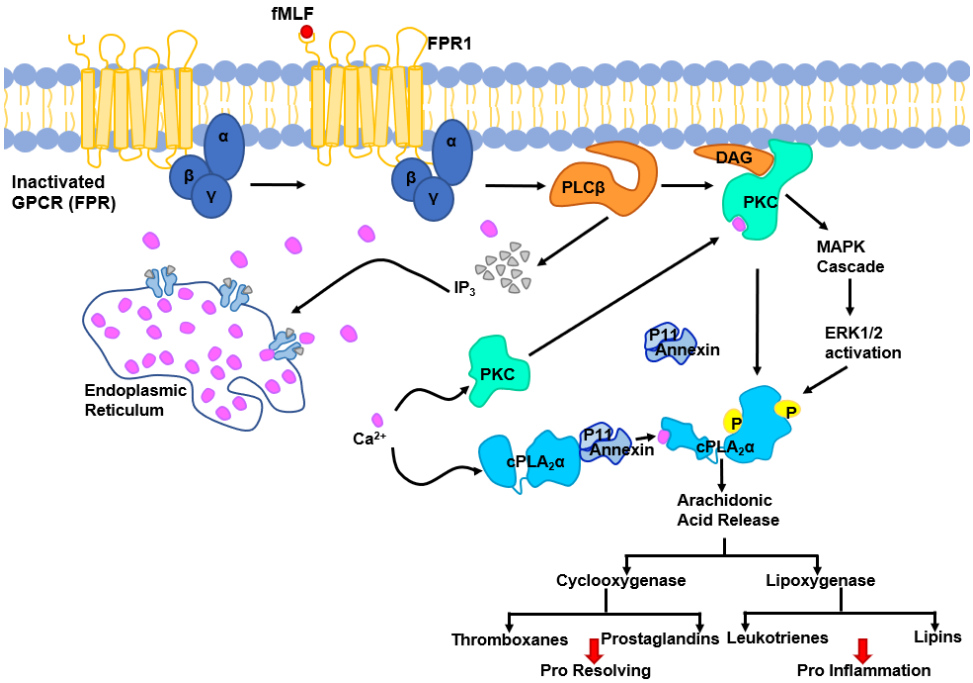

Figure 1.4: Schematic of cPLA$_2$α activation cascade (see text for details)

1.5 Functions of cPLA$_2$α

The primary function of cPLA$_2$α is to release AA from phospholipids. However, cPLA$_2$α has been implicated in other functions, including protein trafficking and lipid droplet generation. cPLA$_2$α plays an important role in phagocytosis and degranulation of innate immune cells. Some of these functions are discussed in detail below.

1.5.1 cPLA$_2$α in arachidonic acid production

In macrophages, cPLA$_2$α has been shown to translocate to the nuclear fraction to release AA (Peters-Golden and McNish 1993). Once released, AA is metabolized via one of four metabolic pathways: cyclooxygenase, lipoxygenase, cytochrome p450, or anandamide pathway to generate bioactive oxygenated polyunsaturated fatty acids (PUFA) (**Figure 1.5**) (Hanna and Hafez

2018). These PUFAs, also called eicosanoids, behave as signaling molecules or local hormones contributing to various biological activities in a paracrine or autocrine manner.

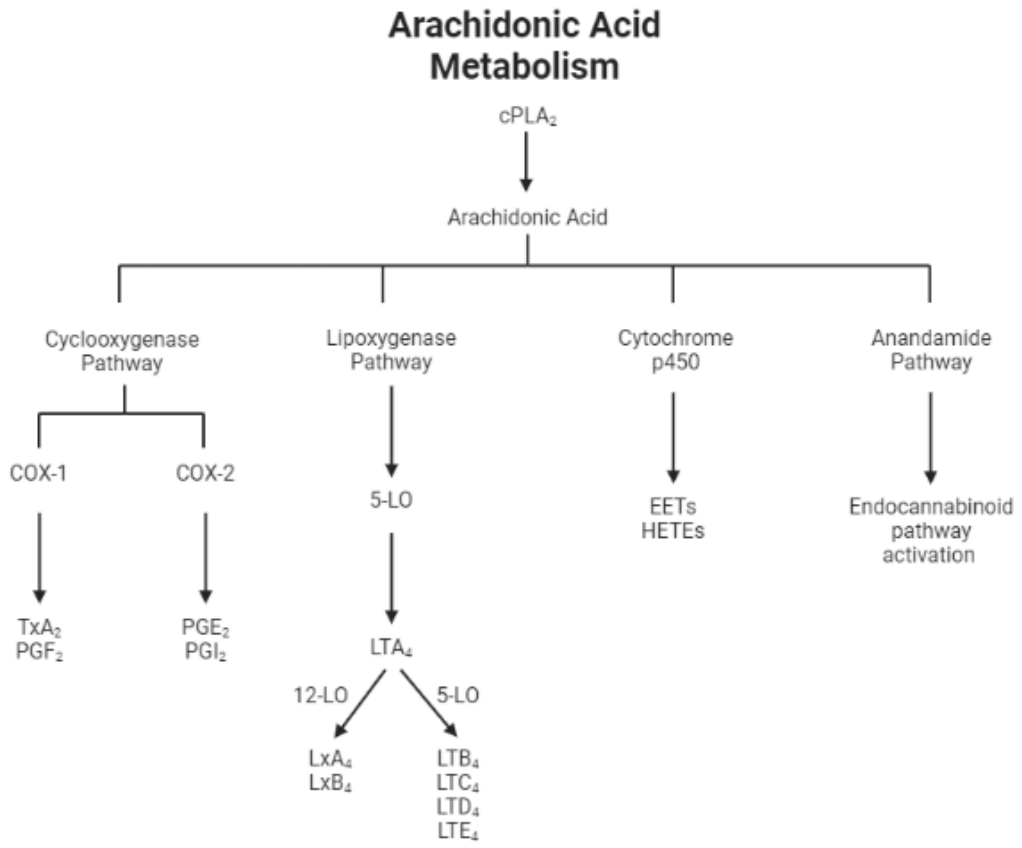

Figure 1.5: AA metabolism pathway.

A simple illustration of the AA metabolism pathway. COX-cyclooxygenase, PG-prostaglandin, Tx- thromboxane, LO-lipoxygenase, LT- leukotriene, Lx- lipoxin, EET- epoxyeicosatrienoic acid, HETE- hydroxyeicosatetraenoic acid.

1.5.1.1 Cyclooxygenase pathway

The cyclooxygenase pathway has two main enzymes: cyclooxygenase 1 (COX-1) and cyclooxygenase 2 (COX-2). Together these enzymes are responsible for generating prostaglandins and thromboxanes in a context-dependent manner. COX-1 is ubiquitously expressed and is primarily responsible for maintaining tissue homeostasis (Tomić, Micov et al. 2017). An example

of this homeostasis is seen in the gastrointestinal (GI) tract, where COX-1 is responsible for producing prostaglandins that help protect against injury and ulceration caused by various damaging agents, including natural acid production (Cryer 2001). In platelets, COX-1 is responsible for generating Thromboxane A_2 (TxA_2), which triggers platelet aggregation (Tomić, Micov et al. 2017). On the other hand, COX-2 expression is induced under inflammatory conditions and is primarily responsible for producing prostacyclin (PGI_2) and prostaglandin E_2 (PGE_2). These biomolecules cause vasodilation and trigger the fever initiation cascade, allowing the host to mount an inflammatory response and protect from infection (Cryer 2001, Dennis and Norris 2015, Tomić, Micov et al. 2017). Nonsteroidal anti-inflammatory drugs (NSAIDs), such as aspirin, ibuprofen, and naproxen, primarily act on the cyclooxygenase pathway to help reduce inflammation and fever (Tomić, Micov et al. 2017). Interestingly, in certain context, COX-2 derived prostaglandins can also have homeostatic or anti-inflammatory effects.

1.5.1.2 Lipoxygenase pathway

The other arm of the AA metabolism is the lipoxygenase pathway, which produces leukotrienes (pro-inflammatory molecules) and lipoxins (anti-inflammatory molecules). The major enzyme of this pathway is 5-lipoxygenase (5-LO), which along with the 5-LO activating protein (FLAP), converts AA to leukotriene A_4 (LTA_4). LTA_4 is a short-lived intermediary lipid that is converted to leukotriene B_4 (LTB_4) by the action of LTA_4 Hydrolase (LTA_4H) or to leukotriene C_4 (LTC_4) by the action of LTC_4 synthase (LTC_4S) (Haeggström and Wetterholm 2010). LTC_4 can be further metabolized to LTD_4 and LTE_4. When secreted by neutrophils, LTB_4 has been shown to dramatically amplify the signal from local injury or infection and recruit distant neutrophils (Lammermann, Afonso et al. 2013). This infiltration of neutrophils increases inflammation to help resolve the injury or infection (Samuelsson 1983, Lammermann, Afonso et

al. 2013). On the other hand, LTC_4 and its metabolites have been shown to act as bronchoconstrictors (Samuelsson 1983, Haeggström and Wetterholm 2010). LTA_4 can also be metabolized by another enzyme, 12-lipoxygenase (12-LO), to generate the lipoxin LxA_4 and LxB_4 (Serhan, Chiang et al. 2008, Bäck, Dahlén et al. 2011). These biomolecules have both, pro- and anti-inflammatory properties by reducing the infiltration of neutrophils to inflamed tissues and activating macrophages to engulf apoptotic cells at the site of inflammation (Schwab, Chiang et al. 2007, Serhan, Chiang et al. 2008, Bäck, Dahlén et al. 2011).

1.5.1.3 Cytochrome p450 pathway

A key characteristic of cytochrome p450 enzymes is the presence of heme iron. Originally thought to only reside in the liver to metabolize drugs and toxins, CYP enzymes have since been shown to be involved in various cellular functions, such as the generation and metabolism of cholesterol, bile acids, and Vitamin D3. AA metabolites from this pathway, such as 20-hydroxyeicosatrienoic acid (20-HETE) and epoxyeicosatrienoic acids (EETs), have been shown to cause vasodilation, vasoconstriction and have anti-inflammatory effects (Fleming 2001, Nebert and Dalton 2006, Dennis and Norris 2015, Fan, Muroya et al. 2015, Hanna and Hafez 2018).

1.5.1.4 Anandamide pathway

Increased levels of unesterified AA leads to apoptosis (Tallima and El Ridi 2018). In the event of excess free AA in the cell, AA is sequestered by the anandamide pathway. In the presence of ethanolamine, free AA is converted into anandamide by the action of the fatty acid amide hydrolase (FAAH) (Izzo and Deutsch 2011). Anandamide belongs to the family of endocannabinoids and is one of the two best-characterized endocannabinoids (Piomelli 2013).

1.5.2 cPLA$_2$α in membrane curvature

Cellular membranes are essential structures as they compartmentalize individual intracellular organelles. These membranes are composed of phospholipids. These highly dynamic membranes function as a barrier and can rapidly and precisely change their shape in response to various stimuli (Has, Sivadas et al. 2022). Membrane curvature can be induced through (1) protein-membrane interactions, (2) lipid shape changes, and (3) molecular crowding (Has, Sivadas et al. 2022, Peeters, Piët et al. 2022). cPLA$_2$α can induce membrane curvature through its lipase activity and protein-protein interactions. The cPLA$_2$α-mediated hydrolysis of neutral phospholipids, for example, phosphatidylcholine (PC), results in the release of AA and the generation of lysophosphatidylcholine (inverted-cone shaped lipid). The increase in the local concentration of inverted-cone shaped lysophospholipid on the membrane creates positive membrane curvature (**Figure 1.6**) (Brown, Chambers et al. 2003, Ha, Clarke et al. 2012). In addition, upon binding with Ca^{2+}, the C2 domain of cPLA$_2$α penetrates neutral phospholipids to a depth of 1-1.5nm, assisting in the induction of membrane curvature (Frazier, Wisner et al. 2002). Ward and colleagues further validated this by using various mutants of cPLA$_2$α lacking the ability to penetrate or bend membranes (Ward, Ropa et al. 2012). Additionally, it was shown that the C2 domain of cPLA$_2$α alone is sufficient for inducing membrane curvature in a cell free system (Ward, Sengupta et al. 2020). Interestingly, it was shown that the C2 domain of cPLA$_2$α preferentially translocates to smaller vesicles (~50nm) with high positive curvature versus larger vesicles (~600nm) (Ward, Sengupta et al. 2020). Together, these findings suggest that cPLA$_2$α can induce membrane curvature and that the C2 domain of cPLA$_2$α can sense the curvature on membranes and preferentially bind these curved regions (Ward, Sengupta et al. 2020).

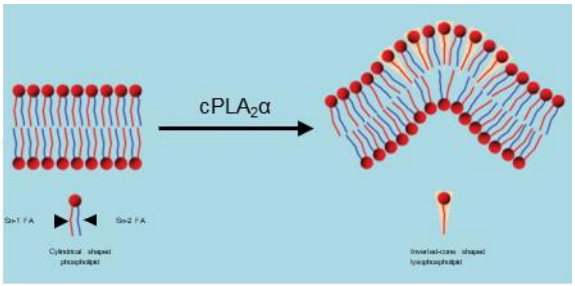

Figure 1.6: Illustration of the membrane curvature induced by cPLA$_2$α activity.

Differential catalysis of membrane phospholipids leads to an increase in the local concentration of lysophospholipids, leading to the induction of positive membrane curvature (*illustration adapted from (Brown, Chambers et al. 2003)*).

1.5.3 cPLA$_2$α in degranulation and phagocytosis

The PLA$_2$ family of enzymes have been implicated in various steps of phagocytosis and degranulation since the 1980s and 1990s (Scott, Zrike et al. 1980, Dana, Leto et al. 1998). cPLA$_2$α has been shown to be involved in degranulation by platelets as platelets derived from cPLA$_2$αKO mice showed a significant delay in degranulation (Wong , Kita et al. 2002). cPLA$_2$α is not involved in the phagocytosis of opsonized zymosan particles in neutrophil-like cells (Levy 2006). However, recent studies have implicated cPLA$_2$α in regulating zymosan containing phagosomes and Fc receptor–mediated phagocytosis in Raw264.7 macrophages (Casas, Valdearcos et al. 2010, Zizza, Iurisci et al. 2012), indicating that the involvement of cPLA$_2$α in phagocytosis depends on the cell type and function. The mechanism by which cPLA$_2$α mediates phagocytosis remains unknown.

1.6 cPLA$_2$α in disease

Although cPLA$_2$αKO mice develop normally and live normal life spans, there are some significant differences between WT and cPLA$_2$αKO mice. For instance, female KO mice have defects in fertility - producing smaller litters and eventually losing their ability to conceive

(Bonventre, Huang et al. 1997). Interestingly, it has been determined that cPLA$_2$αKO mice are resistant to acute lung injury (Nagase, Uozumi et al. 2000) and auto-immune diabetes (Oikawa, Yamato et al. 2005). This is potentially due to the fact that neutrophils and macrophages derived from cPLA$_2$αKO mice do not produce prostaglandins or leukotrienes, the key mediators for inflammation (Bonventre, Huang et al. 1997). Additionally, these mice showed a decrease in lung cancer and tumor angiogenesis (Meyer, Dwyer-Nield et al. 2004, Linkous and Yazlovitskaya 2010, Linkous, Yazlovitskaya et al. 2010).

Contrasting mice studies, mutations in cPLA$_2$α leads to deleterious effects in humans. Patients with different mutations in cPLA$_2$α commonly show abnormalities in the GI tract. However, there are differences in clinical presentation and the severity of disease (Leslie 2015). Patients with heterozygous single base pair mutations, S111P, R485H, or D575H, in cPLA$_2$α had GI bleeds and anemia in their childhood with increased acute GI bleeding and ulceration in ileum and jejunum as an adult (Leslie 2015). The most severe case of cPLA$_2$α mutation was presented in two siblings who inherited a homozygous four base pair deletion in the cPLA$_2$α gene, resulting in a premature stop codon with the loss of 43 amino acids at the C-terminus of cPLA$_2$α. At the age of 4 years, the male patient presented with severe peptic ulceration and bleeding. He also developed type 2 diabetes, peripheral neuropathy, and osteoporosis over the next several years. On the other hand, his sister presented with severe GI abnormalities as early as the age of 2 years, which worsened over time. She developed acute respiratory distress syndrome, acute renal failure, endometriosis, infertility, left ventricular concentric hypertrophy, and fibrotic bladder with sones (Leslie 2015). These studies show a critical role for cPLA$_2$α in maintaining gut integrity in humans. Additionally, these studies highlight the differences in the role of cPLA$_2$α and eicosanoid signaling in mice and humans.

In human neutrophils, cPLA$_2$α plays a crucial role in mediating pro- or anti-inflammatory responses by regulating the generation of specific mediators (Hurley, Pirzai et al. 2011). Therefore, disruptions in the activity of cPLA$_2$α can lead to disruptions in the host defense. Yonker et al. showed that inhibition of cPLA$_2$α in human neutrophils leads to a decrease in their ability to detect infection, leaving the host vulnerable to infection (Yonker, Pazos et al. 2017). On the other hand, patients suffering from sepsis show higher cPLA$_2$α expression and activity, sending the host's immune system into hyperdrive and potentially leading to death (Levy, Dana et al. 2000). Therefore, there needs to be a fine balance between the expression and activity of cPLA$_2$α to maintain homeostasis. These results suggest that cPLA$_2$α could be used as a potential therapeutic target against some diseases. However, further research is required to fully appreciate the various functions of cPLA$_2$α.

1.7 Summary and research goals

cPLA$_2$α has been extensively studied since the late 1980s, when it was first characterized in neutrophils and platelets (Alonso, Henson et al. 1986, Kramer, Checani et al. 1986). To date, cPLA$_2$α has been implicated in various cellular processes including, but not limited to, the production of eicosanoids and maintaining lipid homeostasis. In neutrophils, macrophages, and platelets, cPLA$_2$α has been implicated in phagocytosis and degranulation. However, the exact mechanism by which cPLA$_2$α performs these functions is still largely unclear, particularly in the context of the recently discovered role of cPLA$_2$α in inducing membrane curvature (Ward, Ropa et al. 2012, Ward, Bhardwaj et al. 2013, Ward, Sengupta et al. 2020).

In the context of neutrophils, the first line of defense against infection or injury, cPLA$_2$α has only been implicated in the generation of LTB$_4$ (Shah, Burg et al. 2017, Yonker, Pazos et al. 2017). Interestingly, most studies that imply other role for cPLA$_2$α in neutrophils often leave it as

"data not shown." Therefore, for my thesis work, I set out to study the function of cPLA$_2$α in neutrophils. cPLA$_2$α is a fascinating enzyme. Even after 30+ years of research, the localization of cPLA$_2$α is often questioned. Various reports show it in the cytosol, translocating to internal organelles such as the Golgi, ER and nucleus upon stimulation from a calcium ionophore, A23187 (Gijón and Leslie 1999, Gijón, Spencer et al. 1999, Gijon, Spencer et al. 2000, Evans, Spencer et al. 2001, Evans and Leslie 2004, Leslie, Gangelhoff et al. 2010). However, other reports show cPLA$_2$α in the nucleoplasm, translocating to the inner NE (Enyedi, Jelcic et al. 2016, Lomakin, Cattin et al. 2020, Venturini, Pezzano et al. 2020). Based on the multiple roles played by cPLA$_2$α, I hypothesized that cPLA$_2$α is not only involved in LTB$_4$ generation but also regulates membrane curvature and cell migration in human neutrophils. I first collaborated with Dr. Subhash Arya, a post-doctoral fellow in our lab, to identify the origin of LTB$_4$ secreting exosomes at the nuclear envelope (Chapter 2). Additionally, in chapter 3, I investigated the role of cPLA$_2$α in neutrophil migration. Finally, in chapter 4, I show that cPLA$_2$α is not only involved in the generation of LTB$_4$ but also is required to maintain lipid homeostasis in the chemotaxing neutrophil-like cells.

Chapter 2 Ceramide-Rich Microdomains Facilitate Nuclear Envelope Budding for Non-Conventional Exosome Formation

Subhash B Ayra, Song Chem, **Fatima Jordan-Javed**, and Carole A. Parent

The work presented in this chapter has been previously published (PMID: 35739317). I contributed experimentally to protocol standardization, quantification, and exosome isolation and characterization. Specifically, I contributed to the following figures: Figure 4.3 (Figures 4.3D and 4.3E) and Extended Figures 4.3 and 4.7. Additionally, I contributed to editing and proofing the manuscript for publication.

2.1 Abstract

Neutrophils migrating towards chemoattractant gradients amplify their recruitment range by releasing the secondary chemoattractant leukotriene B_4 (LTB_4). We previously demonstrated that LTB_4 and its synthesizing enzymes, the 5-lipoxygenase (5-LO), 5-LO activating protein (FLAP), and leukotriene A_4 hydrolase (LTA_4H), are packaged and released in exosomes. We now report that the biogenesis of the LTB_4-containing exosomes originates at the nuclear envelope (NE) of activated neutrophils. We show that the neutral sphingomyelinase 1 (nSMase1)-mediated generation of ceramide enriched lipid-ordered microdomains initiates the clustering of the LTB_4-synthesizing enzymes on the NE. We isolated and analyzed exosomes from activated neutrophils and established that the FLAP/5-LO-positive exosome population is distinct from that of the CD63-positive exosome population. Furthermore, we observed a strong co-localization between ALIX and FLAP at the periphery of nuclei and within cytosolic vesicles. We propose that the initiation of NE curvature and bud formation is mediated by nSMase1-dependent ceramide generation, which leads to FLAP and ALIX recruitment. Together, these observations elucidate the mechanism for LTB_4 secretion and identify a non-conventional pathway for exosome generation.

.

2.2 Introduction

Neutrophils represent the first line of defense at sites of injury or infection (Burn, Foti et al. 2021). Upon exposure to primary chemoattractants, e.g., formyl peptide N-Formyl-methionine-leucyl-phenylalanine (fMLF), neutrophils rapidly secrete the secondary chemoattractant leukotriene B_4 (LTB_4) which serves to maintain the robustness and sensitivity to primary chemoattractant signals and dramatically increase the range and persistence of migration (Afonso, Janka-Junttila et al. 2012). LTB_4-synthesis is initiated with the release of arachidonic acid (AA) through phospholipid hydrolysis mediated by the translocation of cytosolic-phospholipase A_2 ($cPLA_2$) to the nuclear envelope (NE) (Schievella, Regier et al. 1995). The NE-associated transmembrane protein, 5-lipoxygenase activating protein (FLAP), presents the released AA to 5-lipoxygenase (5-LO), which generates leukotriene A_4 (LTA_4). LTA_4 is in turn quickly hydrolyzed to LTB_4 by LTA_4 hydrolase (LTA_4H) (Sadik and Luster 2012). It has been shown that the LTB_4-synthesizing enzymes are present in exosomes secreted from macrophages, dendritic cells, and chemoattractant-activated neutrophils (Esser, Gehrmann et al. 2010, Majumdar, Tavakoli Tameh et al. 2021). Exosomes are synthesized as intraluminal vesicles (ILVs) within multivesicular bodies (MVBs) and secreted upon fusion of MVBs with the plasma membrane. The sorting of cargos packaged in ILVs is mediated by the tetraspanin CD63, the endosomal sorting complex required for transport (ESCRT) complexes, or affinity towards neutral sphingomyelinase (nSMase)-dependent ceramide-rich lipid microdomains (van Niel, D'Angelo et al. 2018). The inhibition of LTB_4 synthesis *ex vivo* (Lammermann, Afonso et al. 2013) or *in vivo* (Terradas, Martín et al. 2009, Oyoshi, He et al. 2012, Lammermann, Afonso et al. 2013) or the inhibition of exosome release through neutral sphingomyelinase1 (nSMase1) knockdown (Majumdar, Tavakoli Tameh et al. 2021) results in diminished neutrophil recruitment in response to sterile injury or

bacterial peptides with a concomitant decrease in recruitment range. In this context, we envision that the packaging of LTB_4 in exosomes provides a mechanism to support intercellular signaling in harsh extracellular environments.

2.3 Results and Discussion

2.3.1 LTB_4 synthesizing machinery is packaged in NE-Derived buds and cytosolic vesicles

To gain more insight into the mechanisms that regulate the biogenesis of LTB_4-containing exosomes, we measured FLAP and 5-LO distribution in activated human peripheral blood-derived primary polymorphonuclear neutrophils (PMNs) uniformly stimulated with fMLF. In resting cells, while FLAP clearly showed NE and reticulate (endoplasmic reticulum) localization, 5-LO mainly localized inside the nucleus. However, 15 min after fMLF addition, we readily observed the appearance of FLAP-positive NE buds that also contained 5-LO (**Figure 2.6A**). The NE origin of these buds was confirmed using the inner-nuclear membrane (INM) resident protein, Lamin B Receptor (LBR), which we observed around 5-LO-positive perinuclear as well as cytosolic vesicles (**Figure 2.1**: The LTB4-syntheszing machinery is packaged in NE derived buds and cytosolic vesicles in activated neutrophils.**A**). The temporal increase in the percentage of PMNs with LBR-positive NE buds and cytosolic vesicles upon fMLF stimulation highlights the requirement for chemotactic activation in the generation of NE-derived buds and cytosolic vesicles (**Figure 2.1B**). Similar findings were observed in PMNs chemotaxing towards fMLF (**Figure 2.1C, D**), where we observed that the LBR-positive vesicles present in the cytosol are consistently smaller in size, compared to the NE-associated buds in these cells (**Figure 2.1C, D and Figure 2.6B**). We also observed the presence of LTA_4H within the LBR-positive NE-buds and cytosolic vesicles (**Figure 2.1E, F**), substantiating the nuclear origin of the LTB_4-containing exosomes. NE budding and vesiculation have been reported during the formation of micronuclei in cancer cells

and are characterized by the presence of the nucleoskeleton proteins, LaminB1 and or Lamin A/C, along with the DNA repair machinery in LBR-positive vesicles (Terradas, Martín et al. 2009, Terradas, Martín et al. 2012). To rule out the possibility that the LBR-positive NE buds and cytosolic vesicles we observed are micronuclei, we immunostained chemotaxing PMNs with Lamin B1 as PMNs express very low levels of Lamin A/C and are devoid of measurable DNA repair (Manley, Keightley et al. 2018). We found that the LBR positive buds and cytosolic vesicles are devoid of Lamin B1 signal (**Figure 2.6C**).

2.3.2 nSmase1 facilitates the recruitment of LTB4 synthesizing machinery on the lipid ordered microdomains

Changes in lipid bilayer symmetry are required to induce membrane curvatures for the initiation of budding. Whereas certain transmembrane or BAR-domain-containing proteins are involved in facilitating membrane curvature, the localized presence of lipids, such as ceramide and lysophosphatidic acid, has also been reported to induce changes in membrane curvature (McMahon and Boucrot 2015). Furthermore, lipid-ordered domains that contain ceramide and the ganglioside GM1 are required for the assembly of various signaling complexes and their endocytosis (Eich, Manzo et al. 2016, Kabbani, Raghunathan et al. 2020). To assess whether membrane microdomains are involved in NE budding we performed confocal fluorescence microscopy of chemotaxing PMNs in the presence of the phase transition sensitive lipid probe di-4ANEPPDHQ (Owen, Rentero et al. 2011). We took advantage of the blue shift in fluorescence of di-4ANEPPDHQ upon binding with lipids in ordered membrane environments, to acquire general polarization (GP) images of chemotaxing PMNs, where high GP values indicate lipid ordered (L_o) domains. Time-lapse imaging showed spatiotemporal increases in regions of high GP values in punctae close to the nucleus in PMNs chemotaxing towards fMLF and quantification

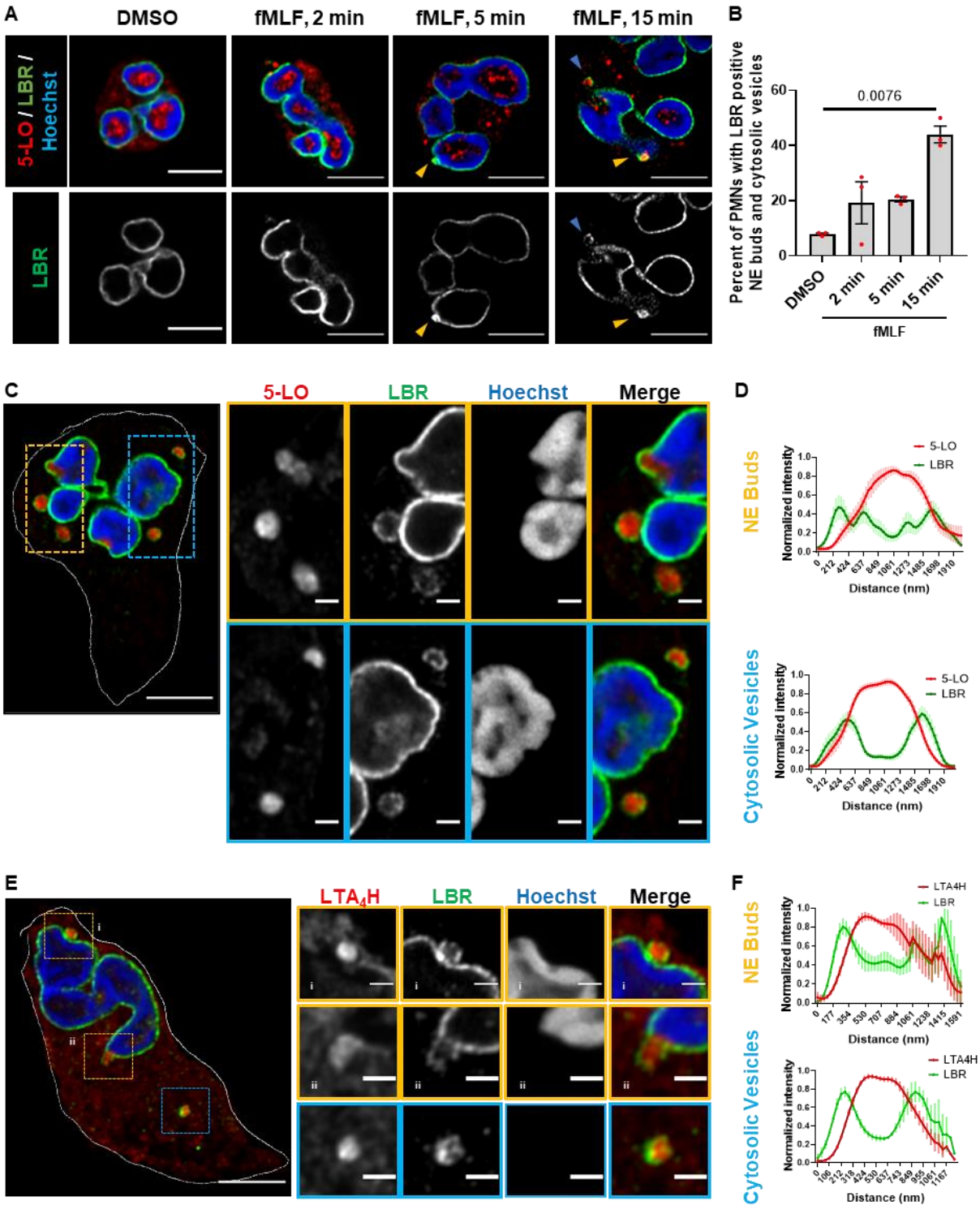
A
DMSO
fMLF, 2 min
fMLF, 5 min
fMLF, 15 min
5-LO / LBR / Hoechst
LBR
B
Percent of PMNs with LBR positive NE buds and cytosolic vesicles
0.0076
DMSO
2 min
5 min
15 min
fMLF
C
5-LO
LBR
Hoechst
Merge
D
NE Buds
Cytosolic Vesicles
Normalized intensity
Distance (nm)
E
LTA4H
LBR
Hoechst
Merge
F
NE Buds
Cytosolic Vesicles
Normalized intensity
Distance (nm)

Figure 2.1: The LTB_4-syntheszing machinery is packaged in NE derived buds and cytosolic vesicles in activated neutrophils.

A Representative Airyscan microscopy images showing the distribution of LBR (green) and 5-LO (red) in fixed PMNs uniformly stimulated with 20 nM fMLF (n=3). The yellow arrowheads point to nuclear buds and the blue arrowheads point to cytosolic vesicles. Scale bar is 5 µm. **B** Scatter dot plot showing the percentage of PMNs containing LBR-positive buds and cytosolic vesicles in a field of randomly selected images. Data collected from 50, 46, 74, and 66 cells in DMSO, 2min, 5 min, and 15 min fMLF treatment, respectively, pooled from three independent experiments are plotted as mean ± SEM. Each dot represents the value from one experiment. P=0.0076 as obtained from RM one-way ANOVA analysis. **C** Representative Airyscan microscopy images of PMNs chemotaxing towards 100 nM fMLF and stained for LBR (green) and 5-LO (red), obtained from six independent experiments. NE buds are shown in yellow boxes and cytosolic vesicles are shown in blue boxes. Scale bar is 5 µm. In magnified insets, the scale bar is 1 µm. **D** Histograms showing the normalized intensity of LBR and 5-LO across the diameter of LBR positive buds and cytosolic vesicles. Data points from 15 vesicles and 13 buds within 11 cells pooled from four independent experiments are plotted as mean +/- SEM, with the bold line showing the mean and bar representing the SEM. **E** Representative Airyscan microscopy images of fixed PMNs chemotaxing towards 100 nM fMLF and stained for LBR (green) and LTA_4H (red), obtained from three independent experiments. See panel C for more details. Scale bar is 5 µm. In the inset, it is 1 µm. **F** Histograms showing the normalized intensity of LBR and LTA_4H across the diameter of LBR positive buds and cytosolic vesicles. Data points from 5 vesicles and buds each within 5 different cells pooled from three independent experiments were plotted as mean +/- SEM, with the bold line showing the mean and bar representing the SEM. Source numerical data are available in the source data file

revealed the abundance of L_o punctae within 1μm of the nucleus compared to the rest of the cell (**Figure 2.2A, B**).

Sphingomyelin, the major phosphosphingolipid in mammalian cells, is hydrolyzed to ceramide and phosphocholine by the action of sphingomyelinases (Lucki and Sewer 2012). The enrichment of ceramide coalesces nanoscale lipid domains leading to the formation of microscopic ceramide-rich signaling platforms (Airola and Hannun 2013). The nSMase1 and its substrate sphingomyelin are abundant in the nucleus (Mizutani, Tamiya-Koizumi et al. 2001) and the depletion of nSMase1 from cancer cells (Luberto, Hassler et al. 2002), neuronal cells (Guo, Bellingham et al. 2015), or neutrophils (Majumdar, Tavakoli Tameh et al. 2021) has been reported to decrease the secretion of CD63-positive exosomes as well as FLAP/5-LO-positive exosomes from neutrophils. We, therefore, assessed the role of nSMases on the generation of the nuclear lipid microdomains in chemotaxing PMNs using the nSMase inhibitor GW4869 (Luberto, Hassler et al. 2002) and found a strong dependence between nSMase activity and the generation of perinuclear L_o domains (**Figure 2.2C, D**). In addition, we found similar defects in differentiated HL-60 (dHL-60) cells genetically lacking nSMase1 (**Figure 2.7A-D).**

Lipid-ordered domains are resistant to solubilization in non-ionic detergents, by virtue of their ceramide-, GM1- and cholesterol-rich composition (Magee and Parmryd 2003). To assess the role of nSMase1-dependent lipid ordering in the recruitment of FLAP and 5-LO at sites of NE budding, we isolated nuclei from resting and fMLF-stimulated Scramble (Scr) and nSMase-1 KO dHL-60 cells and separated detergent-resistant membranes (DRMs) and detergent soluble membranes (DSMs) (**Figure 2.8A**). The purity of the nuclear preparation from resting dHL-60 cells was assessed using GAPDH (cytosol marker), calreticulin (ER marker), LBR (NE

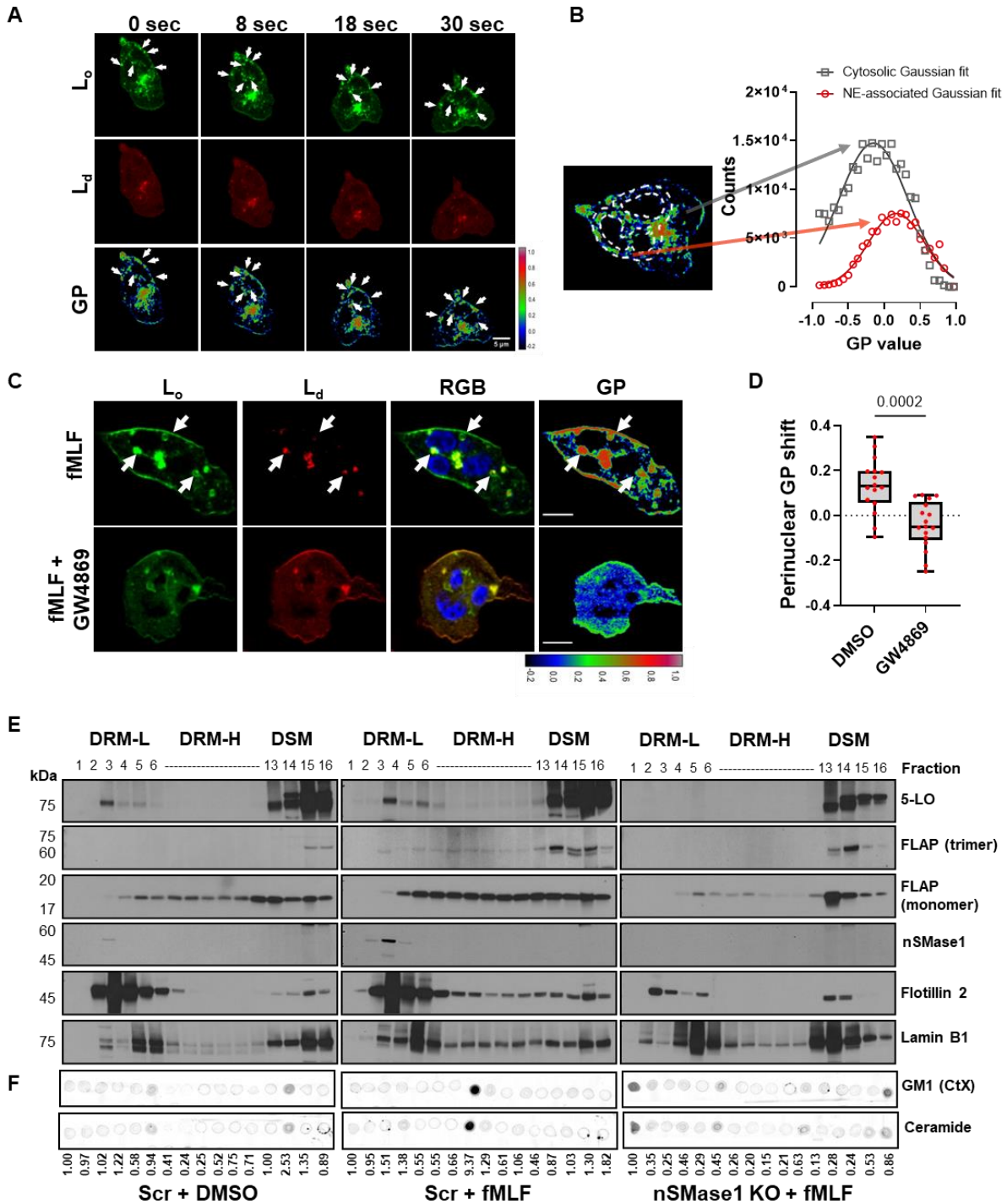
A
0 sec
8 sec
18 sec
30 sec
Lo
Ld
GP
B
Cytosolic Gaussian fit
NE-associated Gaussian fit
Counts
GP value
C
Lo
Ld
RGB
GP
fMLF
fMLF + GW4869
D
0.0002
Perinuclear GP shift
DMSO
GW4869
E
DRM-L
DRM-H
DSM
Fraction
kDa
5-LO
FLAP (trimer)
FLAP (monomer)
nSMase1
Flotillin 2
Lamin B1
F
GM1 (CtX)
Ceramide
Scr + DMSO
Scr + fMLF
nSMase1 KO + fMLF
G
Arbitrary intensity
FLAP monomer
FLAP trimer
Flotillin 2
DMSO
fMLF
nSMase1 KO + fMLF

Figure 2.2: nSMase1 facilitates the recruitment of the LTB_4 synthesizing machinery on lipid-ordered NE microdomains

A Representative fluorescence images of di-4-ANEPPDHQ-stained PMNs chemotaxing towards 100 nM fMLF (n=5), showing the temporal distribution of the lipid-ordered (L_o) domains (green), lipid-disordered (L_d) domains (red), and the corresponding GP image. Pseudo-colored GP images are based on the colormap, with white/red shades depicting lipid ordered regions and blue/darker shades representing lipid disordered regions. White arrows mark the perinuclear vesicular regions of high GP values. Scale bar is 5µm. **B** Histogram depicting the gaussian distribution of the GP pixel intensity obtained from the two ROIs as depicted in the left image, with the cytosol ROI (gray arrow) 1 µm from the nuclear boundary and the perinuclear ROI (red arrow) extending up to 1 µm from the nucleus. **C** Representative fluorescence images of di-4-ANEPPDHQ-stained PMNs chemotaxing towards 100 nM fMLF in the presence of DMSO or 3 µm GW4869 (n=3). The lipid-ordered (L_o) domains (green), lipid-disordered (L_d) domains (red), RGB images as the merge of L_d, L_o, and Hoechst (blue), and GP images are presented. For color scale, refer to panel A. White arrows show the perinuclear vesicular regions of high GP values. Scale bar is 5 µm. Also, see Supplementary Movie S1. **D** Graph showing the median value of the perinuclear GP intensity distribution of DMSO- and GW4869-treated PMNs chemotaxing towards fMLF, presented as a box-whisker plot where whiskers indicate the range, and the boundary of the box closest to the x-axis indicates 25^{th} percentile, while farthest one indicates 75^{th} percentile. The line within the box represents the median and the red dots indicate16 data points from the DMSO sample and 17 from the GW4869 sample (n=3). P value quantified using the two-tailed Mann-Whitney test. **E** Representative western blots showing the distribution of various proteins in DRM-L, DRM-H, and detergent soluble membranes (DSM) fractions isolated from the NE of Scr or nSMase1 KO dHL-60 cells stimulated with 100 nm fMLF (n=3). Lamin B1 is used as a loading control. **F** Representative dot-blots of lipids isolated from the fractions shown in panel E stained for GM1 or ceramide (n=2). The ceramide intensity values of the spots relative to lane 1 of each condition are indicated below the dot blot. **G** Bar graphs depicting the arbitrary intensity of FLAP monomer, FLAP trimer, and Flotillin 2 signal in the different fractions of either DMSO- or fMLF-treated Scr cells or fMLF-treated nSMase1 KO cells. Data are plotted as mean ± SEM, and P values are determined using two-way ANOVA, with DMSO as a control column (n=3). Source numerical data and unprocessed blots are available in the source data file.

marker), Histone H3 (chromatin marker), and LTB_4 synthesizing machinery, FLAP, and 5-LO (**Figure 2.8B**). Flotillin 2 and Lamin B1 were used as a lipid microdomain marker and as a loading control, respectively (**Figure 2.2E**). We found an increase in the intensity of FLAP monomers and trimers – the functional form of FLAP (Mandal, Jones et al. 2008)- along with 5-LO in both light detergent resistant membrane fractions (DRM-L) enriched with Flotillin 2 as well as in heavy DRM fractions (DRM-H) enriched with ceramide/GM1, upon fMLF stimulation in Scr dHL-60 cells (**Figure 2.2E, F**). nSMases have been reported to bind sphingomyelin-rich nanodomains for ceramide generation and to dissociate from ceramide-rich microdomains/DRM-H (Kolesnick 2002), accordingly, we found that nSMase1 was only enriched in DRM-L fractions (**Figure 2.2E**). Remarkably, we observed a dramatic inhibition of monomeric and trimeric FLAP signals in the DRM-L and DRM-H fractions in nuclei isolated from fMLF-activated nSMase1 KO dHL-60 cells compared with Scr dHL-60 cells, which also showed a loss of ceramide/GM1 in DRM-H fractions, while Flotillin 2 levels remained grossly unchanged (**Figure 2.2E-G**). Since low temperatures employed during the biochemical isolation of DRMs can artificially induce the formation of DRMs in some cases (Schuck, Honsho et al. 2003), we assessed FLAP aggregation on the NE of fixed nuclei isolated from either DMSO- or fMLF-treated Scr or nSMase1 KO dHL-60 cells. As depicted in Figure 3A, we observed an increase in the regions with high FLAP signal intensity in fMLF-stimulated Scr dHL-60 cells compared to DMSO-treated Scr and fMLF-treated nSMase1 KO dHL-60 cells, demonstrating a nSMase1-dependent increase in FLAP recruitment in response to fMLF activation. However, the absence of nSMase1 did not alter the decrease in the nuclear sphericity observed in response to fMLF stimulation (**Figure 2.3B**). We next labeled the nuclei isolated from PMNs with antibodies against ceramide and FLAP and assessed object colocalization from 3D-reconstructions of z-stacks imaged using Airyscan microscopy. We observed defects in the fMLF-

induced increase in the colocalization of FLAP with ceramide clusters in the nuclei isolated from GW4869-treated PMNs (**Figure 2.3C**). Upon quantification, we measured a significant decrease in FLAP-ceramide co-occurrence and correlation upon nSMase inhibition in fMLF activated PMNs (**Figure 2.3D**). Together, these findings establish the requirement of nSMase1 for the ceramide-dependent enrichment of FLAP on the NE of activated neutrophils and dHL-60 cells.

2.3.3 nSmase1 and ceramide are present within and are required for the generation of NE derived 5LO/LBR positive NE buds and cytosolic vesicles

We next sought to visualize the distribution of nSMase1 and ceramide in PMNs. We stained PMNs chemotaxing towards fMLF with ceramide and LBR and observed ceramide staining on the NE as well as on the inner periphery of LBR-positive NE buds and cytosolic vesicles (**Figure 2.4A, B**). We also found a strong colocalization between nSMase1 and ceramide and between nSMase1 and 5-LO on NE buds and cytosolic vesicles (**Figure 2.4C, D**). Consistent with the previously reported nuclear localization of nSMase1 (Mizutani, Tamiya-Koizumi et al. 2001), we observed nSMase1 localization on the NE (**Figure 2.4D, green arrows**). Similarly, in dHL-60 cells expressing nSMase1-GFP chemotaxing towards fMLF, we observed a clear NE distribution along with a strong enrichment at the sites of NE buds (**Figure 2.9**). Since ceramide-induced changes in membrane curvature are required for the initiation of vesicle budding (Trajkovic, Hsu et al. 2008), we investigated the effect of nSMase inhibition on NE-budding and vesiculation. We found a reduction in the percent of cells showing LBR- and 5-LO-positive NE buds and cytosolic vesicles in GW4869-treated PMNs chemotaxing toward fMLF (**Figure 2.4E, F**). However, most of the few remaining LBR-positive vesicles observed in the GW4869-treated cells were NE-associated (**Figure 2.4G**). These findings suggest that while other components can initiate the formation of NE buds, nSMase activity is required for the release of the NE buds and

the generation of cytosolic vesicles. Indeed, the membrane bending properties of $cPLA_2$ (Ward, Ropa et al. 2012), which is upstream of nSMase, could contribute to the formation of NE-associated buds.

2.3.4 5LO positive and CD63 negative punctae are present within the LBR positive vesicles

To further characterize the nature of the 5-LO/FLAP/LBR-positive NE buds and cytosolic vesicles, we used expansion microscopy – a method developed to enable confocal microscopy to visualize sub-diffraction limited details by isotropic enlargement of the samples (Gambarotto, Zwettler et al. 2019, Nijenhuis, Damstra et al. 2021). PMNs chemotaxing under agarose were fixed, stained, crosslinked, and expanded as described in the methods section, giving rise to an expansion of the sample by ~4x. We observed the clear presence of 5-LO-positive punctae within the LBR-positive cytosolic vesicles **(Figure 2.5A)** and NE-associated buds **(Figure 2.5B)** in chemotaxing cells. We also noted the presence of ceramide mainly at the periphery of the LBR-positive structures, although small ceramide punctae could also be seen inside the structures (**Figure 2.5A-B**), as observed using traditional IF imaging (**Figure 2.4A-B)**. The median diameter of the LBR-positive NE buds and cytosolic vesicles was 972.5 nm (**Figure 2.5C**), which closely matched the sizes measured using conventional confocal imaging (1000 ± 200 nm) (**Figure 2.6B**), and the median diameter of the 5-LO positive punctae present within the LBR NE buds or cytosolic vesicles was 200 nm (**Figure 2.5D**). We also observed a positive correlation between the size of the LBR-positive vesicles and the number of 5-LO-positive punctae within the LBR-positive vesicles (**Figure 2.5C**). Notably, we did not observe the presence of the canonical exosome marker CD63 within the LBR-positive structures, although CD63-positive structures did contain ceramide punctae, indicative of ceramide enriched conventional ILVs (Elsherbini and Bieberich 2018) (**Figure 2.5E, F, Figure 2.10A, B**). The CD63-positive MVBs had a smaller diameter that ranged

between 350-420 nm (**Figure 2.10C**) which matches the reported size range of CD63-positive MVBs (Verweij, Bebelman et al. 2018). Using traditional IF, we also found that the number and size of the CD-63-positive MVBs did not change in response to fMLF stimulation (**Figure 2.10D, E**). We previously observed the colocalization of mCherry-5-LO with CD63-GFP in chemotaxing dHL-60 cells (Majumdar, Tavakoli Tameh et al. 2021). We envision that this was a consequence of 5-LO overexpression and/or to the potential multimerization from the mCherry fusion, targeting mCherry-5-LO to the CD63 positive MVBs. Together, these findings suggest that LBR-positive MVBs contain 5-LO-positive ILVs and are distinct from the canonical CD63-positive MVBs in both their composition and their size.

As we previously reported using shRNA mediated nSMase1/SMPD2 knockdown HL-60 cells (Majumdar, Tavakoli Tameh et al. 2021), we found that fMLF-stimulated nSMase1 KO dHL-60 cells release fewer exosomes, compared to Scr dHL-60 cells. Using nanoparticle tracking analysis (NTA), we now found that Scr cells release two major populations of exosomes in response to fMLF stimulation (**Figure 2.11A, B**). Interestingly, exosomes isolated from nSMase1 KO dHL-60 cells showed a significant decrease in the number of the larger, >180 nm, particles, which correlated with the size of the 5-LO punctae within the LBR-positive MVBs measured using expansion microscopy (**Figure 2.5D**). We also observed a decrease in the levels of 5-LO and FLAP (**Figure 2.11C, D**) and of LTB_4 content (**Figure 2.11E**) in exosomes isolated from the nSMase1 KO cells. Although exosomal Flotillin 2 levels did not change significantly in the nSMase1 KO cells, CD63 levels decreased (**Figure 2.11C, D**), as we previously published(Majumdar, Tavakoli Tameh et al. 2021). A closer analysis of the fractions of the supernatants from fMLF-stimulated PMNs separated by density gradient

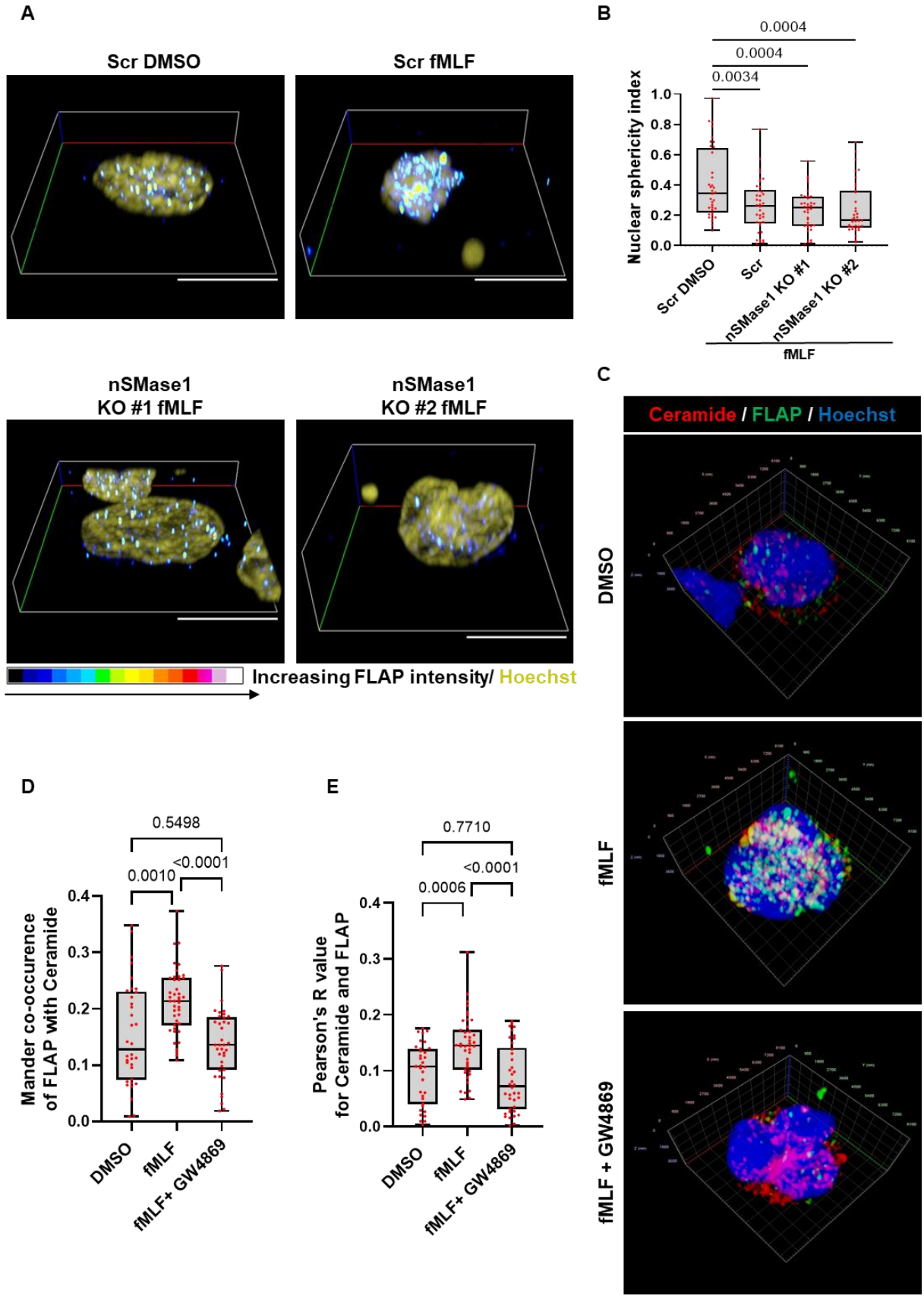
A
Scr DMSO
Scr fMLF
nSMase1
KO #1 fMLF
nSMase1
KO #2 fMLF
Increasing FLAP intensity/ Hoechst
B
0.0004
0.0004
0.0034
Nuclear sphericity index
1.0
0.8
0.6
0.4
0.2
0.0
Scr DMSO
Scr
nSMase1 KO #1
nSMase1 KO #2
fMLF
C
Ceramide / FLAP / Hoechst
DMSO
fMLF
fMLF + GW4869
D
0.5498
0.0010
<0.0001
Mander co-occurence of FLAP with Ceramide
0.4
0.3
0.2
0.1
0.0
DMSO
fMLF
fMLF+ GW4869
E
0.7710
0.0006
<0.0001
Pearson's R value for Ceramide and FLAP
0.4
0.3
0.2
0.1
0.0
DMSO
fMLF
fMLF+ GW4869

Figure 2.3 nSMase-dependent enrichment and colocalization of FLAP with ceramide-positive structures on the NE of activated neutrophils

A Representative 3D volumetric render of the fixed nuclei isolated from DMSO or fMLF (100 nM) stimulated Scr or nSMase1 KO dHL-60 cells stained for FLAP (spectrum) and Hoechst (olive). Red/whiter shades as shown in the colormap, denote higher FLAP intensity whereas blue/darker shades represent regions of lower FLAP abundance (n=3). Scale bar is 5 µm. Also, see Supplementary Movie S2. **B** Box-whisker plots showing the sphericity of isolated nuclei obtained from 3D-reconstructed images. The whiskers indicate the range, and the boundary of the box closest to zero indicates 25th percentile, while the farthest one indicates 75th percentile. The line within the box represents the median and the red dots indicate data points from at least 36 cells (n=3). P values were determined using Tukey's multiple comparisons test with ordinary one-way ANOVA. **C** Representative 3D volumetric render of the nuclei isolated from PMNs stimulated with either DMSO or fMLF (100 nM) in the presence or absence of GW4869 (3 µM), and immunostained for ceramide (red), FLAP (green), and Hoechst (blue) (n=3). Scale shown on xyz-axis. Also, see Supplementary Movie S3. **D-E** Box-whisker plots showing the Mander co-occurrence coefficient **(D)** and Pearson's R-value **(E)** between FLAP- and ceramide-positive structures present on the NE under the indicated conditions, calculated using 3D-reconstructed multiple z-stack images. The whiskers indicate the range, and the boundary of the box closest to zero indicates 25th percentile, while the farthest one indicates 75th percentile. The line within the box represents the median and the red dots indicate all 34 datapoints of DMSO, 43 of fMLF, and 38 of fMLF + GW4869 (n=3). P values determined using ordinary one-way ANOVA, are indicated on the graph. Source numerical data and unprocessed blots are available in the source data file.

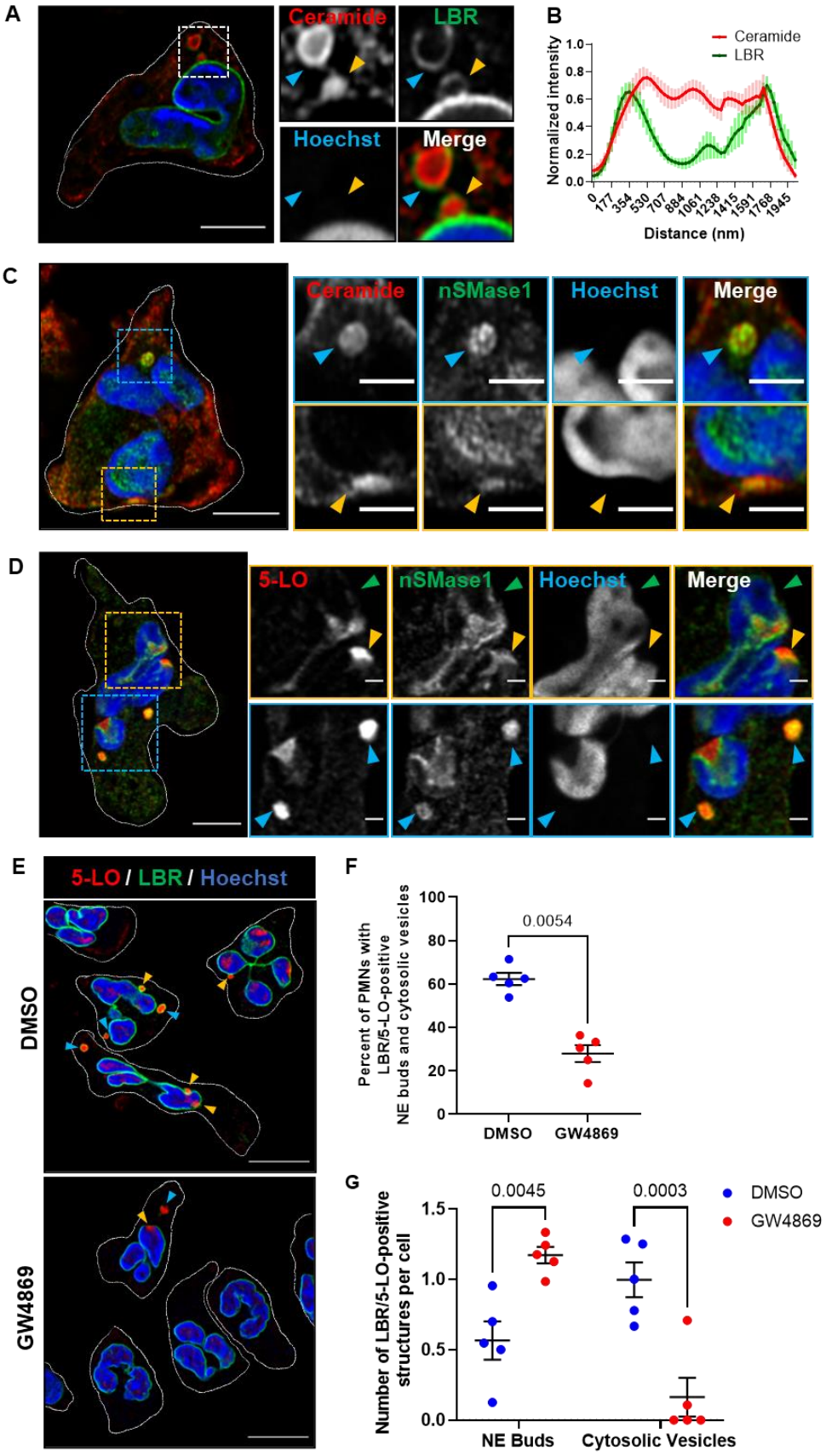
A
Ceramide
LBR
Hoechst
Merge
B
Ceramide
LBR
Normalized intensity
1.0
0.8
0.6
0.4
0.2
0.0
0
177
354
530
707
884
1061
1238
1415
1591
1768
1945
Distance (nm)
C
Ceramide
nSMase1
Hoechst
Merge
D
5-LO
nSMase1
Hoechst
Merge
E
5-LO / LBR / Hoechst
DMSO
GW4869
F
Percent of PMNs with LBR/5-LO-positive NE buds and cytosolic vesicles
100
80
60
40
20
0
0.0054
DMSO
GW4869
G
Number of LBR/5-LO-positive structures per cell
1.5
1.0
0.5
0.0
0.0045
0.0003
DMSO
GW4869
NE Buds
Cytosolic Vesicles

Figure 2.4: nSMase1 and ceramide are present within and are required for the generation of NE-derived 5-LO/LBR positive NE buds and cytosolic vesicles

A Representative Airyscan microscopy image of fixed PMNs chemotaxing towards 100 nM fMLF and stained for LBR (green) and ceramide (red) (n=4). The yellow arrowheads point to nuclear buds and the blue arrowheads point to cytosolic vesicles. Scale bar is 5 µm. In the inset, it is 1 µm. **B** Histogram showing the normalized intensity of LBR and ceramide across the maximum width of the LBR-positive vesicles. Data are represented as mean ± SEM of 10 NE buds or cytosolic vesicles from three independent experiments. **C** Representative Airyscan microscopy images of fixed PMNs chemotaxing towards 100 nM fMLF and stained for nSMase1 (green) and ceramide (red) (n=3). The yellow arrowheads point to nuclear buds and the blue arrowheads point to cytosolic vesicles. Scale bar is 5 µm, in the inset it is 2 µm. **D** Representative Airyscan microscopy images of fixed PMNs chemotaxing towards 100 nM fMLF stained for 5-LO (red) and nSMase1 (green) (n=3). The yellow arrowheads point to nuclear buds and the blue arrowheads point to cytosolic vesicles. Green arrowheads point to the 5-LO and nSMase1 on the NE. Scale bar is 5 µm. In the inset it is1 µm. **E** Field Airyscan microscopy image of fixed PMNs chemotaxing towards 100 nM fMLF in the presence or the absence of 3 µM GW4869 stained for 5-LO (red) and LBR (green). Scale bar is 10 µm. The yellow arrowheads point to nuclear buds and the blue arrowheads point to cytosolic vesicles.**F** Scatter plots showing the percentage of PMNs in DMSO- or GW4869-treated PMNs containing LBR/5-LO-positive NE buds and cytosolic vesicles among the total cells quantified within randomly selected imaging fields. A total of 158 cells in the DMSO sample and 108 cells in GW4869 samples from 5 independent experiments were analyzed and plotted (red dots) as mean ± SEM. P values were determined using a two-tailed paired t-test. **G** Scatter plots showing the changes in the number of LBR/5-LO-positive buds and cytosolic vesicles per cell in PMNs treated with GW4869 compared to DMSO control. The data points from five independent experiments (red dots) are plotted as mean ± SEM, and P values determined using two-way RM ANOVA are reported. Source numerical data are available in the source data file.

ultracentrifugation revealed that the levels of the canonical exosome markers CD63, Flotillin 2, and TGS101 peaked in the higher density fraction 9 compared with FLAP and the ESCRT-associated protein ALIX (van Niel, D'Angelo et al. 2018), which appeared more uniformly distributed throughout fractions 4-9 (

Figure 2.12**A, B**). We next used anti-CD63 antibody immunoprecipitation of the exosomes pooled from fractions 4-9 of fMLF activated PMNs to compare the composition of CD63-positive and flowthrough exosome populations. We found that while Flotillin 2 was present in both CD63-positive and flowthrough exosome preparations, CD63-positive exosomes showed decreased levels of FLAP, 5-LO, and ALIX with a concomitant enrichment in the flowthrough fraction (**Figure 2.5G, H**). These results are supported by the exclusion of CD63 signal from LBR-positive NE buds and cytosolic vesicles (**Figure 2.5E, F**) and the substantial recruitment of ALIX to LBR- or FLAP-positive NE buds and cytosolic vesicles in PMNs chemotaxing towards fMLF (**Figure 2.5I, Figure 2.13**). From these findings we conclude that the NE-derived and nSMase1-dependent 5-LO- and FLAP-positive exosomes are synthesized in a CD63 independent manner.

2.4 Discussion

Neutrophil infiltration and exit into and from sites of infection/injury are crucial for potent inflammatory response and tissue homeostasis. Neutrophils are endowed with a highly malleable multilobed nucleus enriched with LBR and expressing high levels of Lamin B1 and relatively low levels of Lamin A/C (Manley, Keightley et al. 2018). This unique nuclear architecture has been implicated in neutrophil extravasation and squeezing through tight spaces during migration (Rowat, Jaalouk et al. 2013). The LTB_4 signaling pathway plays a key role during neutrophil chemotaxis *in vitro (Majumdar, Tavakoli Tameh et al. 2021)* and *in vivo*

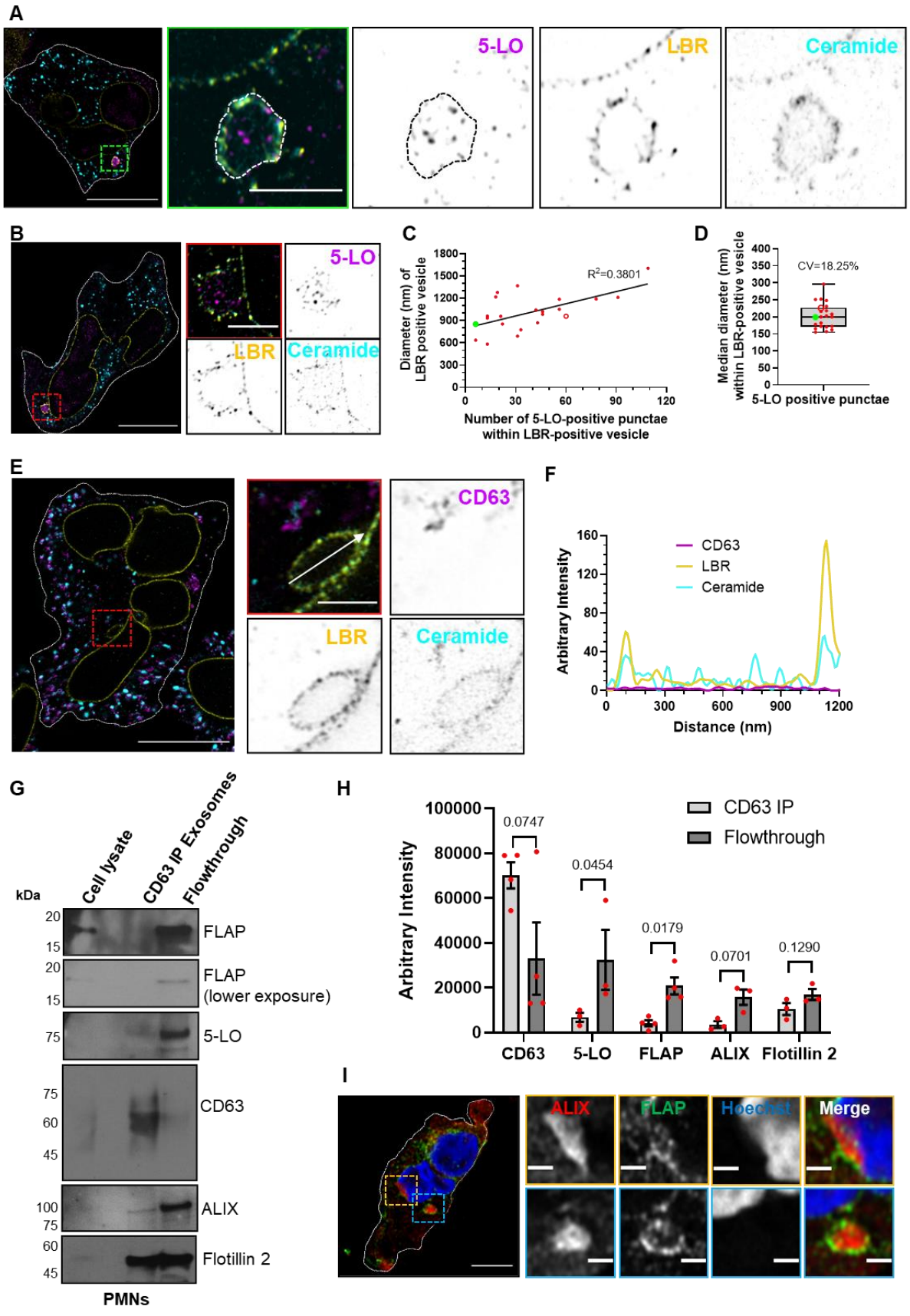
A
5-LO
LBR
Ceramide
B
5-LO
LBR
Ceramide
C
Diameter (nm) of LBR positive vesicle
R²=0.3801
Number of 5-LO-positive punctae within LBR-positive vesicle
D
Median diameter (nm) within LBR-positive vesicle
CV=18.25%
5-LO positive punctae
E
CD63
LBR
Ceramide
F
CD63
LBR
Ceramide
Arbitrary Intensity
Distance (nm)
G
Cell lysate
CD63 IP Exosomes
Flowthrough
kDa
FLAP
FLAP (lower exposure)
5-LO
CD63
ALIX
Flotillin 2
PMNs
H
CD63 IP
Flowthrough
Arbitrary Intensity
0.0747
0.0454
0.0179
0.0701
0.1290
CD63
5-LO
FLAP
ALIX
Flotillin 2
I
ALIX
FLAP
Hoechst
Merge

Figure 2.5: 5-LO-positive and CD63-negative punctae are present within LBR-positive vesicles
A-B Four-fold expansion images of fixed human PMNs chemotaxing towards 100 nM fMLF, acquired using Airyscan microscopy, stained for 5-LO (magenta), LBR (yellow), and ceramide (cyan) within cytosolic vesicles **(A)** and NE buds **(B)**, are represented as inverted grayscale zoomed images (n=3). Scale bar is 5 µm. In the inset, the scale bar is 800 nm.
C Scatter plot showing the non-linear regression of the diameter of LBR positive vesicles versus the number of 5-LO positive punctae per LBR-positive vesicle.
D Box-whisker plot showing the distribution of the median diameter of 5-LO-positive punctae per LBR-positive vesicle. The whiskers indicate the range, and the boundary of the box closest to zero indicates 25^{th} percentile, while the farthest one indicates 75^{th} percentile. The line within the box represents the median and the red dots indicate datapoints obtained from 22 LBR-positive vesicles quantified from 10 cells (n=2). In panels C and D, the blue dot and open red dot represent data points from panels A and B, respectively.
E Four-fold expansion microscopy image of fixed human PMNs chemotaxing towards 100 nM fMLF, acquired using Airyscan microscopy, stained with CD63 (magenta), LBR (yellow), and ceramide (cyan) within an NE-derived vesicle, represented as inverted grayscale zoomed images (n=3). Scale bar is 800 nm, and in the uncropped image it is 5 µm.
F Histogram showing the arbitrary intensity of LBR, ceramide, and CD63 across the white arrow along the LBR positive bud shown in zoomed and merged image in panel E.
G Representative western blot of exosomes obtained from fractions 4-9 of the density gradient centrifugation from PMNs stimulated with 100 nM fMLF and immunoprecipitated using an antibody against CD63 (n=3-4). CD63-positive and CD63-negative (unbound flowthrough) populations were immunoblotted for FLAP, 5-LO, CD63, ALIX, and Flotillin 2.
H Bar graph showing the quantifications of the band intensity of CD63, 5-LO, FLAP, ALIX, and Flotillin 2 in CD63-IP and flowthrough fractions. Four data points for FLAP and CD63, and three for 5-LO, ALIX, and Flotillin 2 are plotted as mean ± SEM where each red dot represents the value from one experiment. P values determined using a two-tailed ratio paired t-test are reported.
I Representative Airyscan microscopy images of fixed PMNs chemotaxing towards 100 nM fMLF and stained for FLAP (green) and ALIX (red) (n=3). Scale bar is 5 µm. In the inset, the scale bar is 1 µm. NE buds are shown in yellow boxes and cytosolic vesicles are shown in blue boxes. Source numerical data and unprocessed blots are available in the source data file.

(Lammermann, Afonso et al. 2013) as well as during extravasation (Miyabe, Miyabe et al. 2019, Subramanian, Melis et al. 2020). We now show that the biogenesis of exosomes containing the LTB_4-synthesizing machinery originates at sites of NE budding during neutrophil chemotaxis. Our study identifies nSMase1 as critical for the generation of NE-derived buds and cytosolic vesicles and the subsequent release of FLAP/5-LO-containing exosomes. More importantly, we report that nSMase1 localization on the NE is required for ceramide production, which leads to the generation of lipid-ordered nuclear membrane microdomains and the recruitment of FLAP/5-LO at sites of NE buds. The induction of membrane curvature required for vesicle budding is generally mediated by (i) lipid composition, (ii) protein motif insertion, and/or (iii) clustering of membrane proteins of defined shapes (McMahon and Boucrot 2015). Ceramide and its glucoside derivative GM1 are known to facilitate membrane budding by inducing negative and positive membrane curvature, respectively (Dasgupta, Miettinen et al. 2018, Sarmento, Ricardo et al. 2020). The enrichment of these lipids at sites of nuclear budding underscores their role in the initiation of FLAP/5-LO-containing NE buds. Moreover, the induction of positive membrane curvature mediated by the insertion of the C2-domain of $cPLA_2$ and lysoPC, the byproduct of $cPLA_2$ activity (Ward, Ropa et al. 2012), may facilitate the budding of the vesicle from the NE. Indeed, $cPLA_2$ was recently proposed to act as a molecular sensor of nuclear membrane tension in migrating cancer cells and zebrafish (Lomakin, Cattin et al. 2020, Venturini, Pezzano et al. 2020). Notably, the released AA through $cPLA_2$ activation is a key factor in LTB_4 biogenesis, where it was shown to not only induce FLAP trimerization (Ferguson, McKeever et al. 2007) and act as the substrate for 5-LO but also as an activator of nSMases and ceramide production (Jayadev, Hayter et al. 1997). We, therefore, propose that the clustering of FLAP, along with the incorporation of ceramide, induces membrane curvatures that are required for NE-derived bud formation. However, as we observe the presence

of the INM protein LBR on 5-LO- and FLAP-positive cytosolic vesicles, the transformations needed to generate an MVB from the two NE membranes remain unknown. Interestingly, the emergence of MVBs from the NE has previously been reported in other cell types (Kilarski and Jasiński 1970, Conti and Klein-Szanto 1973), where MVBs appear to be enclosed in two membranes. Since ALIX facilitates the sorting of membrane-associated tetraspanin cargos to ILVs/exosomes (Larios, Mercier et al. 2020) and as FLAP is structurally similar to tetraspanin proteins (Ferguson, McKeever et al. 2007), the presence of ALIX within FLAP-positive NE buds and cytosolic vesicles in chemotaxing PMNs also suggests that ALIX is involved in the generation of FLAP/5-LO-positive ILVs. Furthermore, ALIX recruits the ESCRT III complex protein CHMP4B, which is known to induce membrane curvature during vesicle fission and ILV formation (McCullough, Fisher et al. 2008). Finally, as we found that the absence of nSMase1 significantly downregulates the secretion of a larger (>180 nm) 5-LO-positive exosome population that originates within LBR-positive and CD63-negative MVBs, we propose that activated neutrophils release at least two structurally, biochemically, and functionally distinct exosomes populations: namely non-conventional NE-derived and conventional exosomes. Indeed, exosome heterogeneity based on size/density (Willms, Johansson et al. 2016), cargo type (Song, Tian et al. 2021), and the mechanism of ILV generation (Matsui, Osaki et al. 2021), has recently been reported. We envision that the unique characteristics for the neutrophil nuclei provide a specialized environment for the release of nuclear material during chemotaxis.

2.5 Materials and Methods

2.5.1 Ethics statement

Human neutrophils were isolated from blood obtained from anonymous healthy human donors form the Platelet Pharmacology and Physiology Core at the University of Michigan. The

blood was attained through an IRB-approved (IRB#HUM00107120) protocol specifically approved to provide de-identified blood for research purposes. We therefore did not have access to the HIPAA information. All subjects were consented and agreed to provide their blood for research purposes and were financially compensated.

2.5.2 Isolation of human peripheral blood neutrophils

Heparinized whole blood from anonymous healthy human donors that had not taken aspirin for 7 days and NSAIDS for 48 hours was obtained by venipuncture from the Platelet Pharmacology and Physiology Core at the University of Michigan. Neutrophils were isolated using the protocol described earlier (Kremserova and Nauseef 2020). Briefly, whole blood was incubated with an equal volume of 3% dextran (sigma D1037) in 0.9% NaCl for 30 min at 37˚C to facilitate RBC sedimentation. Three volumes of plasma containing platelets monocytes, lymphocytes, and neutrophils were overlayed onto a volume of Histopaque-1077 (Sigma 10771) and centrifuged at 400Xg for 20 min at room temperature to separate peripheral blood mononuclear cells from neutrophils. Residual erythrocytes in the neutrophils pellet were removed using ACK lysing buffer (Thermo Fisher A1049201). The protocol yields >99% live neutrophils with >95% purity.

2.5.3 Cell lines and plasmid constructs

The human myeloid leukemia-derived pro-myelocytic cell line HL-60 was obtained from ATCC (CCL-240™) and maintained in RPMI-1640 media containing 10% HI-FBS, 20 mM HEPES pH 7.4, and penicillin-streptomycin antibiotic cocktail. HL-60 cells are also known as PLB-985 cells, which were originally reported in 1987 to arise from an acute myeloid leukemia patient different from the HL-60 cells (Tucker, Lilly et al. 1987). However, in 2003, Drexler and colleagues determined that the PLB-985 cells are actually a sub-clone of HL-60 cells (Drexler,

Dirks et al. 2003). Our PLB-985 cells were authenticated using STR analysis and showed to be a 93% match with HL-60 Promyelocytic Leukemia Human cells (ATCC #CCL-240; see **Supplementary Table 1**). We therefore now refer to them as HL-60 cells in this work and future work form our laboratory. To generate neutrophil-like cells HL-60 were differentiated in culture media containing 1.3% DMSO for 6 days with a change to fresh media every other day as described by Saunders *et al* (Saunders, Majumdar et al. 2019). HEK293T cells obtained from ATCC (CRL-3216™), cultured in DMEM containing 10% FBS were used to generate lentiviral particles for the generation of stable HL-60 cell lines. pVSVG, pCMV dR8.91, and pLentiCRISPR V2 vector expressing SCR/nSMase1 sgRNA or pCDH MSCV MCS EF1 neomycin vector expressing nSMase1 fused with eGFP at the C-terminal were transfected to HEK293T at the ratio of 1:2:4 using Lipofectamine 3000 transfection reagent. The lentiviral particles collected after 48- and 72-hours post-transfection were pooled, concentrated using PEG-it (Systems Biosciences LV810A-1), and added to the HL-60 cells with 8ug/ml polybrene. The clones expressing the construct were selected in 2 µg/ml puromycin and verified by western blotting and genetic sequencing. The SMPD2 sgRNA #1; GCCGACCGCATGAGGCGCCT, and sgRNA#; GAACCAGGAGAGCTTCGACC were cloned in pLentiCRISPR V2 plasmid, which was a kind gift from the Zhang lab. Full-length SMPD2 (NM_003080) was amplified from the cDNA pool generated using oligo dT primer based SuperScript^{TM} IV First-Strand Synthesis System (Thermo Fischer 18091050) kit, using RNA extracted from dHL60 cells. Gene-specific primers: 5' GGAATTCGCCACCATGAAGCCCAACTTCTC 3' and 5' CCGCTCGAGTTGTTCTTTAGTTCTGTCC 3', were used to amplify SMPD2 with 5' EcoRI and 3' XhoI RE sites. The fragment was cloned in pCDH MSCV MCV EF1 Neomycin vector upstream to 5' XhoI-EGFP using T4 DNA ligase.

2.5.4 Isolation of intact nuclei for microscopy and the purification of the nuclear membrane microdomains

The protocol is based on and modified from the DRM isolation protocols by Persaud-Sawin *et al.*(Persaud-Sawin, Lightcap et al. 2009) and Cascianelli *et al.* (Cascianelli, Villani et al. 2008), as is shown in Extended data Figure 3. dHL-60 or PMNs were resuspended in 1X mHBSS (150 mM NaCl, 4 mM KCl, 1.2 mM $MgCl_2$, 10 mg/ml Glucose, 20 mM HEPES pH 7.4) at a density of 10e6/ml. The cells were treated with either DMSO or 100 nM fMLF (Sigma Aldrich F3506) in the presence or absence of 3 μM GW4869 (Sigma Aldrich D1692) for 5 min at 37˚C with 10 RPM rotation. The cells were further incubated with an equal volume of 20 mM dimethyl pimelimidate (DMP) crosslinker (TCI chemicals D4476) in 1X mHBSS for 15 min at 37˚C, washed in 20 mM Tris-Cl (pH 8.0) at 500Xg for 5 min at 4˚C, and partially lysed twice with 15X trituration in ice-cold hypotonic lysis buffer (10 mM HEPES pH 7.5, 4 mM $MgCl_2$, 25 mM NaCl, 1 mM DTT, and 0.1% NP-40) at a density of 50e6/ml. After centrifugation at 16,000Xg at 4˚C for 10 sec, supernatants were saved as vesicle containing cytosol fractions. To remove ER fragments (microsomes), Golgi, and mitochondria, the nuclear pellet was washed with ice-cold Barnes solution (85 mM KCl, 85 mM NaCl, 2.5 mM $MgCl_2$, 5 mM trichloroacetic acid pH 7.4) (Albi, Lazzarini et al. 2003). For immunostaining, the purified nuclei were resuspended in ice-cold isotonic resuspension buffer (10 mM HEPES pH 7.4, 4 mM $MgCl_2$, 150 mM NaCl, 1 mM DTT, 250 mM Sucrose) at a density of 1e6/ml for microscopy, added to the poly-L-lysine coated glass coverslip, spun at 500Xg for 5 min at 4˚C and fixed with 4% paraformaldehyde in isotonic resuspension buffer for 15 min at room temperature. For the isolation of lipid microdomains, nuclei were further lysed in 650 μl ice-cold TNE buffer (50 mM tris-Cl pH 7.4, 150 mM NaCl, 5 mM EGTA) containing 4 mM $MgCl_2$ and 1% Triton X-100. The suspension was passed through a 23

G needle 30X and incubated on ice for 30 min. The NE supernatant was collected at 110Xg for 10 min at 4˚C and adjusted to 40% iodixanol concentration using 60% Optiprep solution (Sigma D1556) and overlayed with 7 ml of 30% iodixanol, 2 ml of 20% iodixanol, and 1 ml of 5% iodixanol solution in TNE buffer, in a 13 ml ultracentrifuge tube. Sixteen fractions of 750 µl each from the top (F1) were collected after centrifugation at 150,000Xg for 16 hours at 4˚C. One-fifth of the volume of the individual fraction was used to extract lipids by the methanol-chloroform based lipid extraction (Moltu, Bjørgo et al. 2013). Briefly, 150 µl sample was thoroughly mixed with 450 µl of chloroform: methanol (2:1) for 15 min at room temperature followed by the addition of 100 µl distilled water, vortexed and centrifuged at 1,000Xg for 15 min at room temperature, which yield lipids in the bottom organic layer, which were dried under nitrogen gas in fume hood, and resuspended in 20 µl chloroform: methanol (2:1). The rest of the fraction volume was used to concentrate protein by the TCA-acetone method, and proteins were resuspended in 75 µl of 1X Laemmli sample buffer and boiled at 95˚C for 10 min before loading on 4-12% Bis-Tris gel for electrophoresis. The electrophoresed proteins were transferred to 0.2-micron PVDF membrane, blocked using 1X Fish gelatin (Fischer Scientific NC0382999) in TBS containing 0.1% Tween-20 and probed for specific proteins using antibody against FLAP (1 µg/ml, Abcam 85227), 5-LO (1:1000, Abcam 169755), Flotillin 2 (1:1000, CST 3436), nSMase1 (1:500, CST 3867), and Lamin B1 (1:1000, Abcam 133741). The lipids (5 µl) were spotted on the nitrocellulose membrane, blocked with 1X fish gelatin in DPBS and dot blots were probed with 1 µg/ml CF®568-conjugated cholera toxin (Biotium 00071) in DPBS for GM1 and with mouse anti-ceramide antibody (1:500, Sigma C8104-50TST) followed by the Rhodamine Red™-X-conjugated goat anti-mouse IgM µ-chain specific secondary antibody (1:500, Jackson Immuno research 115-297-020) to detect ceramide.

2.5.5 Under agarose chemotaxis assay, live imaging and immunofluorescence microscopy

The chemotaxis assay was performed as described by Saunders *et al* (Saunders, Majumdar et al. 2019). Cell culture dishes were coated with 1% BSA in DPBS at 37˚C for 1 hr. 0.5% agarose in DPBS: HBSS (1:1) was poured and allowed to solidify for 45 min. Three 1 mm diameter wells were carved 2 mm from each other. fMLF (100 nM) in HBSS was placed in the middle well creating a gradient of 50 pM/µm as described by Afonso and colleagues (Afonso, Janka-Junttila et al. 2012). A total of 50,000 cells in 5 µl mHBSS were plated in the outer wells and incubated at 37°C. The chemotaxing cells were imaged under a 63X oil objective in a temperature-controlled chamber set at 37˚C. Images of nSMase1-GFP expressing HL-60 cells were acquired at 10-sec intervals, using Airy disk imaging array "Airyscan" to rapidly achieve resolution beyond the diffraction limit (140 nm at 488 nm). The acquired images were reconstructed using the Airyscan processing tool using the Zen imaging software and were converted to a movie using Fiji. For immunostaining, the PMNs were allowed to chemotax for 1 hr and fixed with 4% PFA in HBSS for 20 min at 37˚C. The agarose was removed and PMNs were blocked for 1 hour at room temperature followed by staining in blocking buffer (0.2% saponin, 2% goat serum in 1X mHBSS) at 4˚C overnight with antibodies against FLAP (1µg/ml, Abcam 85227), 5-LO (1:500, BD biosciences 610694), nSMase1 (1:100, Abcam 131330), and Lamin B1 (1:100, Proteintech 66095-1), LBR (1:400, Abcam 32535), LTA_4H (1:100, Santacruz biotechnology sc23070), Ceramide (1:50, Sigma C8104-50TST), CD63 (1:800, BD biosciences 556019), and ALIX (1:200, Abcam 117600). The PMNs were washed with HBSS 3X for 5 min each and incubated with Alexa fluor-conjugated secondary antibody (1:500, Invitrogen A11008, A11031) along with 1 µg/ml of Hoechst 33342, for 1 hr at room temperature. The washed PMNs were mounted with Immumount™ (Fischer Scientific FIS9990402), z-stacks were acquired at an interval of 160 nm,

using 63x objective in Zeiss LSM 880 confocal microscope fitted with Airyscan, and the acquired images were reconstructed using Airyscan processing in Zen 3.4 Blue edition software. The immunostaining of isolated fixed nuclei was performed in non-permeabilizing conditions (2% goat serum in DPBS).

2.5.6 Di-4ANEPPDHQ fluorescence imaging

The image acquisition and anisotropy quantification were performed as described earlier by Owen *et al* (Owen, Rentero et al. 2011). Briefly, cells were incubated with HBSS containing 1 µM di-4ANEPPDHQ (ThermoFisher D36802) and Hoechst for 30 min at 37°C, washed, and added to the under agarose well as described above. Cells chemotaxing towards fMLF were imaged using a 63X oil immersion lens at 37˚C. di-4NEPPDHQ fluorescence was excited using 488 nm argon laser, and the emission was collected at 500–580 nm (L_o) and 620–750 (L_d) nm range, respectively. Hoechst was excited using a 405 nm laser and the signal was captured using a simultaneous line scanning approach on a Zeiss 880 Airyscan microscope. Images were captured at 10-sec intervals and reconstructed by Airyscan processing. Generalized polarization (GP) images were created based on the methodology outlined by Owen *et al* (Owen, Rentero et al. 2011). To calculate the perinuclear GP shift, the brighter lipid ordered (L_o, green) channel was used to create a mask of the whole cell and the perinuclear mask with a width of 15 pixels was created using Hoechst image. The cell cytosol area was obtained by subtracting the perinuclear mask from the whole-cell mask. The GP value of every pixel in both the perinuclear area and the cytosol area was calculated using the formula below:

$$GP= (I_{500-580}-GI_{620-750})/(I_{500-580}+GI_{620-750})$$

Where $I_{500-580}$ and $I_{620-750}$ are pixel intensities acquired in the L_o and L_d emission channels and G is the calibration factor manually adjusted to center the GP histogram of cytosol area around zero.

GP distributions were obtained from the binned GP values and fitted into non-linear Gaussian using GraphPad Prism. Finally, after fitting the GP histograms of the cytosol area and perinuclear area, the GP shift = the median value of GP perinuclear histogram - the median value of GP cytosol histogram.

2.5.7 Exosome isolation, immunoprecipitation and LTB_4 ELISA

Exosome isolation was performed following the guidelines described by Thery *et al* (Théry, Witwer et al. 2018). PMNs or Scr and nSMase1 KO HL-60 cells were stimulated with 100 nM fMLF in RPMI-1640 containing 10 U/ml DNaseI (Sigma Aldrich DN25) for 30 min at 37ºC and the supernatants were collected at 500Xg at 4˚C for 5 min. The microvesicles and apoptotic bodies were removed at 4000Xg for 20 min followed by filtration through a 0.2 µm polyethersulfone membrane filter. The extracellular vesicles (EVs) present in the filtered supernatant were concentrated with 8% PEG-6000 (Bio Basic PB0432) in 20 mM HEPES and 500 mM NaCl, at 4˚C for 36 hrs, followed by centrifugation at 4000Xg at 4˚C for 1 hr. The concentrated EVs, resuspended in 1 ml 250 mM sucrose and 20 mM Tris-Cl pH 7.4, were overlayed on the top of optiprep gradients and centrifuged at 100,000Xg for 16 hrs at 4˚C. The optiprep gradients were prepared in 250 mM sucrose and 20 mM Tris-Cl, starting from the bottom as 3 ml of 40% optiprep, 3 ml of 20% optiprep, 3 ml of 10% optiprep, and 2 ml of 5% optiprep. The fractionated exosomes were collected as 12 fractions of 1 ml each from the top (lower to higher density).

For exosome immunoprecipitation, fractions 4-9 (Iodixanol density 1.083-1.142 g/ml) as described in Majumdar *et al* (Majumdar, Tavakoli Tameh et al. 2021) were pooled, diluted in DPBS, centrifuged at 100,000Xg for 1 hr, resuspended in DPBS containing 1% 0.2 µm filtered BSA, and incubated with anti-CD63 antibody-conjugated magnetic beads (Thermo Scientific

10606D) overnight at 4˚C with 10 RPM rotation. The CD63-specific bead-bound exosomes were separated using DynaMag^{TM} magnets (Thermo Scientific 12321D) and washed once with DPBS containing 1% BSA. The supernatant containing unbound exosomes was collected and centrifuged at 100,000Xg for 1 hr. The unbound exosome pellet and the CD63 positive bead-bound exosomes were lysed in RIPA buffer for 15 min on ice, boiled in an equal volume of 2X reducing Laemmli buffer at 95˚C for 5 min, loaded in 4-12% bis-tris gel, electrophoresed, and transferred to PVDF membrane for western blotting with anti-ALIX antibody (1:1000, Abcam 117600), anti-CD63 antibody (1:500, BD biosciences 556019), anti-Flotillin 2 antibody (1:1000, cell signaling technology 3436), anti-5-LO antibody (1:1000, Abcam 169755) and anti-FLAP antibody (1µg/ml, Abcam 85227), and detected using protein A-HRP (1:5000, Invitrogen 101023).

The LTB_4 ELISA kit (Cayman Chemicals 520111) was used to assess the LTB_4 levels within the exosomes. The isolated exosomes were homogenized in 100 µl ELISA buffer using a 3 mm diameter sonicator probe at an amplitude of 20% with 2 sec ON/OFF cycles for a total of 10 cycles on ice. To detect LTB_4 concentrations within the linear range, 50 ul of concentrated homogenate was diluted 4X in ELISA buffer and LTB_4 levels were quantified according to the manufacturer's instructions. The values obtained were plotted using GraphPad prism.

2.5.8 Nano-tracking analysis

The data for NTA was captured using a Malvern Nanosight NS300 equipped with a 488 nm laser and a high sensitivity sCMOS camera and analyzed using the NTA 3.3 Dev Build 3.3.301 software. The exosomes purified using optiprep-density gradient centrifugation were resuspended in DPBS, vortexed, and diluted to 1:1000 in 0.22 µm filtered particle-free water to obtain a recommended concentration range of 1-10 × 10^8 particles/ml for reliable measurement. Using a syringe pump speed of 100/AU to inject exosome suspension in the flow channel, videos of the

particle's inflow were captured in script control mode, as 5 videos of 60 s each with 1 s delay and viscosity of water at 25°C. A total of 1,500 frames/sample at a capture rate of 25 frames/sec at constant camera level for each experimental set were captured.

2.5.9 Expansion microscopy

To maintain the structural integrity of PMNs, samples were processed with a few modifications from the protocols described earlier (Gambarotto, Zwettler et al. 2019, Truckenbrodt, Sommer et al. 2019). PMNs migrating under 3 ml of agarose over a 22x22 mm glass coverslip (#1.5, BSA coated) in a 35-mm dish were fixed with 1 ml of 4% PFA and 0.05% glutaraldehyde in PHEM buffer (60 mM PIPES, 25 mM HEPES, 10 mM EGTA and 2 mM $MgCl_2$, pH 6.9) at 37ºC for 20 min. After careful removal of the agarose, the fixed cells were immunostained in saponin-containing buffer, as described above. Post staining, the cells on the coverslips were washed thrice with 1X PBS and crosslinked with 3 mM Acryloyl-X, SE (Sigma Aldrich A20770) in 1X PBS, overnight at room temperature. To remove residual cross-linker, cells were washed thrice with 1X PBS for 15 min each at room temperature. The coverslips were incubated with an 80 µl drop of gelation solution comprising 8% sodium acrylate (Sigma Aldrich 408220), 10% Acrylamide (Sigma Aldrich 4058), 0.1% bisacrylamide (Sigma Aldrich M1533), 2M NaCl, and 1X PBS containing 1% heat-induced initiator VA-044 (Fischer scientific A3012), at 4ºC for 10 min. The coverslip was assembled in the gelation chamber as illustrated by Truckenbrodt *et al.*(Truckenbrodt, Sommer et al. 2019), 200 µl of gelation solution was added, and the gelation chamber was incubated in a humidified chamber at 37ºC for a minimum of 2 hrs to allow polymerization. The gelation chamber was disassembled and the gel on the coverslip was washed quickly with 1X PBS to remove the unpolymerized gel. The gel was treated with 2 ml of the digestion buffer consisting of 50 mM Tris-Cl, 800 mM Guanidine hydrochloride, 1 mM EDTA,

and 0.5% Triton-X 100 adjusted to pH 8.0, with 8 U/ml of proteinase K (NEB P8107S) added just before use, in a 35 mm dish, at 37ºC for 1 hr. The gel containing the homogenized sample was washed thrice with 1X PBS (2 ml each) for 15 min each at room temperature. The gel was slid carefully into a 100 mm dish to allow for gel expansion, by sequentially changing the buffer to 10 ml of 1X>0.5X>0.02X>0.01X PBS for 20 min each at room temperature, followed by incubation in ddH_2O overnight at 4ºC. Gel size both before and after the expansion was measured using a ruler and was found to be approximately 4X lengthwise. Gel pieces containing the cells were excised to fit into a 12 mm glass-bottom 35 mm dish coated with poly-L-lysine (Sigma Aldrich P8920). The gel was gently pressed using a soft painting brush to ensure its adherence to the coverslip and avoid gel drift during imaging. 100µl ddH2O was slowly added to the empty spaces of the chamber to cover the gel and avoid the shrinking of the polymer. The sample was imaged using a Zeiss 880 confocal microscope fitted with an Airyscan detector, under a 63X (1.4NA) oil objective. Since Airyscanning provides 120 nm lateral and 350 nm axial resolution (Huff, Bergter et al. 2017), using 4X expansion of the sample has increased the resolution between 30-40 nm laterally and approximately 100 nm axially. The z-stacks acquired at an interval of 160 nm were ~50 nm apart, after expansion adjustment. All the scales shown in the images were after 4X adjustment, as verified by measuring the CD63 positive MVB size (~400 nm post adjustment). All the zoomed images representing buds/vesicles were deconvoluted using fast iterative algorithm and were used for presentation and data quantification.

2.5.10 Image quantification and data representation

Nuclei sphericity as presented in figure 3B, was quantified from z-stacks of Hoechst-stained nuclei. Briefly, the entire stack is converted to 8-bit and intensity thresholded (Otsu) with dark background for individual images. Volume, surface area, and sphericity were calculated using

analyze>analyze 3D options of MorphLibJ plugin. To quantify the colocalization between ceramide and FLAP in the nuclei, 3D images were thresholded using maximum entropy parameters, and Pearson's R-value and Mander colocalization coefficients (figure 3D) were determined using the JaCoP plugin in Fiji image analysis software. Intensity profiles of RGB channels (Figures 1D, 1F, 4B, 5F, and Extended data figure 5B) across the diameter of the vesicle of interest were determined using the RGB profiler plugin (https://imagej.net/plugins/rgb-profiler) from the Fiji image analysis tool. The resulting data was exported to GraphPad prism and plotted as histograms with mean ± SEM. The size of LBR-positive vesicles presented in figure 5C and Extended data figure 1B, was determined by manually drawing a line across the max diameter of the vesicle MFI projection image and quantifying the difference between the max intensity of LBR at the vesicle boundary. The size of CD63 vesicle presented in Extended data figure 5C was quantified as Feret diameter of the ROI around individual CD63-positive MVBs, as presented in the zoomed panel of Extended data figure 5A, using Analyze>Measure tool of Fiji image analysis software. The size of CD63 punctae as presented in Extended data figure 5E were quantified using Analyze regions 3D option of MorphLibJ plugin in Fiji software, from the CD63 images thresholded using Max entropy filter. The scale on the expansion microscopy images was adjusted 4X, and the size of LBR positive vesicles was determined by manually drawing an ROI and using the Measure option from the Fiji toolbar to determine the Feret diameter. The 5-LO channel was extracted, intensity thresholded using the Max entropy algorithm, and both the number and mean radii of 5-LO positive objects within the LBR-positive ROI were determined using Analyze>Analyze region 3D option in the MorphLibJ plugin of Fiji software. The data were exported to Microsoft Excel spreadsheet and plotted in Graphpad prism. The band intensities on the western blots were quantified using the Gels plugin from Analyze toolbar and were plotted in

GraphPad prism. To quantify the integrated pixel density of the spots obtained from the dot blots, circular ROI of uniform size was manually created, and the intensity was quantified using Analyze>Measure tool in Fiji image analysis tool. The 3D reconstruction of the z-stack images as presented in Figure 3A and 3C, were performed by exporting the Spectrum LUT (FLAP intensity) and olive pseudo color (Hoechst) images for figure 3A, and unmodified images for Figure 3C directly to Arivis Vision 4D 3.5 platform. In the software the volumetric rendering of the 3D images were performed using maximum intensity enabling projection of data along view direction. Rendered volumes were tilted to an angle of 125º and rotated along the Y-axis at 25 frames per second containing a total of 125 frames, to create a stereoscopic view.

2.5.11 Statistics and reproducibility

All data presented are from at least three independent biological replicates. An appropriate test of significance has been used to determine the level of confidence and variability in the data and mentioned in the corresponding figure legends.

2.6 Data availability

All the raw data and associated statistic calculations presented have been provided as "source data" for the respective figures. Owing to the large size of high-resolution z-stack microscopy images, the raw microscopy images are available from the corresponding author upon reasonable request

2.7 Acknowledgements

We thank the Platelet Pharmacology and Physiology Core at the University of Michigan for providing human blood from healthy volunteers. We are grateful to D. Cai and Y. Li (University of Michigan) for their assistance in the expansion microscopy experiments. We also

acknowledge R. Majumdar and C. Saunders as well as J. Y. Park for their intellectual contributions. Finally, many thanks to members of the Parent laboratory, and P. Hanson (University of Michigan) and P. Coulombe (University of Michigan) for their valuable suggestions and help during the progress of this work. This work was supported by funding from the University of Michigan School of Medicine (C.A.P.), by the Lucchesi Predoctoral Fellowship Award (S.C.), by an American Heart Association Predoctoral Award (F.J.-J.), and by R01 AI152517 (C.A.P.).

2.8 Author contributions

S.B.A., S.C., F.J.-J., and C.A.P. designed the experiments. S.B.A., S.C., and F.J.-J. performed the experiments and analyzed the results. S.B.A., S.C., and C.A.P. wrote and edited the manuscript. F.J.-J. edited the manuscript.

2.9 Competing interests

Authors declare no competing interests

2.10 Extended Figures

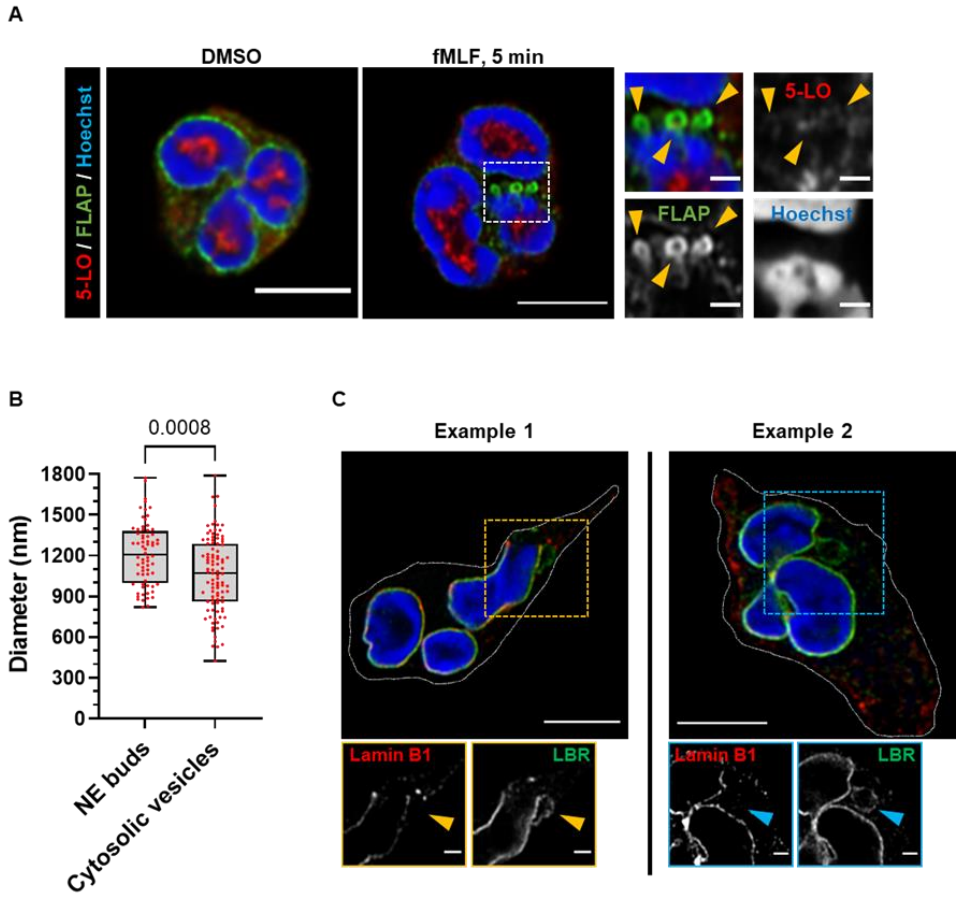

Figure 2.6: Characterization of LBR-positive NE buds and cytosolic vesicles.
A Representative Airyscan microscopy image of fixed PMNs uniformly stimulated with either DMSO or 20 nM fMLF showing the distribution of FLAP (green) and 5-LO (red) (n = 3). The yellow arrowheads point to nuclear buds. Scale bar is 5 µm, in the inset scale bar is 2 µm. **B** Box-whisker plots showing the size distribution of LBR-positive NE buds and cytosolic vesicles in PMNs chemotaxing towards fMLF (n = 5), where each red dot represents the value from the individual bud (68) and cytosolic vesicle (99), plotted as box-whisker plot with whiskers indicating the range. The boundary of the box closest to zero indicates 25th percentile, while the farthest one indicates 75th percentile, where the line within the box represents median. The indicated P value was determined using the two-tailed Mann-Whitney test. **C** Examples of fixed PMNs chemotaxing towards 100 nM fMLF and stained for LBR (green), Lamin B1 (red), and Hoechst (blue) acquired using Airyscan microscopy (n = 3). Scale bar is 5 µm, in the inset it is 1 µm. NE buds are shown in yellow boxes and cytosolic vesicles are shown in blue boxes. The yellow arrowheads point to nuclear buds and the blue arrowheads point to cytosolic vesicles. Source numerical data are available in the source data file.

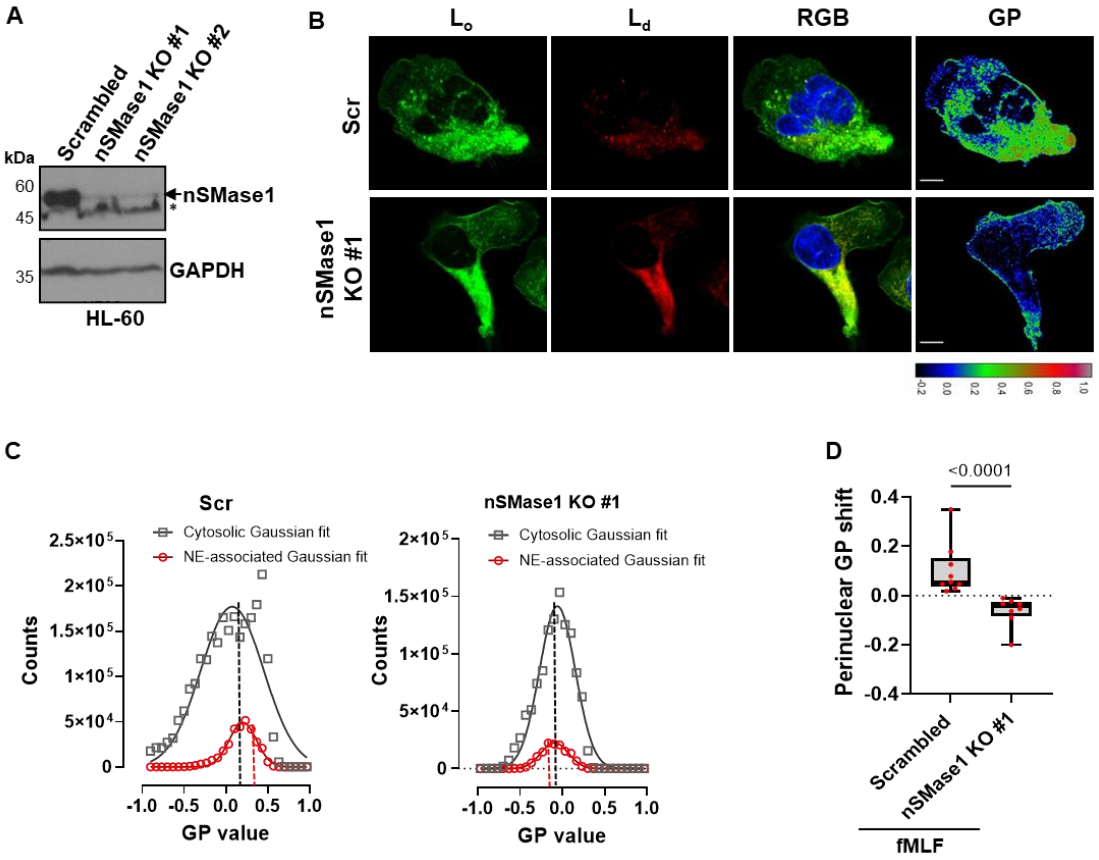

Figure 2.7: nSMase1 regulates fMLF-induced perinuclear lipid order.

A Representative western blot image showing the levels of nSMase1 in Scr or nSMase1 CRISPR KO HL-60 cell lysates. GAPDH was used as a loading control (n = 2). * Denotes non-specific band detected by the nSMase1 antibody. **B** Representative fluorescence microscopy images, showing the lipid-ordered (Lo) domains, lipid-disordered (Ld) domains, RGB images of Ld, Lo, and Hoechst merged, and GP images of either Scr or nSMase 1 KO dHL-60 cells chemotaxing towards 100 nM fMLF stained with di-4ANEPPDHQ (n = 3). Pseudo-colored GP images are based on the colormap, with white/red shades depicting lipid ordered regions and blue/darker shades representing lipid disordered regions. Scale bar is 5 µm. **C** Histogram depicting the gaussian distribution of the GP pixel intensity obtained from the cytosol and perinuclear ROI (as depicted in Fig. 2b). **D** Graph showing the median value of the perinuclear GP intensity distribution obtained from the GP images of Scr and nSMase1 KO dHL-60 cells. Data is quantified from 9 cells out of three independent experiments and is presented as box-whisker plot where whiskers indicate the range, and the boundary of the box closest to x-axis indicates 25th percentile, while the farthest one indicates 75th percentile and the line within the box represents the median. Each red dot represents the value from one cell. Indicated P value is determined using two-tailed Mann-Whitney test. Source numerical data and unprocessed blots are available in the source data file.

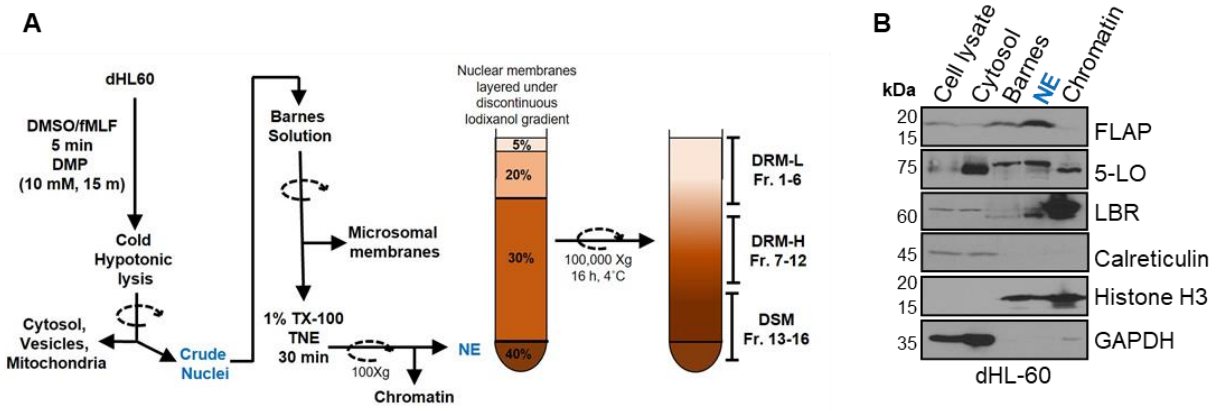

Figure 2.8: Characterization of NE membranes from WT dHL-60 cells.

A Schematic illustration of the methodology used to isolate DRM and DSM fractions from the isolated NE. **B** Representative western blot showing the efficiency of the fractionation protocol using resting WT dHL60 cells (n = 2). Scanned unprocessed blots are available in the source data file

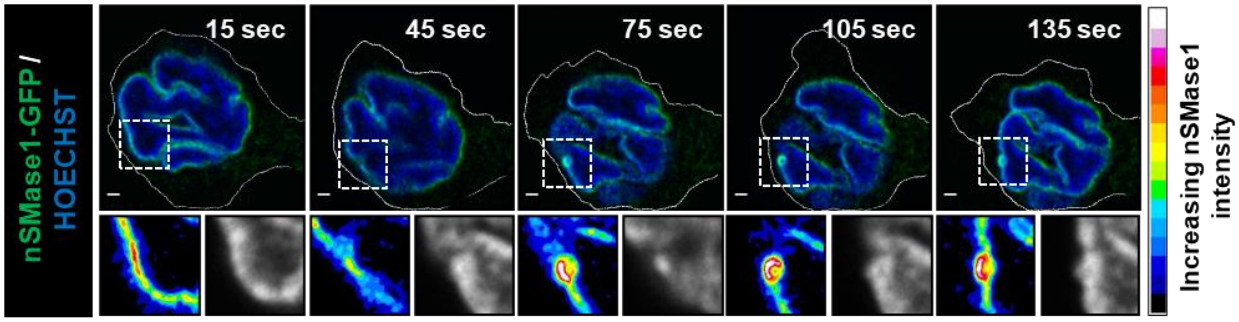

Figure 2.9: nSMase1-GFP is enriched at sites of nuclear budding.

Representative time-lapse images of dHL-60 cells expressing nSMase1-GFP chemotaxing towards 100 nM fMLF. The zoomed section of the images shows the nSMase1-GFP signal as fluorescence intensity spectrum (scale on right) and Hoechst in grayscale. Scale bar is 2 µm, in the zoomed images it is 1 µm. N = 6 cells acquired from two independent experiments. Also, see Supplementary Movie 4

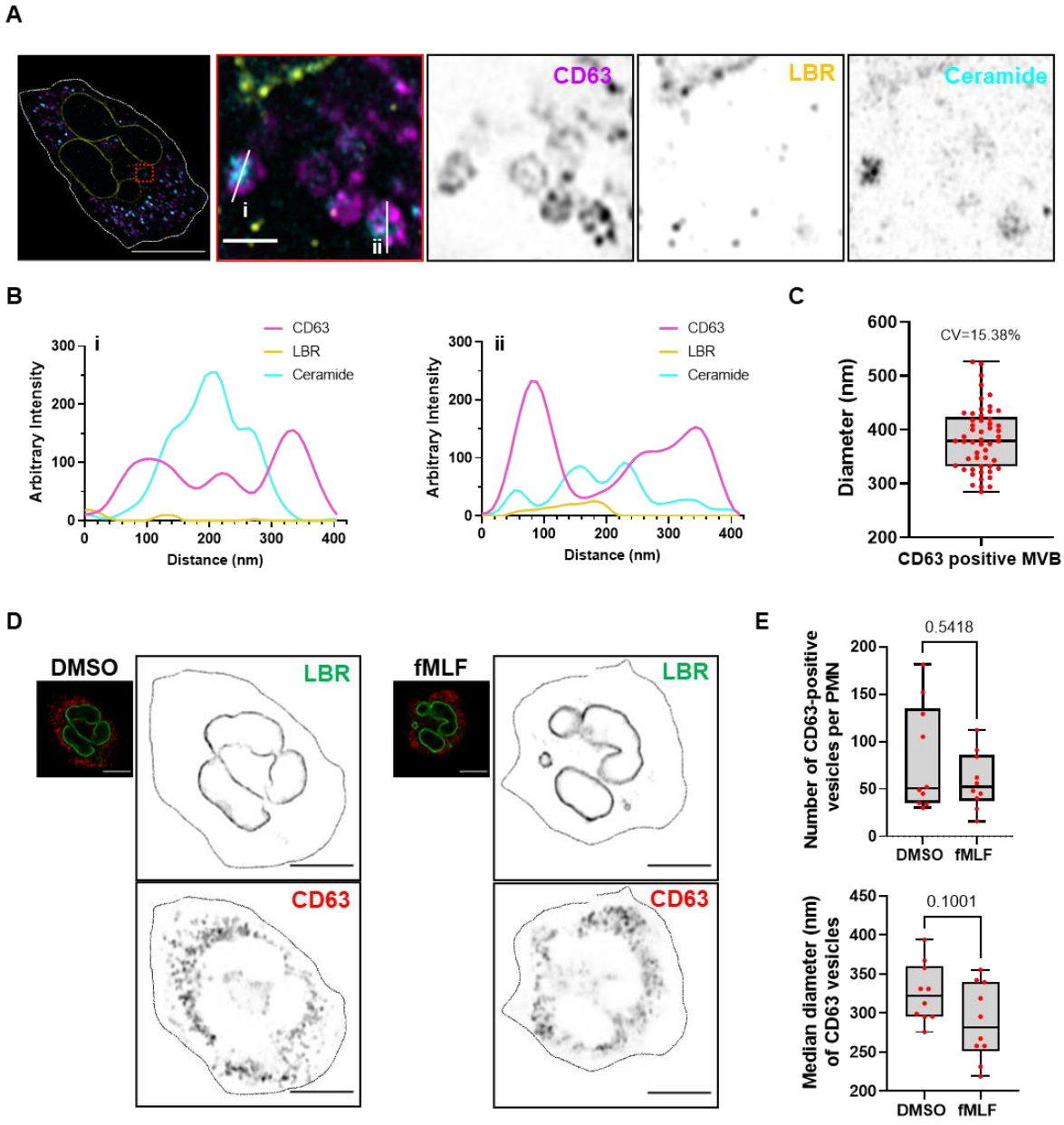
A
CD63
LBR
Ceramide
i
ii
B
CD63
LBR
Ceramide
Arbitrary Intensity
Distance (nm)
C
CV=15.38%
Diameter (nm)
CD63 positive MVB
D
DMSO
fMLF
LBR
CD63
E
0.5418
Number of CD63-positive vesicles per PMN
DMSO
fMLF
0.1001
Median diameter (nm) of CD63 vesicles

Figure 2.10: Characterization of CD63 positive vesicles in activated neutrophils.

A Representative four-fold expansion microscopy image of fixed human PMNs chemotaxing towards 100 nM fMLF, captured using Airyscan microscopy, stained for CD63 (magenta), LBR (yellow) and ceramide (cyan) (n = 3). Scale bar 5 μm. In the inset, the scale bar is 400 nm. **B** Line profiles showing the presence of 50–100 nm ceramide (cyan) positive punctae within the CD63 (magenta) positive MVBs from panel A. **C** Graph showing the distribution of the median diameter of CD63-positive MVBs. Data are plotted as box-whisker plot where whiskers indicate the range, and the boundary of the box closest to 200 nm indicates 25th percentile, while the farthest one indicates 75th percentile and the line within the box represents the median. The red dots represent data of 52 CD63-positive MVBs (red dots) from 8 cells pooled from two independent experiments. **D** Representative Airyscan microscopy images of fixed PMNs uniformly stimulated with 100 nM fMLF for 30 min and stained with LBR (green) and CD63 (red) (n = 3). Enlarged images are depicted in inverted grayscale. Scale bar is 5 μm. **E** Box-whisker plots showing the number (top) and median diameter (bottom) of CD63-positive vesicles per cell, as shown in panel C, where whiskers indicate the range, and the boundary of the box closest to zero or 200 nm indicates 25th percentile, while the farthest one indicates 75th percentile and the line within the box represents the median. P value calculated using two-tailed Mann-Whitney test yield non-significant values (n = 3). Source numerical data are available in the source data file.

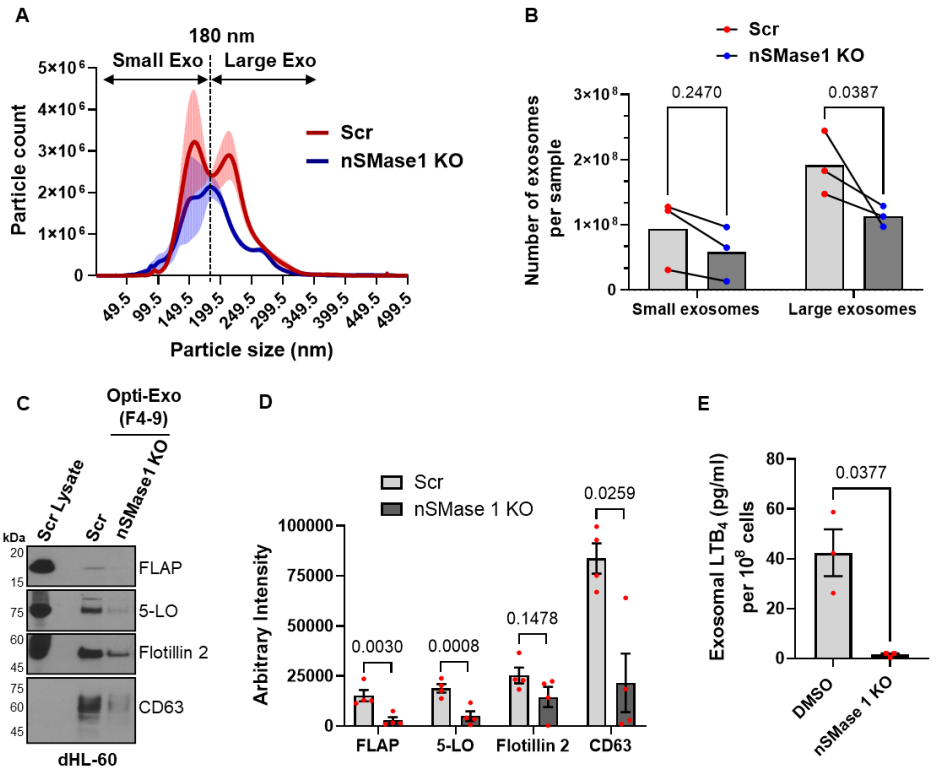

Figure 2.11: Characterization of exosomes isolated from activated Scr and nSMase1 KO dHL-60 cells.

A Histogram showing the particle count and size of exosomes purified from either Scr or nSMase1 KO dHL60 cells stimulated with 100 nM fMLF for 15 min. Data were obtained from nanoparticle tracking analysis (NTA) of the isolated exosomes and is plotted from three independent experiments as mean ± SEM. The dotted line parallel to the y-axis, at 180 nm, indicate the segregation of two exosome populations, small (0–180 nm) and large (181–360 nm). **B** Quantification of the area under the curve from the NTA data. Data from three independent experiments are presented as paired experiments. P-value was obtained using two-way RM ANOVA. **C** Representative western blot images showing the levels of FLAP, 5-LO, Flotillin 2, and CD63 in pooled fractions 4–9 of density-gradient purified exosomes isolated from either Scr or nSMase1 KO dHL-60 cells stimulated with 100 nM fMLF for 15 min. Scr cell lysate represents the amount of protein from 1/100th the number of cells used for exosome isolation (n = 4). **D** Bar graph showing the quantifications of the band intensity of FLAP, 5-LO, Flotillin 2, and CD63 in Scr and nSMase1 KO exosomes. Four data points are plotted as mean ± SEM where each red dot represents the value from one experiment. P values determined using two-tailed paired multiple t-test are reported. **E** Bar graph showing exosomal LTB4 levels from the Scr or nSMase1 KO dHL60 cells stimulated with 100 nM fMLF for 15 min. Data from three independent experiments are plotted as mean ± SEM. P value was obtained using two-tailed ratio paired t-test. Source numerical data and unprocessed blots are available in the source data file.

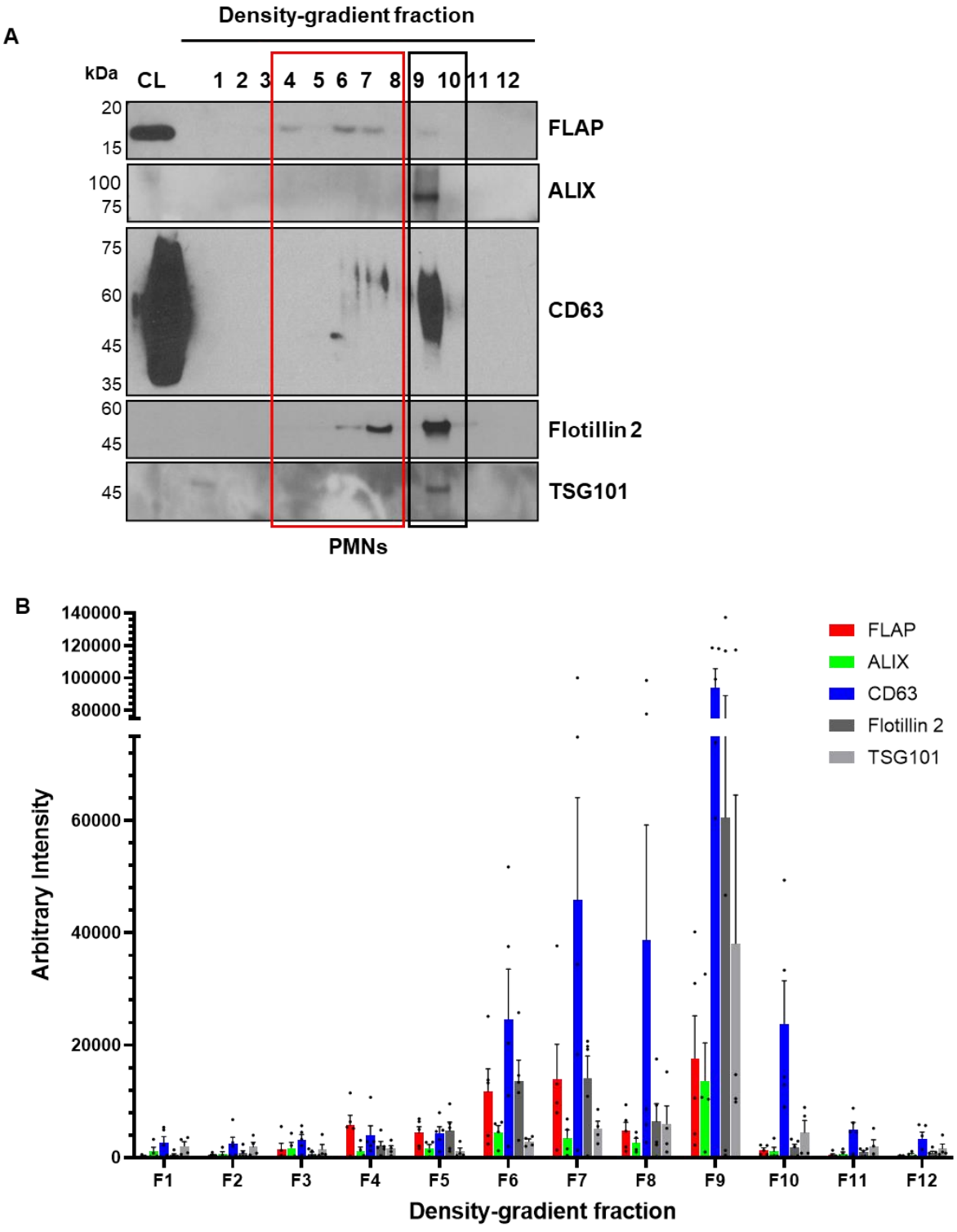
A
Density-gradient fraction
kDa
CL
1 2 3 4 5 6 7 8 9 10 11 12
20
15
FLAP
100
75
ALIX
75
60
45
35
CD63
60
45
Flotillin 2
45
TSG101
PMNs
B
140000
120000
100000
80000
60000
40000
20000
0
Arbitrary Intensity
FLAP
ALIX
CD63
Flotillin 2
TSG101
F1
F2
F3
F4
F5
F6
F7
F8
F9
F10
F11
F12
Density-gradient fraction

Figure 2.12: Characterization of exosomes isolated form activated PMNs.

A Representative western blot showing the distribution of FLAP, CD63, Flotillin 2, TSG101, and ALIX in various fractions of density-gradient purified exosomes isolated from the supernatant of PMNs stimulated with 100nM fMLF for 15 min (n = 4–5). **B** Bar graph showing the arbitrary band intensity of the indicated proteins. Data are plotted as mean ± SEM of at least three independent experiments. Source numerical data and unprocessed blots are available in the source data file.

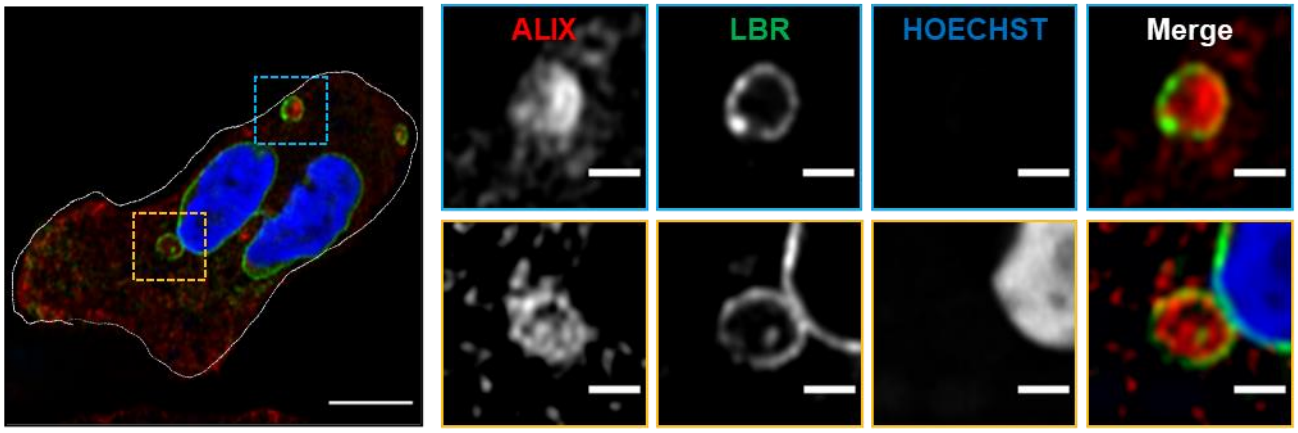

Figure 2.13: ALIX and LBR distribution in activated PMNs.

Representative Airyscan microscopy images of fixed PMNs chemotaxing towards 100nM fMLF and stained for LBR (green) and ALIX (red) (n = 3). Scale bar is 5 µm. In the inset, the scale bar is 1 µm. NE buds are shown in yellow boxes and cytosolic vesicles are shown in blue boxes.

Chapter 3 Cytosolic Phospholipase $A_2\alpha$ ($cPLA_2\alpha$) Regulates Neutrophil Chemotaxis in a Chemoattractant Dependent Manner

3.1 Introduction

Neutrophils are the most abundant immune cells in human blood and are the first responders to sites of inflammation/injury (Kolaczkowska and Kubes 2013, Shah, Burg et al. 2017). They play a crucial role in mediating and resolving inflammation. Long-term inflammation in the vasculature is often the root cause of cardiovascular and cerebrovascular disease pathogenesis like thrombotic strokes and myocardial infarctions (Sun, Wang et al. 2017). In this context, damaged tissues release chemical cues that recruit nearby neutrophils (Majumdar, Sixt et al. 2014, Subramanian, Majumdar et al. 2017). These cues, including formylated peptides [formyl-Methionine-Leucyl-Phenylalanine (fMLF)] or complement 5a (C5a), are referred to as primary chemoattractants (Majumdar, Sixt et al. 2014, Subramanian, Majumdar et al. 2017). Upon chemoattractant stimulation, neutrophils secrete the secondary chemoattractant leukotriene B_4 (LTB_4), which has been shown to dramatically amplify the range of the initial inflammatory signals and contribute to the robust recruitment of neutrophils (Afonso, Janka-Junttila et al. 2012, Lammermann, Afonso et al. 2013). This mechanism of producing a secondary chemoattractant in response to a primary chemoattractant is also known as signal relay. Additionally, it is possible that LTB_4 secreted by tissue resident macrophages acts as a "primary" chemoattractant to help recruit neutrophils to the site of injury or infection (Serezani, Divangahi et al. 2023).

In rat peritoneal macrophages, LTB_4 production is initiated by the binding of formylated peptides to formyl peptide receptor 1 (FPR-1), a G-protein coupled receptor (GPCR), which leads

to the release of calcium and the translocation of cPLA$_2$α to the NE (Peters-Golden and McNish 1993). At the NE, cPLA$_2$α releases AA from membrane phospholipids, which is converted into LTB$_4$ by the sequential action of 5-lipoxygenase (5-LO), 5-LO activating protein (FLAP), and leukotriene A$_4$ hydrolase (LTA$_4$H) (P Needleman, J Truk et al. 1986, Peters-Golden, Song et al. 1996) (Figure 3.1). Additionally, studies from our lab have shown that in neutrophils, LTB$_4$ is packaged in multivesicular bodies (MVBs) (Majumdar, Tavakoli Tameh et al. 2021), which originate from ceramide-rich lipid microdomains at the nuclear envelope (NE) ((Arya, Chen et al. 2022) also see chapter 2), and is secreted outside the cell in exosomes. Our group also demonstrated that defects in the ability to produce, secrete, or detect LTB$_4$ result in greatly attenuated neutrophil responses towards injury or inflammation (Afonso, Janka-Junttila et al. 2012, Lammermann, Afonso et al. 2013, Subramanian, Majumdar et al. 2017).

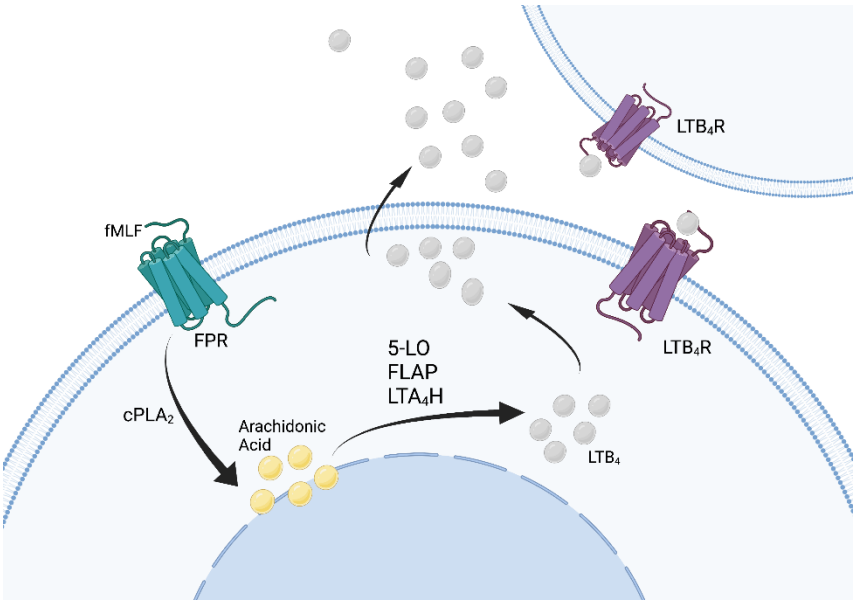

Figure 3.1: Current understanding of LTB$_4$ synthesis and secretion. (See text for details)

It is well established that AA released by cPLA$_2$α is the rate-limiting step in LTB$_4$ production, and disruption in cPLA$_2$α activity leads to a decrease in LTB$_4$ production (Leslie 2004, Dennis, Cao et al. 2011, Leslie 2015, Yonker, Pazos et al. 2017). However, few studies have evaluated the effect of cPLA$_2$α on neutrophil migration and chemotaxis. Using a cPLA$_2$α pharmacological inhibitor (cPLA$_2$i), Yonker and colleagues reported that cPLA$_2$α inhibition in neutrophils leads to a significant decrease in LTB$_4$ production and neutrophil migration towards *Pseudomonas aeruginosa* infected pulmonary epithelial cells (Yonker, Pazos et al. 2017). However, in inflammatory responses, neutrophils respond to various chemokines and chemoattractants such as interleukin 8 (IL8), C5a, and formulated peptides. In this chapter, I investigated the role of cPLA$_2$α during neutrophil chemotaxis towards various chemoattractants using a controlled *in vitro* setting.

3.2 Materials and Methods

3.2.1 Isolation of human neutrophils

Blood was donated by healthy males and females who had not taken aspirin for seven days and NSAIDs for 48 hours. Blood was collected by venipuncture from the Platelet Pharmacology and Physiology Core at the University of Michigan. Neutrophils were purified using dextran based sedimentation followed by histopaque density gradient centrifugation as described earlier (Subramanian, Moissoglu et al. 2018). Briefly, whole blood was incubated with equal volume of 3% dextran (Sigma D1037) in 0.9% NaCl for 1hr at 37ºC to help sediment erythrocytes. One volume of Histopaque-1077 (Sigma 10771) was underlaid to three volumes of plasma containing monocytes, lymphocytes, and neutrophils and centrifuged at 400g for 20min without break to separate neutrophils from PBMCs. Residual RBCs were lysed using ACK lysis buffer (Gibco A10492-01 100mL). Isolated neutrophils were resuspended in mHBSS (150mM NaCl, 4mM KCl,

1.2mM $MgCl_2$, 10mg/mL glucose, and 20mM HEPES pH 7.2). This protocol yields >95% neutrophils.

3.2.2 Cell lines and plasmid constructs

The human myeloid leukemia-derived pro-myelocytic cell line HL-60 was obtained from ATCC (CCL-240) and maintained in RPMI-1640 medium containing 10% HI-FBS, 20 mM HEPES pH 7.2 and penicillin–streptomycin antibiotic cocktail. To generate neutrophil-like cells, HL-60 cells were differentiated in culture medium containing 1.3% DMSO for 5.5 days with a change to fresh medium every other day as described by Saunders et al. (Saunders, Majumdar et al. 2019).

HEK293T cells obtained from ATCC (CRL-3216), cultured in DMEM containing 10% FBS were used to generate lentiviral particles for the generation of stable HL-60 cell lines. pVSVG, psPax2, and pLentiCRISPR V2 vector expressing scramble (SCR) or $cPLA_2\alpha$ single guide RNA (sgRNA) were transfected to HEK293T at a ratio of 1:2:4 using Lipofectamine 3000 transfection reagent. The lentiviral particles collected after 24-, 48- and 72-hours post-transfection were pooled, concentrated using PEG-it (Systems Biosciences LV810A-1), and added to the HL-60 cells with 8μg/mL polybrene. The clones expressing the construct were selected in 2μg/mL puromycin and verified by western blotting and genetic sequencing. The $cPLA_2\alpha$ sgRNA, ACACCACTACCGTAAACTTG and SCR sgRNA, GCGGTCTAGGCGCAAGAGGT, were cloned in pLentiCRISPR V2 plasmid, which was a kind gift from the Feng Zhang lab.

3.2.3 Under-agarose chemotaxis assay

The under agarose chemotaxis assay was performed as described by Saunders *et al.* (Saunders, Majumdar et al. 2019). Briefly, 35mm glass bottom dish with 20mm micro-well #1.5

glass coverslip (MatTek Corp P35G-1.5-10-C.S) was coated with 1% BSA for 1hr at 37˚C. 0.5% SeaKem ME agarose (Lonza, 50010) was prepared in 50% DPBS and 50% mHBSS (20mM HEPES pH 7.4, 150mM NaCl, 4mK KCl, 1.2mM $MgCl_2$ and 10mg/mL glucose). The agarose was allowed to solidify in the coated dishes. Three 1mm diameter wells were carved at 2mm distance from each other. For human neutrophils migration assays, neutrophils were resuspended in mHBSS and pretreated with either DMSO (Sigma Aldrich, D2650-100mL), 200nM MK886 (Cayman Chemical, 10133) or 0.1μM–10μM of Pyrrophenone (cPLA2ai, Calbiochem, 530538) along with 0.5μM CellTracker Red CMPTX dye (Invitrogen, C34552) for 15min at 37˚C while rotating. For HL-60 cell lines, differentiated HL-60 cells were resuspended in mHBSS and stained with 0.5μM CellTracker Red CMPTX dye for 15min at 37˚C while rotating. 100nM fMLF diluted in mHBSS was added to the middle well and 50,000 stained cells in 7μL were added to the flanking wells. Time-lapse videos were acquired at 30sec intervals for 2hrs using a 10X objective of a fluorescent microscope equipped with an environment-controlled unit set at 37˚C.

3.2.4 Chemotaxis analysis

Manual tracking plugin in ImageJ software was used to analyze migration data. Randomly selected cells (30-40 per experiment) were manually tracked over the 2-hour time course for each cell line. The resultant tracks were then added to the chemotaxis tool plug-in in ImageJ to get the mean velocity, mean accumulated distance, and chemotaxis index. Chemotaxis index was represented by X-forward migration index (X-FMI), which shows the efficiency of forward migrating cells in the X-direction (parallel to the chemoattractant gradient). Data from three independent experiments were compiled in GraphPad 9.4.1, and two-tailed t-test was used to determine statistical significance.

3.3 Results

To test the impact of cPLA$_2$α on human neutrophil biology, I treated human neutrophils with a cPLA$_2$α specific pharmacological inhibitor, pyrrophenone (cPLA$_2$αi) (Flamand, Picard et al. 2006) and tested their ability to secrete LTB$_4$. MK886, a FLAP inhibitor, was used as a positive control as our lab previously showed a decrease in LTB$_4$ secretion upon treatment with this inhibitor (Majumdar, Tavakoli Tameh et al. 2021). As expected, I observed a significant decrease in LTB$_4$ production by neutrophils treated with either MK886 or cPLA$_2$αi (**Figure 3.2A**). Next, I tested the impact of cPLA$_2$α on human neutrophil migration. DMSO, MK886, and cPLA$_2$αi treated neutrophils were allowed to directionally migrate towards 100nM fMLF. As expected (Afonso, Janka-Junttila et al. 2012), I found that MK886-treated neutrophils exhibited a defect in directional migration towards fMLF, as shown by the wandering tracks of individual cells (**Figure 3.2B&C**). However, we did not see a decrease in the chemotaxis index of these cells (**Figure 3.2G**). Surprisingly, I found that cPLA$_2$αi-treated neutrophils exhibited a dose-dependent increase in directionality and distance migrated towards 100nM fMLF (**Figure 3.2D-I**). Worried that this phenotype is due to the off-target effects of the cPLA$_2$αi (Yun, Lee et al. 2016), in collaboration with Dr. Subhash Arya (a postdoctoral fellow in the Parent lab), I generated cPLA$_2$α$^{-/-}$ HL-60 cells (see chapter 4 for cPLA$_2$α$^{-/-}$ characterization). Scramble (SCR) sgRNA was used to make the corresponding control cell line. To assess the role of cPLA$_2$α in the HL-60 cells, I first compared the ability of differentiated SCR and cPLA$_2$α$^{-/-}$ cells to migrate directionally towards the primary chemoattractant fMLF. Similarly to what I observed in human neutrophils, I found that cPLA$_2$α$^{-/-}$ cells migrate slightly better towards fMLF, as depicted by the significant increase in the X-FMI, which shows the efficiency of forward migrating cells in the X-direction (parallel to the chemoattractant gradient) (**Figure 3.3B**). However, no significant differences were observed in

the average velocity (**Figure 3.3C**) and average accumulated distances (**Figure 3.3D**) between cPLA$_2\alpha^{-/-}$ and SCR HL-60 cells. Together, these results suggests that cPLA$_2\alpha$ restains the directional migration of neutrophils towards fMLF.

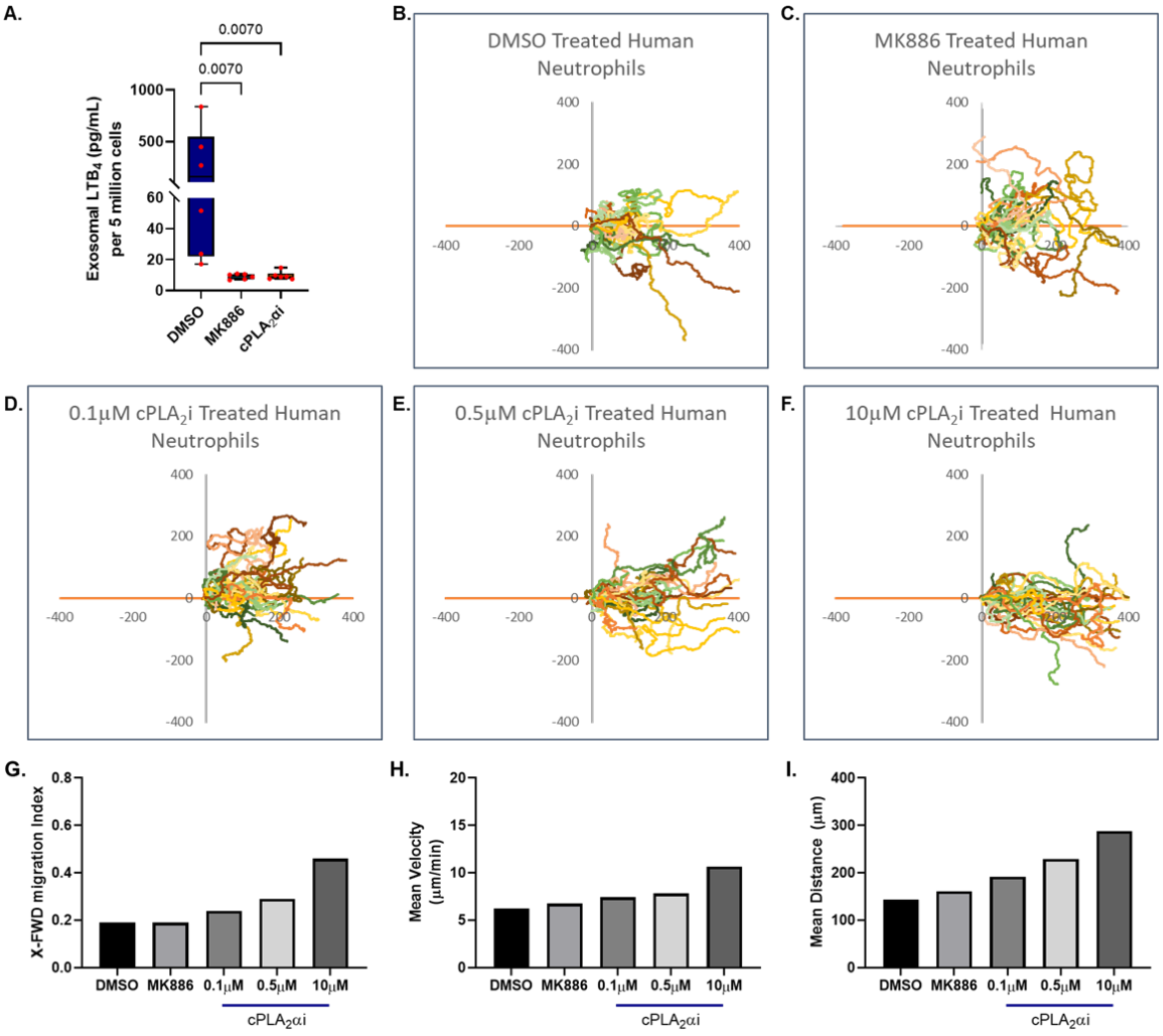

Figure 3.2: cPLA$_2\alpha$i treated neutrophils show a dose-dependent increase in migration towards fMLF.

A) Box and whisker graph showing levels of LTB$_4$ secreted from the neutrophils treated with 0.01% DMSO, 200nM MK886, or 1µM cPLA$_2\alpha$i for 15min followed by stimulation with 100nM fMLF for 15 min. Data from six independent experiments are plotted as min and max with all points. P value was obtained using one-way ANOVA Kruskal-Wallis test. **(B-F)** Plots showing individual cell tracks of neutrophils treated with **(B)** 0.01%DMSO, **(C)** 200nMMK886, **(D)** 0.1µm cPLA$_2\alpha$i, **(E)** 0.5µm cPLA$_2\alpha$i, **(F)** 10µm cPLA$_2\alpha$i migrating towards 100nM fMLF from N=1 experiment. **(G–I)** Graphs depicting X-FMI **(G)**, mean velocity **(H),** and mean accumulated distance **(I)** of cells migrating cells.

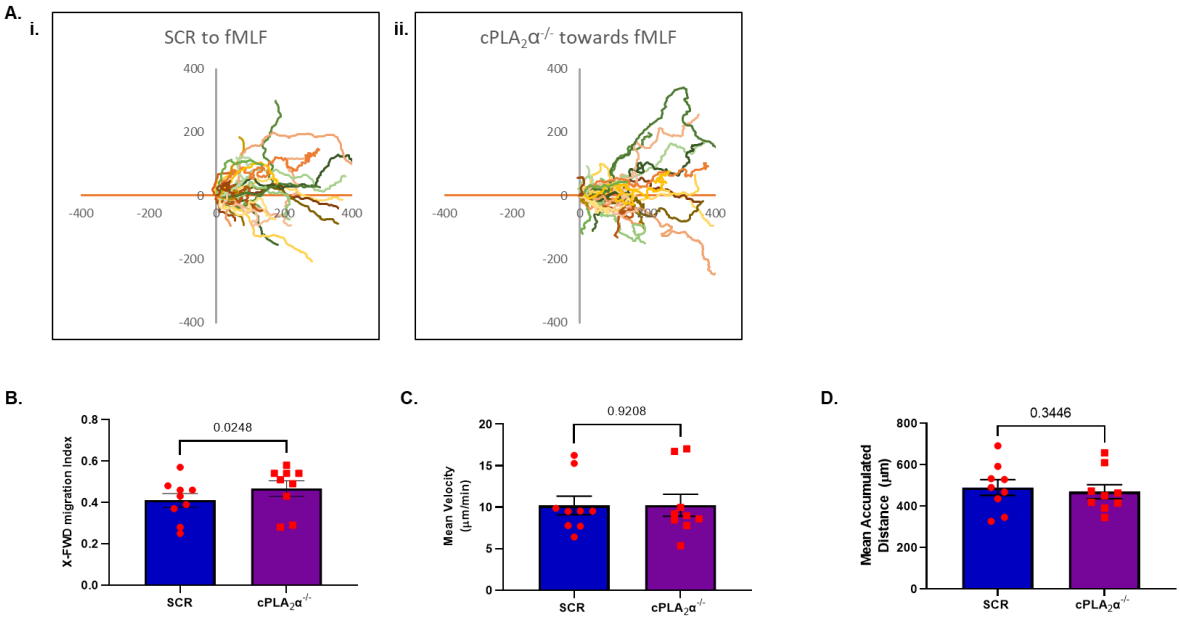

Figure 3.3: cPLA$_2\alpha^{-/-}$ HL-60 cells have no defects in migration towards fMLF

(A) Plots showing representative individual cell tracks of differentiated (i) SCR and (ii) cPLA$_2\alpha^{-/-}$ cells migrating towards 100nM fMLF from N=9 experiments. **(B-D)** Graphs depicting X-FMI **(B)**, mean velocity **(C)**, and mean accumulated distance **(D)** of migrating cells. The error bar represents mean ± SEM and each dot represents the average of a biological replicate. Two-tailed paired t-test was used for statistical analysis.

In the body, neutrophils are exposed and respond to various chemoattractants (Neuber, Hilger et al. 1991, Shah, Burg et al. 2017). Therefore, I next sought to test if cPLA$_2\alpha^{-/-}$ cells exhibit any migration defects towards other chemoattractants. I tested the migration of cPLA$_2\alpha^{-/-}$ HL-60 cells towards (i) C5a, a primary chemoattractant, (ii) LTB$_4$, a secondary chemoattractant, and (iii) IL-8, a chemokine. Looking at the individual cell tracks, I observed that cPLA$_2\alpha^{-/-}$ cells exhibited migratory defects towards C5a, LTB$_4$, and IL-8 (**Figure 3.4B**) when compared with SCR control cells (Figure 3.4A). Quantification revealed a significant decrease in the X-FMI towards all three attractants (Figure 3.5A). Furthermore, I observed a downward trend in the total distance covered by the cPLA$_2\alpha^{-/-}$ cells towards C5a and LTB$_4$ (**Figure 3.5C**). However, I did not observe any significant differences in the average velocity of the cPLA$_2\alpha^{-/-}$ cells migrating toward any of the attractants (**Figure 3.5B**). Together, these results suggest that cPLA$_2\alpha$ amplifies neutrophil migration towards C5a, LTB$_4$, and IL8.

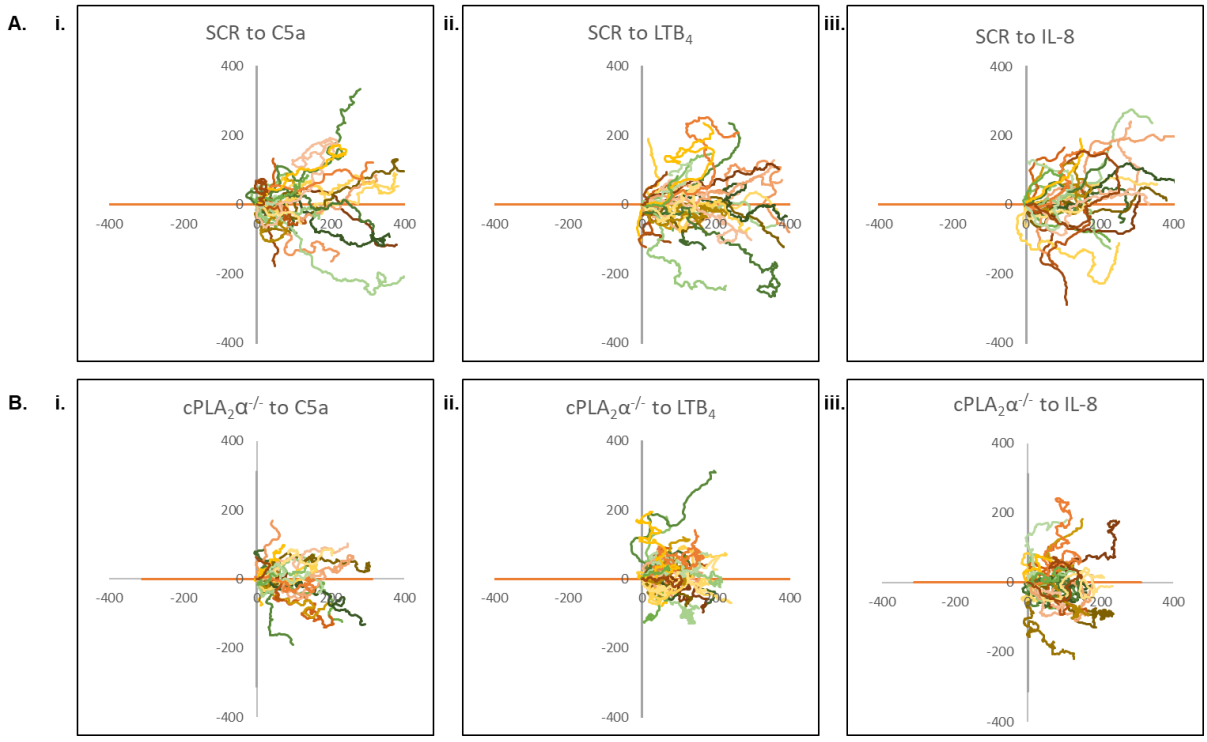

Figure 3.4: $cPLA_2\alpha^{-/-}$ HL-60 cells have defective migration towards C5a, LTB_4 and IL8

(A) Plots showing representative individual cell tracks of differentiated SCR cells migrating towards (i) 1µg/mL C5a, (ii) 100nM LTB_4 from N=3 experiments, and (iii) 100nM IL8 from N=2 experiments. **(B)** Plots showing representative individual cell tracks of differentiated $cPLA_2\alpha^{-/-}$ cells migrating towards (i) 1µg/mL C5a, (ii) 100nM LTB_4, and (iii) 100nM IL8. Each trace represents the migration path of a single cell.

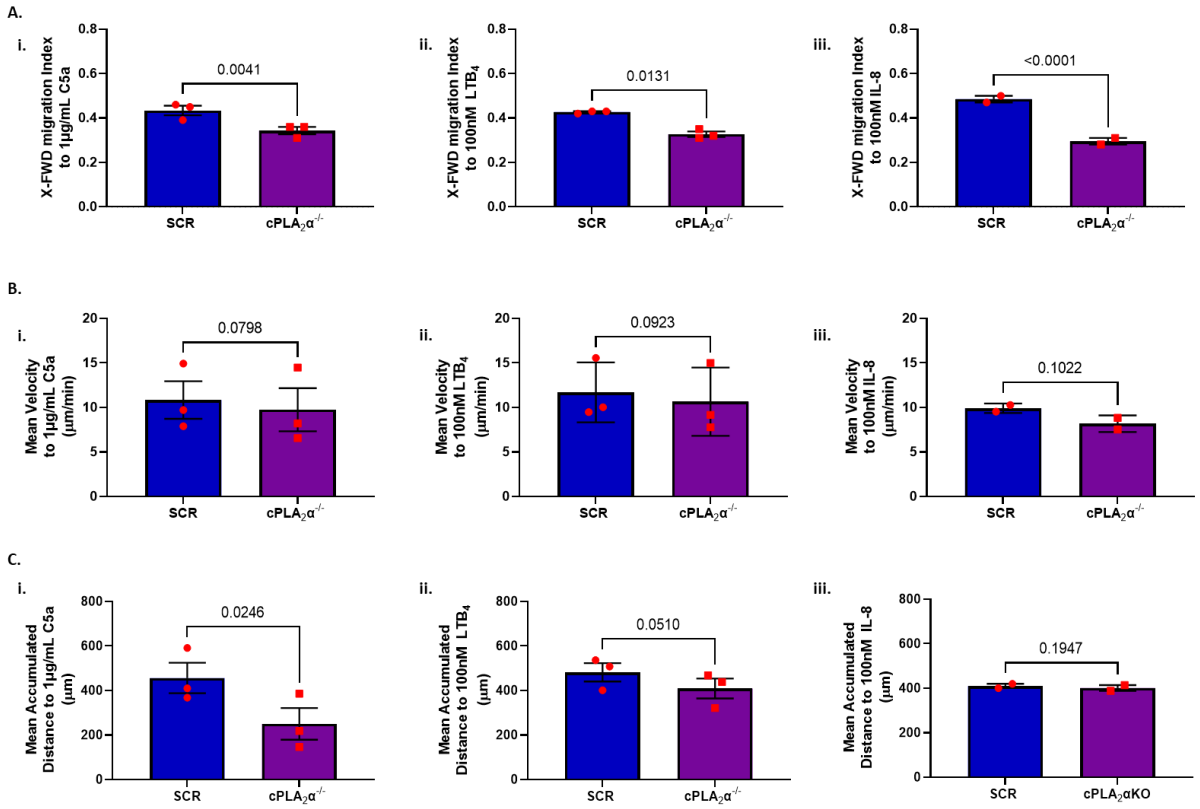

Figure 3.5: cPLA$_2\alpha^{-/-}$ HL-60 cells have a significant decrease in chemotactic index when migrating towards C5a, LTB$_4$, and IL8

(A-C) Graphs depicting X-FMI **(A)**, mean velocity **(B)**, and mean accumulated distance **(C)** of cells migrating towards (i) 1µg/mL C5a, (ii) 100nM LTB$_4$ from N=3 experiments and (iii) 100nM IL8 from N=2 experiments. Each shape and color represent the average of a biological replicate. Two-tailed paired t-test was used for statistical analysis.

3.4 Discussion

In this chapter, I investigated the role of cPLA$_2\alpha$ during neutrophil chemotaxis. I showed that inhibition of cPLA$_2\alpha$ in human neutrophils led to a dose-dependent effect on neutrophil migration towards fMLF: the cells migrated better with increasing concentrations of cPLA$_2\alpha$i (**Figure 3.2Figure 3.2**). Similar results were observed in the migration of cPLA$_2\alpha^{-/-}$ cells, which showed slightly improved migration towards fMLF (**Figure 3.3**). These findings contradict a

previously published report that cPLA$_2$α is required for neutrophil migration towards *P. aeruginosa* infected H292 human pulmonary cells (Yonker, Pazos et al. 2017). This is because fMLF is predicted to be the main chemoattractant involved in *P. aeruginosa* infection. This discrepancy could be explained by the difference in the assay used to measure neutrophil migration. The 3D assay used by Yonker et al. requires neutrophils to first squeeze through the transwell insert pores, followed by squeezing through the epithelial cell monolayer. It was recently established that cPLA$_2$α activity is essential for cells to squeeze through tight spaces (~ 3μm) (Enyedi, Jelcic et al. 2016, Lomakin, Cattin et al. 2020, Venturini, Pezzano et al. 2020). However, cPLA$_2$α seems to be important only for a small range of squeezing diameters as cPLA$_2$α was not activated when neutrophils were compressed into a 5μm space. Based on these findings, it is possible that the decrease in migration of cPLA$_2$i treated neutrophils observed by Yonker and colleagues was due to an inability of the neutrophils to squeeze through the transwell filters with a 3μm pore size. On the other hand, the under agarose chemotaxis assays I performed only call for the ~5μm compression, potentially negating the requirement of cPLA$_2$α to enter the space between the agarose and glass. Therefore, the under agarose assay might be exclusively looking at the involvement of cPLA$_2$α in 2D neutrophil migration.

cPLA$_2$α is essential to produce various pro and anti-inflammatory molecules as AA released by cPLA$_2$α activity leads to the generation of prostaglandins, leukotriene, lipoxins, and thromboxanes (see **Figure 1.4** and **Figure 1.5** in Chapter 1). In this chapter, I discovered that cPLA$_2$α$^{-/-}$ cells exhibit a significant defect in chemotactic index towards C5a, LTB$_4$, and IL-8 (**Figure 3.4, Figure 3.5**). Our lab previously observed a similar neutrophil migration defect toward fMLF when the production of LTB$_4$ is inhibited by MK886 (Afonso, Janka-Junttila et al. 2012, Majumdar, Tavakoli Tameh et al. 2021). An earlier study by Neuber et al. shows that C5a and IL8

stimulation enhances LTB_4 secretion (Neuber, Hilger et al. 1991). Additionally, data from our lab show that neutrophils stimulated with LTB_4 secrete more LTB_4 (data not published). It is possible that C5a, IL-8, and LTB_4 don't establish a strong chemoattractant gradient and the migration towards these attractants is dependent on the generation of LTB_4. Therefore, I hypothesize that it is the lack of $cPLA_2\alpha^{-/-}$ HL-60 cells' ability to produce LTB_4 in response to these chemoattractant stimuli that is resulting in an attenuated migratory response. The reason why we don't observe similar defects in migration towards fMLF is potentially due to the fact that fMLF is an incredibly potent chemoattractant which quickly establishes the gradient. Therefore, in the under agarose assay, the migration towards fMLF is not as dependent on neutrophil signal relay, instead is a measure of migration towards a primary chemoattractant.

In conclusion, in this chapter, I have demonstrated that $cPLA_2\alpha$ regulates neutrophil migration in a chemoattractant-dependent manner. $cPLA_2\alpha$ has been implicated in protein trafficking, inducing membrane curvature, and maintaining lipid homeostasis (Choukroun, Marshansky et al. 2000, Frazier, Wisner et al. 2002, Brown, Chambers et al. 2003, Cho and Stahelin 2005, Schmidt and Brown 2009, Dennis, Cao et al. 2011, Ha, Clarke et al. 2012). Further studies are needed to elucidate the mechanisms by which $cPLA_2\alpha$ impacts neutrophil signal relay and to identify other roles of $cPLA_2\alpha$ in neutrophil biology (See chapter 5, subsection 5.2.1).

Chapter 4 cPLA$_2\alpha$ is Essential for LTB$_4$ Synthesis and Regulates Nuclear Morphology in Chemotaxing *Neutrophil-Like* Cells

4.1 Introduction

Inflammation is the body's normal response to contain an infection and initiate resolution. However, in chronic inflammation conditions, like atherosclerosis and asthma, the body's normal inflammatory response often exacerbates the pre-existing condition (Fanning and Boyce 2013). Eicosanoids, such as leukotriene B$_4$ (LTB$_4$), are primary mediators of inflammation and play a key role in multiple pathological diseases (Dennis and Norris 2015). Enzymes that regulate eicosanoid synthesis have been used as therapeutic targets to generate therapeutic medications for many years. However, a better understanding of the mechanisms behind eicosanoid production and function is needed to lead to better and more focused therapeutics.

Eicosanoids are the product of oxygenation of arachidonic acid (AA), which is released from phospholipids through the action of cytosolic phospholipase A$_2$ (cPLA$_2$). cPLA$_2$ belongs to a superfamily of enzymes that catalyze the hydrolysis of membrane phospholipids. There are six isoforms of this enzyme: cPLA$_2\alpha$, cPLA$_2\beta$, cPLA$_2\gamma$, cPLA$_2\delta$, cPLA$_2\varepsilon$, and cPLA$_2\zeta$ (Dennis, Cao et al. 2011). These isoforms share only 30% sequence homology and are distinctly distributed in tissues, except cPLA$_2\alpha$, which is expressed in all cell tissues (also see Chapter 1) (Dennis, Cao et al. 2011, Leslie 2015). Of these isoforms, cPLA$_2\alpha$ is most abundantly studied as it is ubiquitously expressed (Dennis, Cao et al. 2011, Leslie 2015). cPLA$_2\alpha$ activity is dependent on fluctuations in intracellular calcium levels and is regulated by phosphorylation through the MAPK pathway (Burke and Dennis 2009, Dennis, Cao et al. 2011). One of the major functions of cPLA$_2\alpha$ is the

release of AA from the *sn-2* position of phospholipids in cellular membranes (Dennis, Cao et al. 2011). Additionally, this multifaceted protein has been implicated in various other cellular functions including vesicular trafficking (Brown, Chambers et al. 2003, Ha, Clarke et al. 2012), regulation of membrane curvature (Cho and Stahelin 2005, Lamour, Stahelin et al. 2007, Stahelin, Subramanian et al. 2007, Ward, Ropa et al. 2012, Ward, Bhardwaj et al. 2013, Ward, Sengupta et al. 2020) and cellular mechanotransduction (Lomakin, Cattin et al. 2020, Venturini, Pezzano et al. 2020, Alraies, Rivera et al. 2022).

AA is converted into either leukotrienes, prostaglandins, or lipoxins (P Needleman, J Truk et al. 1986, Hanna and Hafez 2018). In the context of chronic inflammation such as atherosclerosis and asthma, leukotriene B_4 (LTB_4) has been implicated in increasing the severity of the disease (Subbarao, Jala et al. 2004, Higham, Cadden et al. 2016). LTB_4 generation is a highly regulated process, and disruptions in its production, secretion, or detection have been shown to result in greatly attenuated immune responses (Afonso, Janka-Junttila et al. 2012, Kolaczkowska and Kubes 2013, Lammermann, Afonso et al. 2013, Subramanian, Majumdar et al. 2017, Tallima and El Ridi 2018, MacKnight, Stephenson et al. 2019). LTB_4 production is initiated by the binding of chemoattractants to their cognate G–protein-coupled receptor, which leads to increases in intracellular calcium levels, activating $cPLA_2\alpha$ (Alonso, Henson et al. 1986, Kramer, Checani et al. 1986, Leslie, Voelker et al. 1988, Channon and Leslie 1990). In rat peritoneal macrophages, $cPLA_2\alpha$, along with 5-lipoxygenase (5-LO), were shown to translocate from the cytosol to the nuclear envelope (NE) to release AA (Peters-Golden and McNish 1993, Peters-Golden, Song et al. 1996, Peters-Golden 1998, Peters-Golden 1998). AA is then converted to LTB_4 by the sequential action of 5-LO, 5-LO activating protein (FLAP), and leukotriene A_4 hydrolase (LTA_4H). LTB_4 is a hydrophobic molecule that traffics through the hydrophilic, cytosolic

environment before it is secreted from cells. Our group has shown that in neutrophils, LTB_4 is packaged within multivesicular bodies (MVBs) that originate at the NE (Majumdar, Tavakoli Tameh et al. 2021). These MVBs originate at specific ceramide-rich lipid-ordered microdomains on the NE and are functionally distinct from the CD63-positive canonical MVBs ((Arya, Chen et al. 2022) also see chapter 2) (**Figure 4.1**). These studies provide a mechanism by which secreted LTB_4 is protected from harsh extracellular environments, thereby allowing for the communication of directional cues to distant cells during inflammatory responses.

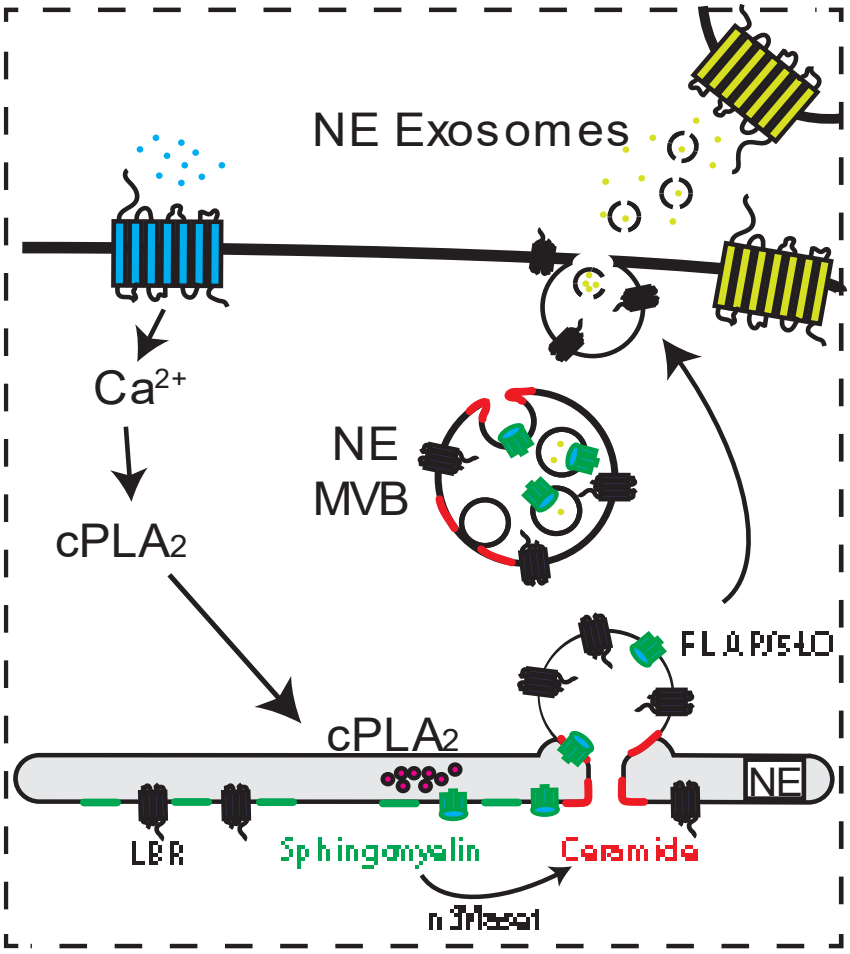

Figure 4.1: Cartoon depicting our current understanding of the mechanisms underlying LTB_4 synthesis in chemotaxing neutrophils (from Subhash Arya; see text for details).

cPLA$_2$α is also involved in maintaining lipid homeostasis and inducing membrane curvature. Cellular membranes are essential structures as they compartmentalize individual intracellular organelles. These highly dynamic membranes function as a barrier and rapidly and precisely change their shape in response to various stimuli (Has, Sivadas et al. 2022). Membrane curvature can be induced through: (i) protein-membrane interactions, (ii) lipid shape changes, and (iii) molecular crowding (Has, Sivadas et al. 2022, Peeters, Piët et al. 2022). cPLA$_2$α induces membrane curvature through its lipase activity and protein-membrane interactions. Structurally, cPLA$_2$α contains a C-terminal C2 domain that contains calcium binding sites and an N-terminal α/β hydrolase domain containing the serine/aspartate catalytic dyad (Dessen, Tang et al. 1999). cPLA$_2$α-mediated hydrolysis of neutral phospholipids, for example phosphatidylcholine (PC), results in the release of AA and the generation of lysophosphatidylcholine (inverted-cone shaped lipid). The increase in the local concentration of inverted-cone shaped lysophospholipid on the membrane creates positive membrane curvature (Brown, Chambers et al. 2003, Ha, Clarke et al. 2012). In addition, upon binding with Ca^{2+}, the C2 domain of cPLA$_2$α penetrates neutral phospholipids to a depth of 1-1.5nm, assisting in the induction of membrane curvature (Frazier, Wisner et al. 2002). Ward and colleagues further validated this by using various mutants of cPLA$_2$α lacking the ability to penetrate or bend membranes (Ward, Ropa et al. 2012). Additionally, it was shown that the C2 domain of cPLA$_2$α alone is sufficient for inducing membrane curvature in both a cell-free system and intact A549 cells (Ward, Sengupta et al. 2020). Interestingly, it was also reported that the C2 domain of cPLA$_2$α preferentially translocates to smaller vesicles (~50nm) with high positive curvature versus larger vesicles (~600nm) (Ward, Sengupta et al. 2020). Together, these findings suggest that cPLA$_2$α induces membrane curvature and that the C2 domain of cPLA$_2$α senses the curvature on membranes and preferentially binds these curved regions

(Ward, Sengupta et al. 2020). This feature of cPLA$_2$α activity might be especially important in the context of LTB$_4$ production, as this process requires the generation of extensive membrane curvature and lipid remodeling.

Recent studies have also implicated cPLA$_2$α in cellular mechanotransduction (Enyedi, Jelcic et al. 2016, Lomakin, Cattin et al. 2020, Venturini, Pezzano et al. 2020, Alraies, Rivera et al. 2022). The nucleus is the largest organelle in the cell and has been shown to be involved in regulating the ability of cells to sense their surrounding environment (Guilluy, Osborne et al. 2014, Kirby and Lammerding 2018, Ross and Stroud 2021). Enyedi and colleagues demonstrated that cPLA$_2$α translocates to the NE upon nuclear swelling and showed that cPLA$_2$α translocation increases upon deletion of Lamin A/C (Enyedi, Jelcic et al. 2016). These results indicate that cPLA$_2$α translocation is dependent on increased nuclear tension. Corroborating these results, Lomakin and colleagues showed that under confined conditions, immature dendritic cells switch to a more migratory phenotype in a cPLA$_2$α-dependent manner by increasing cortical myosin II to allow cells to escape the confined environment. Interestingly, this behavior is specifically observed under extreme compression of 3μm and not at 5μm compression (Lomakin, Cattin et al. 2020). Venturini and colleagues showed similar results in zebrafish progenitor cells (Venturini, Pezzano et al. 2020). Together, these results demonstrate the requirement of cPLA$_2$α in nuclear mechanosensing under confinement.

In the event of an infection or injury, neutrophils are the first cells that respond (Shah, Burg et al. 2017). The patrolling neutrophils sense and directionally migrate toward the damage and pathogen associated molecular patterns (DAMPs/PAMPs) released at the site of infection or injury. Neutrophils must first squeeze through the endothelial cells lining of blood vessels and navigate through the connective tissue (Shah, Burg et al. 2017). While migrating, neutrophils produce and

secrete LTB_4 that dramatically amplifies the signal from the initial site and robustly recruits distant neutrophils to initiate resolution (Lammermann, Afonso et al. 2013). In neutrophils, $cPLA_2\alpha$-mediated AA release is primarily converted to leukotrienes (Peters-Golden 1998). However, aside from its role in LTB_4 production, little is known about the function of $cPLA_2\alpha$ in neutrophils. With recent studies implicating $cPLA_2\alpha$ in cellular mechanotransduction in HeLa-Kyoto cells (a variant of HeLa cells (Tang 2019)) and zebrafish (Lomakin, Cattin et al. 2020, Venturini, Pezzano et al. 2020), $cPLA_2\alpha$ may also regulate neutrophil mechanotransduction. Additionally, Yonker and colleagues demonstrated that inhibition of $cPLA_2\alpha$ in human neutrophils leads to decreased LTB_4 production and neutrophil transepithelial migration towards infected cells (Yonker, Pazos et al. 2017). However, to what extent is $cPLA_2\alpha$ involved in neutrophil migration remains to be addressed. I hypothesize that in neutrophils, $cPLA_2\alpha$ is involved in LTB_4 generation and is also required to maintain membrane architecture for optimal chemotaxis.

4.2 Materials and Methods

4.2.1 Cell Lines

The human myeloid leukemia-derived pro-myelocytic cell line HL-60 was obtained from ATCC (CCL-240) and maintained in RPMI-1640 (Gibco, 11875-093) medium containing 10% HI-FBS, 20 mM HEPES pH 7.2 and 1% penicillin–streptomycin antibiotic cocktail (ThermoFisher Scientific #15-140-122). To generate neutrophil-like cells, HL-60 cells were differentiated in culture medium containing 1.3% DMSO for 5 to 6 days with a change to fresh medium every other day, as described by Saunders et al. (Saunders, Majumdar et al. 2019). HEK293T cells obtained from ATCC (CRL-3216) cultured in DMEM containing 10% FBS were used to generate lentiviral particles for the generation of stable HL-60 cell lines. pVSVG, psPax2 and pLentiCRISPR V2 vector expressing SCR/$cPLA_2\alpha$ single guide RNA (sgRNA) or pCDH MSCV MCS EF1 neomycin

vector expressing eGFP fused with cPLA$_2$α (pCDH-Neo-GFP- cPLA$_2$α) at the N-terminal were transfected to HEK293T at a ratio of 1:2:4 using Lipofectamine 3000 transfection reagent. The lentiviral particles collected after 24-, 48- and 72 hours post-transfection were pooled, concentrated using PEG-it (Systems Biosciences LV810A-1), and added to the HL-60 cells with 8 μg/mL hexadimethrine bromide (polybrene) (Sigma Aldrich, H9268-5G). The clones expressing the construct were selected in 2μg/mL puromycin or 1mg/mL G418 and verified by western blotting and genetic sequencing.

4.2.2 Plasmid constructs

The cPLA$_2$α sgRNA; ACACCACTACCGTAAACTTG, was cloned in pLentiCRISPR V2 plasmid, a kind gift from the Zhang lab. pCDH-puro-GFP-cPLA$_2$α construct was made using the NEB Gibson assembly kit (NEB E5510). cPLA$_2$α was amplified from GenScript plasmid pCDNA3.1-cPLA$_2$ (Clone ID Ohu19957) using 5'-ctgtacaagATGTCATTTATAGATCCTTACCAG-3' and 5'-ccctcagcggccgcggatccTGCTTTGGGTTTACTTAGAAAC-3' and GFP was amplified from FPR1-eGFP plasmid from Subramanian et al. (Subramanian, Moissoglu et al. 2018) using 5'-gagctagagctagcgaattcGCCACCATGGTGAGCAAG-3' and 5'-taaatgacatCTTGTACAGCTCGTCCATGC-3' primers. The construct was confirmed by Sanger sequencing.

pCDH-NEO-GFP-cPLA$_2$α construct was made by amplifying GFP- cPLA$_2$α from pCDH-puro-GFP-cPLA$_2$α construct using 5'-gcgggcGCTAGCATGGTGAGCAAGGGCGAGG-3' and 5'-gcgcggcGCGGCCGCctaTGCTTTGGGTTTACTTAG-3' primers and cloning in NheI and NotI sites in pCDH MSCV MCS EF1 neomycin vector. The construct was confirmed by Sanger sequencing

4.2.3 Isolation of human neutrophils

Blood was donated by healthy males and females who had not taken aspirin for seven days and NSAIDs for 48 hours. Blood was collected by venipuncture from the Platelet Pharmacology and Physiology Core at the University of Michigan. Neutrophils were purified using dextran based sedimentation followed by histopaque density gradient centrifugation as described earlier (Subramanian, Moissoglu et al. 2018). Briefly, whole blood was incubated with equal volume of 3% dextran (Sigma D1037) in 0.9% NaCl for 1hr at 37ºC to help sediment erythrocytes. One volume of Histopaque-1077 (Sigma 10771) was underlaid to three volumes of plasma containing monocytes, lymphocytes, and neutrophils and centrifuged at 400g for 20min without break to separate neutrophils from PBMCs. Residual RBCs were lysed using ACK lysis buffer (Gibco A10492-01 100mL). Isolated neutrophils are resuspended in mHBSS (150mM NaCl, 4mM KCl, 1.2mM $MgCl_2$, 1mg/mL glucose, and 20mM HEPES pH 7.2). This protocol yields >95% neutrophils.

4.2.4 Under Agarose chemotaxis assay and chemotaxis analysis

Chemotaxis assay was performed as described by Saunders et al. (Saunders, Majumdar et al. 2019). Briefly, 0.5% SeaKem ME agarose (Lonza 50010) in 50% DPBS (Gibco 14190-144) and 50% RPMI1640 Phenol Red free (Gibco 11835-030) with 20mM HEPES pH7.2 and allowed to solidify in an 8-well chamber slide (Cellvis C8-1.5H-N) coated with 1% BSA (Sigma A7979-50mL) diluted in DPBS. Two 1mm diameter wells were carved at 2mm distance from each other. Differentiated HL-60 cells were resuspended in Phenol Red free RPMI1640 media containing 20mM HEPES pH 7.2 and stained with 0.1μM Hoechst 33342 dye (Invitrogen H21492) for 15 min at 37ºC while rotating at 10 RPM. 100nM fMLF diluted in Phenol Red free RPMI1640 media containing 20mM HEPES pH 7.2 was added to right well, and 50,000 stained cells in 7μL were

added to the left well. Time-lapse images were acquired at 30-sec intervals for 2 hours using a 10X objective of a fluorescent microscope equipped with an environment-controlled unit set at 37˚C.

TrackMate (version 7.7.2) was used to track cells in the Hoechst channel in an unbiased way. Spot statistics were downloaded from TrackMate analysis and uploaded in the chemotaxis analysis code LEH wrote in Matlab R2021a. Tracks with less than 100μm final distance in X direction were excluded from final analysis. Averages of each experiment were plotted using GraphPad Prism (version 9.4.1). Rose plots in Figure 9C were generated using Matlab plug in.

4.2.5 Immunofluorescence Staining in Intact cells.

Differentiated HL-60 cells were allowed to migrate under agarose towards 100nM fMLF for 2 hours and fixed with 4% paraformaldehyde (PFA) (Electron Microscopy Sciences, 15174) diluted in RPMI 1640 Phenol Red Free with 20mM HEPES pH 7.2 at 37˚C for 15 min. Agarose was scooped out using the flat end of the spatula, and cells were fixed again in 4% PFA for 5 min at room temperature. Cells were washed thrice using DPBS and permeabilized with 0.1% Triton X-100 (Sigma T9285-400mL) for 5 min. Cells were stained with following primary antibodies diluted in 2% goat serum (Sigma G9023-10ML) in DPBS overnight at 4º C: Mouse anti-Ceramide (1:100, Sigma C8104-50TST), Rabbit anti-GFP (1:2000, ThermoFisher A6455), Rabbit anti-LBR (1:500, Abcam 32535) and Goat anti-FLAP (1:200, Novus NB300-891). Stained cells were washed with DPBS thrice for 5 mins each, followed by incubation with AlexFluor tagged secondary antibodies (1:500) in 2% goat serum in DPBS for 1 hour at room temperature. The cells were washed again with DPBS thrice, overlaid with 200μL *ImmuMount* mounting media (ThermoScientific, 9990402), and stored at 4ºC until imaging.

4.2.6 Isolation of intact nuclei and purification of nuclear membrane microdomains

This protocol is modified from the DRM isolation protocols by Persaud-Sawin et al. and Cascianelli et al. (Cascianelli, Villani et al. 2008, Persaud-Sawin, Lightcap et al. 2009). Briefly, differentiated HL-60 or PMNs were resuspended in RPMI1640 phenol red-free media with 20mM HEPES pH 7.2 at 50 million cells/mL. These cells were treated with 2mM AEBSF hydrochloride (Pefabloc) (Fisher Scientific, AC328110010) for 15 min at 37˚C followed by stimulation with 100nM fMLF for either15 or 30 min at 37˚C while rotating at 10 RPM. Cells were pelleted at 6000*g* for 30 seconds and resuspended in 10mM dimethyl pimelimidate cross-linker (TCL chemicals D4476) in 1x mHBSS for 15 min at 37˚C, washed once in 20mM Tris pH 8.0, and partially lysed twice in ice-cold hypotonic lysis buffer (10mM HEPES pH 7.2, 4mM $MgCl_2$, 25mM NaCl, 1mM DTT, and 0.1% NP-40) at a density of 50 million cells/mL. Supernatants from the first lysis were collected as the cytosolic fraction after centrifugation at 16000*g* for 10 sec (fig 1A). To remove residual ER fragments (microsomes), Golgi, and mitochondria, nuclear pellets were washed twice with ice-cold Barnes solution (85 mM KCl, 85 mM NaCl, 2.5 mM $MgCl_2$, and 5 mM trichloroacetic acid pH 7.2) (Albi, Lazzarini et al. 2003). Supernatant from the first wash was collected as Barnes (ER) fraction (Fig 1A).

For the western blot analysis, all fractions were resuspended in 1X Laemmli SDS buffer with 2mM AEBSF hydrochloride and boiled at 95˚C for 10 min before loading an equal number of cells per well. For immunofluorescent staining, purified nuclei were resuspended in ice-cold nuclei resuspension buffer (10mM HEPES pH 7.2, 4mM $MgCl_2$, 150mM NaCl, 1mM DTT, and 250mM sucrose) at a density of 1 million cells/mL, added to poly L-Lysine (Sigma, P4832) coated #1.5 glass coverslips and centrifuged at 500*g* for 5 min at 4ºC. The isolated nuclei were fixed with 4% PFA diluted in resuspension buffer for 10 min at room temperature, followed by primary antibody staining in 2% goat serum diluted in DPBS overnight. Mouse anti-ceramide (Sigma

C8104-50TST) was used at 1:200 dilution, rabbit anti-GFP (ThermoFisher A6455) was used at 1:1500 dilution, and goat anti-FLAP (Novus NB300-891) was used at 1:200 dilution. Of note, we observed that pH plays an important role in the quality of lysis. We observed poor cell lysis when all the buffers were used at pH 7.4, while pH 7.2 works best for this protocol.

For the isolation of lipid microdomains, nuclei were further lysed in 650µL ice-cold TNE buffer (50mM Tris–Cl pH 7.4, 150mM NaCl, and 5mM EGTA) containing 4 mM $MgCl_2$ and 1% Triton X-100. The suspension was passed through a 23G needle 30X and incubated on ice for 30 min. The supernatant containing the nuclear envelope and nucleoplasm was collected by pelleting the samples at 110g for 10 min at 4ºC. In 13mL ultracentrifuge tubes (Beckman 331372), NE containing supernatants were then adjusted to 40% iodixanol concentration using 60% OptiPrep solution (Sigma D1556), overlayed with 7mL of 30% iodixanol, 2mL of 20% iodixanol, followed by 1mL of 5% iodixanol solution in TNE buffer. Sixteen 750µL fractions from the top were collected after centrifugation at 150,000g for 16 hours at 4ºC. The proteins were concentrated using trichloroacetic acid (TCA)-acetone method and were resuspended in 80µL of 1x XT sample buffer (BioRad, 1610791) under reducing conditions, boiled at 95ºC for 10 min and loaded on Criterion XT 4-12% Bis-Tris gel (BioRad 3450124) for electrophoresis. The proteins were transferred to 0.2µm PVDF membrane, blocked using 1X Fish gelatin (Fisher Scientific NC0382999) in Tris-buffered saline containing 0.1% Tween-20 (Fisher Scientific 337-500), and probed for specific proteins using antibody against FLAP (1 µg/mL, Abcam 85227), flotillin 2 (1:1,000, CST 3436), nSMase1 (1:500, CST 3867) and $cPLA_2\alpha$ (1:1,000, Santa Cruz Biotechnology sc-376618).

4.2.7 Microscopy and Image analysis.

Fixed cells and isolated nuclei were imaged using the Plan Apochromat 63X/1.4 Oil DIC M27 objective on Zeiss LSM 880, AxioObserver equipped with AiryScan Superresolution mode with 3X or 5X digital zoom, respectively, at 185nm step size.

For migrating cells, whole cell (WC) regions of interest (ROIs) were drawn using the polygon selection tool, and nuclei ROIs (NUC) were generated in cellpose software and converted to ROIs in FIJI (2.9.0) image analysis tool. Enlarge tool was used to add 1μm (Fig 1C) or 50nm (Fig 7A) to NUC and capture either perinuclear (PN) or nuclear envelop (NE) intensities, respectively. Using the Z slice where most of the cells are in focus, the area, min. and max. grey values, mean grey value, perimeter, and integrated density measurements were collected from FIJI for WC, NUC, PN, and NE ROIs. For cytosolic measurements, values from either PN or NE ROI were subtracted from respective WC ROI, whereas for perinuclear and nuclear envelop measurements, values from NUC were subtracted from PN or NE ROI, respectively. Integrated densities of each cell from three biological replicates were plotted using GraphPad Prism software. Ordinary one-way ANOVA was performed for statistical significance analysis.

For colocalization analysis, ROIs of isolated nuclei were thresholded using maximum entropy parameters, and Mander's co-localization coefficients were determined using the Coloc2 analysis plugin in FIJI. The values were plotted using GraphPad Prism software. Outliers were calculated using the GraphPad Prism ROUT test (Q=1%) and were excluded from the final statistical analysis using the Man Whitney test.

4.2.8 Exosome isolation, LTB_4 ELISA, trypsin protection assay, and nanotracking analysis

Exosome isolation was performed according to the guidelines described by Thery et al. (Théry, Witwer et al. 2018). Differentiated SCR, *cPLA$_2\alpha^{-/-}$*, and GFP- cPLA$_2\alpha$/ *cPLA$_2\alpha^{-/-}$* cells were stimulated with 100nM fMLF in RPMI-1640 containing 10 Units/ml DNase I (Sigma Aldrich

DN25) for 30 min at 37°C and the supernatants were collected at 500*g* at 4°C for 5 min. The apoptotic bodies were removed at 4,000*g* for 20 min and filtrated through a 0.45μm polyethersulfone membrane filter. The extracellular vesicles in the filtered supernatant were concentrated with 8% PEG-6000 (Bio Basic PB0432) in 20mM HEPES containing 500mM NaCl at 4°C for 36 hours, followed by centrifugation at 4,000*g* at 4°C for 1 hour. The remaining PEG solution was washed by resuspending the pellet in 5mL ice-cold PBS and spinning at 100, 000g for 1 hour in Beckman SW55Ti rotor. The concentrated extracellular vesicle, resuspended in 1mL 250 mM sucrose and 20 mM Tris–Cl pH 7.4, were overlayed on the top of optiprep gradients and centrifuged at 100,000*g* for 16 h at 4°C using Beckman Sw41Ti rotor. The optiprep gradients were prepared in 250 mM sucrose and 20 mM Tris–Cl, starting from the bottom as 3 ml of 40% optiprep, 3 ml of 20% optiprep, 3 ml of 10% optiprep, and 2 ml of 5% optiprep. The fractionated exosomes were collected as 12 fractions of 1mL each from the top (lower to higher density). Exosomes containing fractions 4-9 (Iodixanol density 1.083 -1.142 g/ml) were pooled and diluted to 13 ml with PBS, followed by centrifugation at 100,000g for 1 hour at 4ºC. The purified exosomes were either used to assess exosomal LTB_4 content or to determine the orientation of exosome associated proteins.

LTB_4 ELISA kit (Cayman Chemicals 520111) was used to assess LTB_4 levels in the isolated exosomes homogenized in 100μL ELISA buffer using a 3mm diameter sonicator probe at an amplitude of 20% with 2 sec on/off cycles for a total of ten cycles on ice. To detect LTB_4 concentrations within the linear range, 50μL of concentrated homogenate was diluted 4X in ELISA buffer, and LTB_4 levels were quantified according to the manufacturer's instructions. The values obtained were plotted using GraphPad prism.

To determine orientation of exosome associated proteins, the isolated exosomes were resuspended in HBSS supplemented with 1mM $CaCl_2$, volumetrically divided into two equal fractions, one fraction treated with 50µg/ml trypsin (ThermoFisher Scientific 25200072) for 30 min at 37ºC. The trypsin was inactivated by diluting the exosomes in AEBSF hydrochloride containing HBSS, followed by centrifugation at 120,000g for 1 hour at 4ºC to pellet the exosomes. The pelleted exosomes were lysed in 1X XT sample buffer at 95ºC for 10 min, and equal volumes were loaded on Criterion XT 4-12% Bis-Tris electrophoresis gel for western blotting.

The data for NTA were captured using a Malvern Nanosight NS300 equipped with a 488nm laser and a high sensitivity sCMOS camera and analyzed using the NTA 3.3 Dev Build 3.3.301 software. The exosomes purified using iodixanol-density gradient centrifugation were resuspended in DPBS, vortexed, and diluted to 1:1,000 in 0.22µm filtered particle-free water to obtain a recommended concentration range of 1–10x10^8 particles/mL for reliable measurement. Using a syringe pump speed of 100/AU (AU, arbitrary unit) to inject exosome suspension in the flow channel, videos of the particle's inflow were captured in script control mode, as five videos of 60 sec each with 1-sec delay and viscosity of water at 25 °C. A total of 1,500 frames per sample at a capture rate of 25 frames/sec at constant camera level for each experimental set were captured. The data were exported to Microsoft Excel, followed by analysis and plotting in GraphPad Prism.

4.2.9 Generation of whole cell lysate for western blotting

Differentiated HL-60 cells were washed once with DPBS and resuspended in RPMI1640 Phenol Red free (Gibco) with 20mM HEPES pH7.2 and treated with 2mM AEBSF hydrochloride for 15min while rotating. Cells were pelleted at 6000rcf for 30sec and resuspended in 1X Laemmli SDS sample buffer (Fisher Scientific AAJ61337AD) diluted in RPMI1640 Phenol Red free with 20mM HEPES pH7.2. Samples were boiled at 95˚C for 10 min, and 250,000 cells were loaded in

each well loaded on 4-20% Tris-Glycine gel (Invitrogen XP04205BOX) for electrophoresis. The proteins were transferred to 0.2um nitrocellulose membrane (MDI, SCNX8401XXXX101), blocked using 1X Fish gelatin (Fisher Scientific NC0382999) in TBS containing 0.1% Tween-20 and probed for specific proteins using antibody against cPLA$_2\alpha$ (1:1,000, Santa Cruz Biotechnology sc-376618), FLAP (1 μg ml^{-1}, Abcam 85227), 5-LO (1:1000, Abcam, ab169755), LTA$_4$H (1:1000 Protein Tech 13662-1-AP) and GAPDH (1:1000, Santa Cruz Biotechnology

4.2.10 Production of DexVs fibers for 3D under agarose assay

Dextran vinyl sulfone (DexVs) fiber mats were synthesized as described previously by Loesel et al. (Loesel, Hiraki et al. 2023). Briefly, to create electrospinning solution, DexVs was dissolved at 0.6mg/mL in 1:1 dimethylformamide (DMF)/MQ with 100 mg/mL lithium phenyl-2,4,6-trimethylbenzoylphosphinate (LAP), 0.75mM methacryloxyethyl thiocarbamoyl rhodamine B, and 5 vol% glycidyl methacrylate. DexVs solution was electrospun in a humidity-controlled glove box at 30% to 35% relative humidity. Electrospinning was performed at 0.2mL/h flow rate. To create aligned fibers, a 18mm^2 glass coverslip (Fisher scientific, 12546) was placed between two parallel copper electrodes set to -4.0kV. The stainless-steel needle containing the polymer solution was situated 7 cm from the collection surface and connected to the voltage source set to +4.0kV. Electrospun fibers were deposited onto the coverslip for 5min to achieve the desired thickness of the fiber mat. The fiber mats were crosslinked under ultraviolet light at 100mW/cm^2 for 20sec to stabilize the fibers. The coverslips are glued to the bottom of a modified 12-well plate using SYLGARD^{TM} 164 Silicone Elastomer kit (Dow, 0.4028273). The 12-well plates (Fisher Scientific, FB012928) were modified by drilling 15mm^2 holes at the bottom of a polystyrene 12 well plate using Dremel 7760 tool.

Before the experiment, the fiber mats were functionalized using 2.5%(w/v) heparin methacrylate dissolved in 1mg/mL LAP solution via 20s exposure to 100mW/cm2 ultraviolet light. The 12 well plates are sterilized using 70% ethanol for 10min followed by coating with 10µg/mL fibrinogen (Sigma, 4129) in DPBS for 1hr at 37˚C. The plates as then prepared for the under agarose assay as mentioned above.

4.2.11 Statistics and reproducibility

All data presented here is from at least three independent biological replicates. Appropriate tests for significance have been used to determine the level of confidence and variability in the data which is mentioned in the figure legends.

4.2.12 MATLAB code written by LEH for chemotaxis analysis

Below is the code used for chemotaxis analysis written by Lauren E. Hein. This code reorganizes the raw data collected from the chemotaxis tool in FIJI to simplify the subsequent analysis. It plots the graphs of individual cell tracks and calculates the X-forward migration index (X-FMI), speed, and accumulated distance of individual cells.

```
% Goal:  calculate the chemotactic index for each cell in an under agarose video
% Written by Lauren Hein, 2022

% clear the workspace and the command window
clear
clc

% ask user for the name of the file (used to load file, save new file, and
% title of spider plot
prompt1 = 'What is the name of the file?\n Place name in single quotes and do not use file
extension. \n';
name = input(prompt1);

% load file
% create file name by appending the file type to the file name provided by
% the user
```

```
file_csv = '.csv';
filename = append(name, file_csv);
% load the file
data = readmatrix(filename);

% create the file name to use for exported spreadsheet
file_xlsx = '_results.xlsx';
exported_results = append(name, file_xlsx);

% ask the user for time interval in seconds
prompt2 = 'What is the time interval in seconds?\n';
% adjust the time interval to be IN MINUTES
time_interval = input(prompt2)/60;

% extract relevant columns from the TrackMate file
% col 3:  track number, col 9:  frame, col 5:  x pos, col 6: y pos
% x and y coordinates are in microns
data2 = data(:, [3, 9, 5, 6]);
% make y-values negative so that it plots in the same orientation as the video
data2(:, 4) = data2(:, 4) * (-1);

% remove rows that contain NaN in the first column
% create a vector that uses Boolean logic to identify rows that contain NaN
NaN_data = isnan(data2(:, 1));
% use a loop to cycle through all rows (from the bottom up) to remove the
% rows that contain NaN
for nan_id = length(data2): -1 : 1;
   if isnan(data2(nan_id, 1)) == 1
      % delete the row
      data2(nan_id, :) = [];
   end
end

% sort rows based on cell id
data3 = sortrows(data2, 1);

% number of tracks/cell IDs in file (must add 1 because initial track index is 0)
n = max(data3(:, 1)) + 1;
% number of rows in file
l = length(data3);

% rescale matrix such that all tracks start at an imaginary origin of (0,0)
% set up new matrix (data4) with cell id and track number and zeros for columns 3
% and 4
data4 = [];
```

```
% create outputs matrix to hold calculated values
outputs = [];

%%%%%%%%% this is a series of nested loops that take all the info for one
%%%%%%%%% cell id, determine if the cell has traveled for longer than the
%%%%%%%%% desired threshold, normalize it to (0,0), plots the data, and
%%%%%%%%% calculates the XFMI, accumulated distance, speed, and Euclidian
%%%%%%%%% distance
% loop through all track number
for i = 0:(n-1)
    % set/reset group variable to 0
    group = 0;
    % set/reset adjusted position to 0
    adjusted_pos = 0;
    % set/reset counter to 1
    cc = 1;

    % run a for loop to cycle through every row of the data3 matrix, which
    % contains the data sorted by cell id
    for j = 1:l

        % determine if each row belongs to the current cell ID (i)
        if data3(j, 1) == i
            % assign cell id and track slice to new temporary matrix
            group(cc, 1) = data3(j, 1);
            group(cc, 2) = data3(j, 2);
            % assign x value of track
            group(cc, 3) = data3(j, 3);
            % assign y value of track
            group(cc, 4) = data3(j, 4);
            % update counter variable in order to save next data point to a
            % new row of the matrix (group)
            cc = cc + 1;
        end

    end

    % determine the dimensions of the group matrix
    % the size command returns (rows, columns) of a matrix
    s = size(group);
    % the number of rows (length) is equal to the first value of (size)
    lg = s(1);

    % calculate total time the cell traveled
    % determine the first slice in which the cell appeared (first row,
    % second column of "group" matrix)
```

```
slice_initial = group(1, 2);
% determine the last slice in which the cell appeared (first row,
% last column of "group" matrix)
slice_final = group(lg, 2);
% calculate the difference between the first and last slices
slice_lapse = slice_final - slice_initial;

% time the cell traveled in minutes
time_lapse = slice_lapse * time_interval;

% filter out tracks based on time traveled (in minutes)
% if the 'group' matrix contains data for a cell for which the time
% lapse is more than or equal to the indicated time, then the code will continue
% through this if statement and calculate the metrics of interest.  If it
% does not meet the time lapse criteria, it will exit this if statement
% and go back to line 71
if time_lapse >= 10
    % create a new matrix to hold the values of the adjusted position
    % of the cells
    adjusted_pos = zeros(lg, 4);
    % assign the cell id and slice number to the adjusted position
    % matrix
    adjusted_pos(:, 1:2) = group(:, 1:2);
    % define the amount to adjust the x position by using the x
    % position from the the first slice of the cell
    adjustx = group(1, 3);
    % define the amount to adjust the y position by using the y
    % position from the the first slice of the cell
    adjusty = group(1, 4);

    % loop through all slices of the cell's data and subtract the
    % 'adjustx' value from the x position data and the 'adjusty' value
    % from the y position data (results in the origin being (0,0) and
    % everything else being adjusted accordingly)
    for ap = 1:lg
        % x position calculation, assign new value to the adjusted
        % position matrix
        adjusted_pos(ap, 3) = group(ap, 3) - adjustx;
        % y position calculation, assign new value to the adjusted
        % position matrix
        adjusted_pos(ap, 4) = group(ap, 4) - adjusty;
    end

    % continue with cells that have a final x position of at least 15
    % microns
    if adjusted_pos(lg,3) >= 100 | adjusted_pos(lg,3) <= -100
```

```
% add adjusted position matrix for this particular track to a new
% combined data vector
data4 = vertcat(data4, adjusted_pos);

% plot all data that has been rescaled to start at the origin
plot(adjusted_pos(:, 3), (adjusted_pos(:, 4)))
hold on


%%%%%%%%% calculate XFMI for each cell
% first calculate the accumulated distance by summing the distance
% between each data point
% set/reset accumulated distance variable to 0
acc_dist = 0;
% loop through the adjusted position matrix for this cell ID
for z = 1:(lg-1)
   % assign x1 and y1
   x1 = adjusted_pos(z, 3);
   y1 = adjusted_pos(z, 4);
   % assign the next point as x2 and y2
   x2 = adjusted_pos((z+1), 3);
   y2 = adjusted_pos((z+1), 4);
   % use the distance formula to calculate the distance between
   % two points
   dist = sqrt((x2 - x1)^2 + (y2 - y1)^2);
   % add the distance calculated to the accumulated distance
   % variable
   acc_dist = acc_dist + dist;
end

% then calcualte XFMI using accumulated distance and final x
% position
x_final = adjusted_pos(lg, 3);
XFMI = x_final / acc_dist;
   % if the cell does not travel, the accumulated distance will be
   % equal to 0, resulting in an XFMI of NaN.  If this is the
   % case, change the XFMI to zero because the cell did not
   % chemotax in any direction
   if isnan(XFMI) == 1
      % change value to 0
      XFMI = 0;
   end

% calculate average speed in um/min (total time the cell traveled
% is calculated earlier in the code to determine which tracks to
```

```
        % include based on time of track; accumulated distance is also
        % calculated earlier)
        speed = acc_dist / time_lapse;

        % calculate the Euclidian distance (initial position is 0
        % because all data points have been normalized to origin)
        y_final = adjusted_pos(lg, 4);
        % use the distance formula to calculate the distance between the
        % final and initial points of the cell
        Euc_dist = sqrt((x_final - 0)^2 + (y_final - 0)^2);

        % calculate theta (degrees)
        theta = atan2d(y_final, x_final);

        % add cell number, XFMI, speed, accumulated distance, and theta
        % (degrees)
        % to temporary cell output matrix
        cell_outputs = [adjusted_pos(1, 1) XFMI speed acc_dist Euc_dist theta];

        % append cell track number, XFMI, speed, accumulated distance,
        % and theta to outputs summary matrix
        outputs = vertcat(outputs, cell_outputs);
      end
    end
    % repeat back to line 71 to continue loop for next cell ID/track number
end

%%%%% format plot
% plot a line at x = 0
xline_xvalues = zeros(1, 11);
xline_yvalues = [-500:100:500];
plot(xline_xvalues, xline_yvalues, 'k', 'LineWidth', 1)
hold on
% plot a line at y = 0
yline_xvalues = [-300:100:700];
yline_yvalues = zeros(1, 11);
plot(yline_xvalues, yline_yvalues, 'k', 'LineWidth', 1)
hold on
% axis [-x +x -y +y]
axis([-150 650 -500 500]);

% title
title(name, 'Interpreter', 'none')

% axis labels
xlabel('distance (microns)')
```

```
ylabel('distance (microns)')

% calculate average XFMI, speed, adn Euclidian distance for all cells
XFMI_average = mean(outputs(:, 2))
speed_average = mean(outputs(:, 3)) % um/min
Euc_dist_average = mean(outputs(:, 5)) % um

% original number of tracks
original_tracks = max(data3(:, 1))
% included number of tracks
final_size = size(outputs);
final_tracks = final_size(1)


% export the outputs table to an Excel spreadsheet
% add labels to the the columns in the outputs file
outputs_labeled = array2table(outputs, 'VariableNames', {'cell ID', 'XFMI',...
    'Speed (um/min)', 'accumulated distance (um)', 'Euclidian distance (um)',...
    'angle (deg)'});
writetable(outputs_labeled, exported_results);

%%%%%%%%%%%%%%%%%%%%%%%%%%%%%%%%%%%%%%%%%%%%%%%%%%%%%%%%%%%%%%%%%%%%%%%%%%%%
%%%%%%%%%%%%%%%%%%%%%%%%%%%%%%%%%%%%%%%%%%%%%%%%%%%%%%%%%%%%%%%%%%%%%%%%%%%%
```

4.3 Results

4.3.1 cPLA$_2$α localizes to three distinct regions in activated human neutrophils

To visualize the localization of cPLA$_2$α, we first generated a GFP-cPLA$_2$α plasmid construct and overexpressed it in HEK293T cells. As previously reported (Gijón and Leslie 1999, Gijón, Spencer et al. 1999, Leslie 2004, Leslie, Gangelhoff et al. 2010), we observed a rapid translocation of cytosolic GFP-cPLA$_2$α signal from the cytosol to the NE and perinuclear regions within 3 seconds following stimulation with the calcium ionophore A23187 (**Figure 4.2A, B**). We then generated HL-60 cells (neutrophil-like cells; see Chapters 2 and 3; (Tucker, Lilly et al. 1987)) stably overexpressing (OE) the same GFP-cPLA$_2$α construct. To assess cPLA$_2$α translocation in HL-60 cells, we perform time-lapse imaging of differentiated GFP-cPLA$_2$α OE HL-60 cells chemotaxing towards fMLF. However, we were not able to clearly visualize a change in the distribution of cPLA$_2$α under these conditions (**Figure 4.2C, D**). We next assessed the distribution of endogenous cPLA$_2$α in cytosolic and membrane fractions isolated from fMLF-stimulated HL-60 cells. We used GAPDH as a marker of cytosolic fraction and lamin B receptor (LBR) as the marker of membrane fraction. We also probed the fractions with an antibody against phosphor-ERK1/2 (pERK1/2) as a measure of cell activation in response to fMLF. While we measured clear cytosolic and membrane pools of cPLA$_2$α, we could not reproducibly observe a translocation to membrane pools in response to fMLF stimulation in these cells (**Figure 4.2E, F**). We next performed subcellular fractionation via hypotonic lysis of human peripheral blood-derived neutrophils stimulated with either 100nM fMLF or DMSO (vehicle control) (**Figure 4.3A**). We isolated cytosolic, ER, and nuclear fractions and subjected them to western blot analysis (**Figure 4.3B**). Interestingly, we found two distinct pools of cPLA$_2$α in human primary neutrophils that did not change in response to fMLF addition: one in the cytosol and another in the nucleus

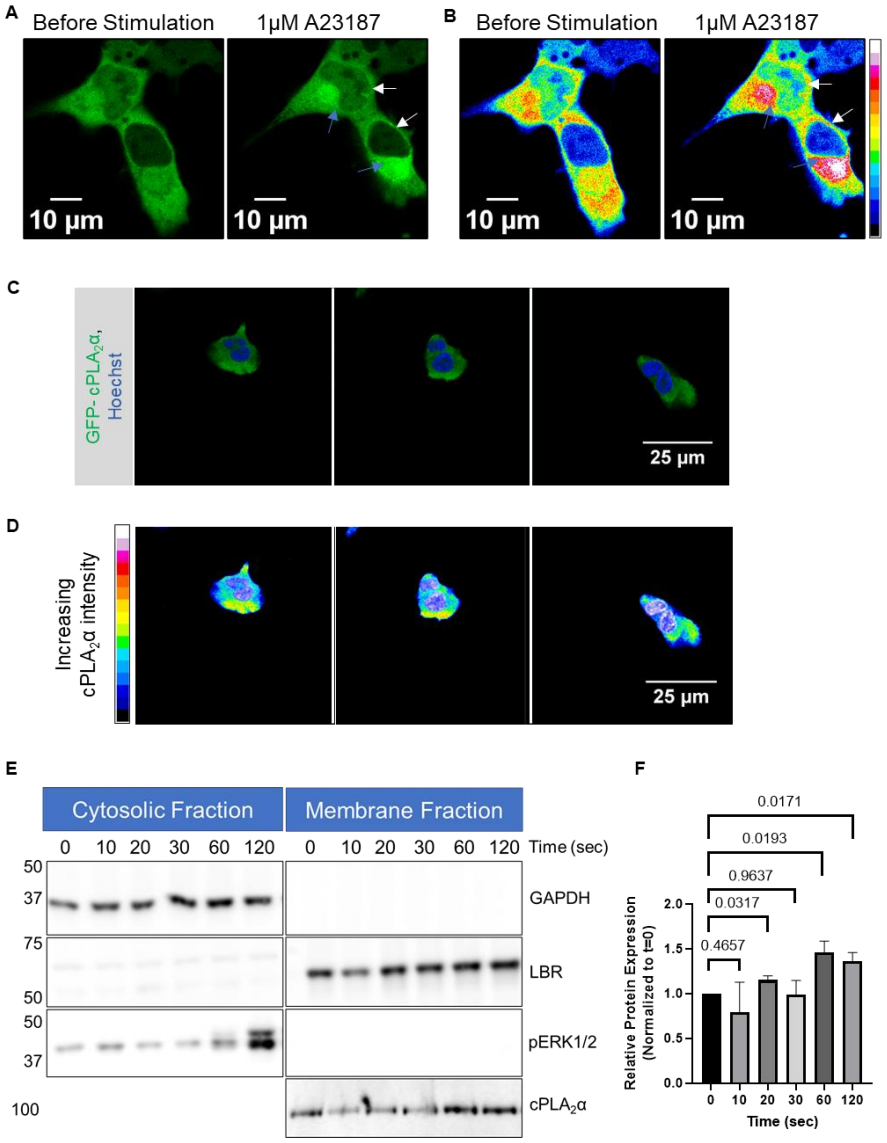

Figure 4.2: cPLA$_2$α translocates from the cytosol to the NE in HEK293T cells but not in HL-60 cells.

A. Representative fluorescent images of HEK293T cells expressing GFP-cPLA$_2$α before and 3 seconds after stimulation with 1μM A23187 with 2mM $CaCl_2$. White arrows point to the NE, and blue arrows point to the peri-nuclear region. **B.** Images showing the changes in GFP- cPLA$_2$α (scale on the right) before and after stimulation. **C.** Representative time-lapse images of differentiated HL-60 cells expressing GFP- cPLA$_2$α chemotaxing towards 100nM fMLF. Images were taken at 15, 20, and 25min intervals after the cells entered agarose. Scale bar is 25μm. **D.** Time-lapse images showing the signal fluorescence intensity (scale on the right) of GFP- cPLA$_2$α in differentiated HL-60 cells migrating towards 100nM fMLF. **E.** Representative western blot showing the presence of cPLA$_2$α membrane fractions of differentiated HL-60 cells after stimulation with 1μM fMLF. **F.** Quantification of the fractionation assays in E (n=3).

(**Figure 4.3B, C**). We next attempted to visualize this using immunofluorescent imaging (IF) with the antibody against cPLA$_2$α we used for Western analysis: a monoclonal antibody targeting the C-terminus of cPLA$_2$α. Surprisingly, we did not observe the nuclear pool in the fixed samples (**Figure 4.3D**).

To further investigate the role and distribution of cPLA$_2$α, we generated *cPLA$_2$α$^{-/-}$* HL-60 cells using the CRISPR/Cas9 technology. We also generated scramble (SCR) control and GFP-cPLA$_2$α rescue (GFP-cPLA$_2$α/*cPLA$_2$α$^{-/-}$*) HL-60 cells. The KO status of the cPLA$_2$α$^{-/-}$ cells was confirmed using genetic sequencing (**Figure 4.4A**) and western blot analysis (**Figure 4.4B, C**). Additionally, we used the *cPLA$_2$α$^{-/-}$* cells to validate the cPLA$_2$α antibody we used for IF imaging of the human primary neutrophils (see **Figure 4.3D**). Remarkably, this antibody gives rise to non-specific signal in the *cPLA$_2$α$^{-/-}$* cells (**Figure 4.4D**). We then tested several other commercially available antibodies against cPLA$_2$α and found that they picked up signals in various cellular localizations (**Figure 4.4E-H**). Some antibodies showed a cytosol-exclusive localization (**Figure 4.4E, H**), while others showed nucleus-exclusive staining (**Figure 4.4G**). A few antibodies showed cytosolic and nuclear localization (**Figure 4.4D, F**). Remarkably, all antibodies tested gave rise to similar signals in the *cPLA$_2$α$^{-/-}$* cells (**Figure 4.4E-H**). Therefore, we used a GFP antibody and the GFP-cPLA$_2$α/*cPLA$_2$α$^{-/-}$* HL-60 cells to visualize cPLA$_2$α localization. Differentiated GFP-cPLA$_2$α/*cPLA$_2$α$^{-/-}$* HL-60 cells were allowed to directionally migrate towards 100nM fMLF for 2hrs, fixed with paraformaldehyde (PFA), and stained with a GFP antibody (**Figure 4.5**). **Figure 4.5A** shows a montage of various migrating cells. As we observed in human primary neutrophils, we found that cPLA$_2$α localizes to both the cytosol and the nucleus of chemotaxing cells (**Figure 4.5A**). Additionally, we observed that cPLA$_2$α localized to nuclear folds and in perinuclear regions (**Figure 4.5A, B, orange arrows and orange boxes**).

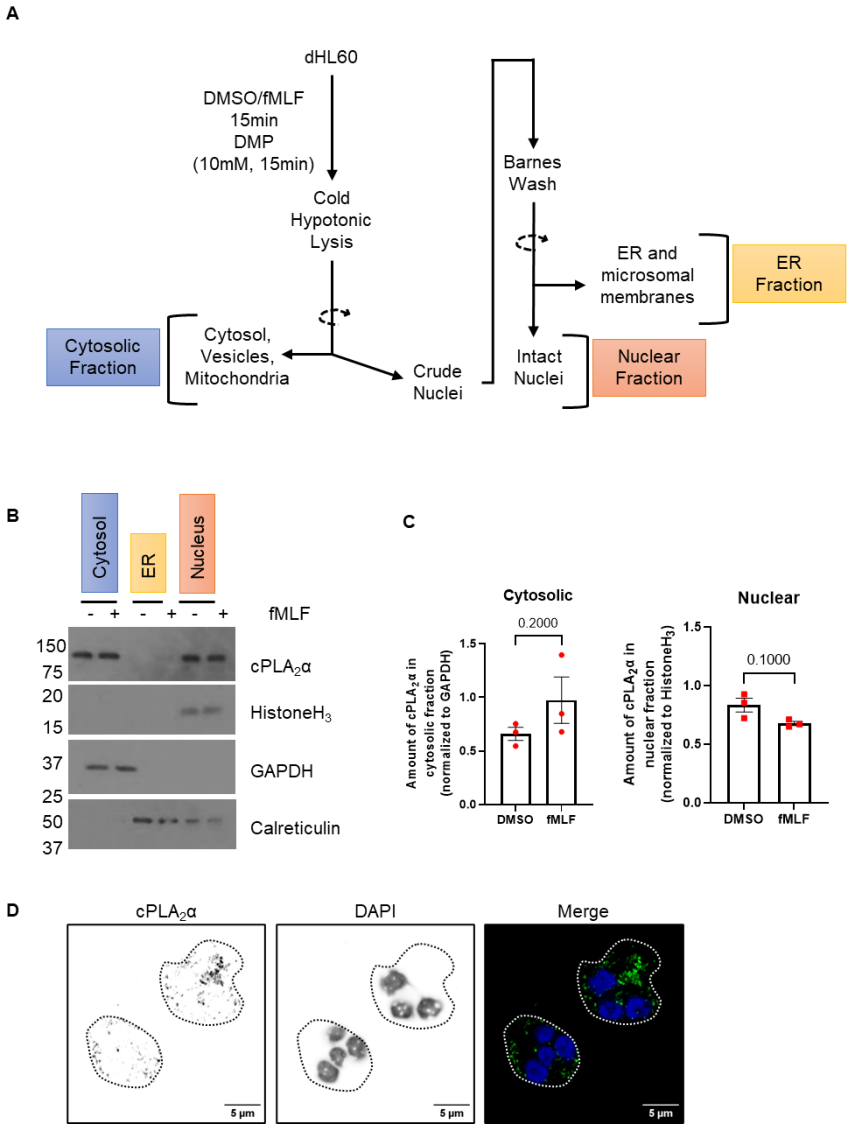

Figure 4.3: cPLA$_2$α is distributed in the cytosol and nucleus in resting and activated human neutrophils.

A. Schematic representation of the subcellular fractionation workflow to isolate the cytosolic, ER, and nuclear fractions from human peripheral blood neutrophils stimulated with either DMSO or 100nM fMLF. **B.** Representative western blot showing the subcellular fractionation of cPLA$_2$α in resting and activated neutrophils. GAPDH was used as a marker for the cytosol. Histone H_3 was used as a nuclear, and calreticulin was used as a marker for ER fractions. **C.** Quantification of western blots presented in B. GAPDH was used to normalize the protein amount in the cytosol, and HistoneH_3 was used to normalize the protein amount in the nucleus. Mann-Whitney test was used to test the statistical significance of the data. $p \leq 0.05$ was considered significant (n=3). **D.** Representative fluorescent images of neutrophils uniformly stimulated with 100nM fMLF and stained with the cPLA$_2$α SCBT-E1 antibody at 1:200 dilution.

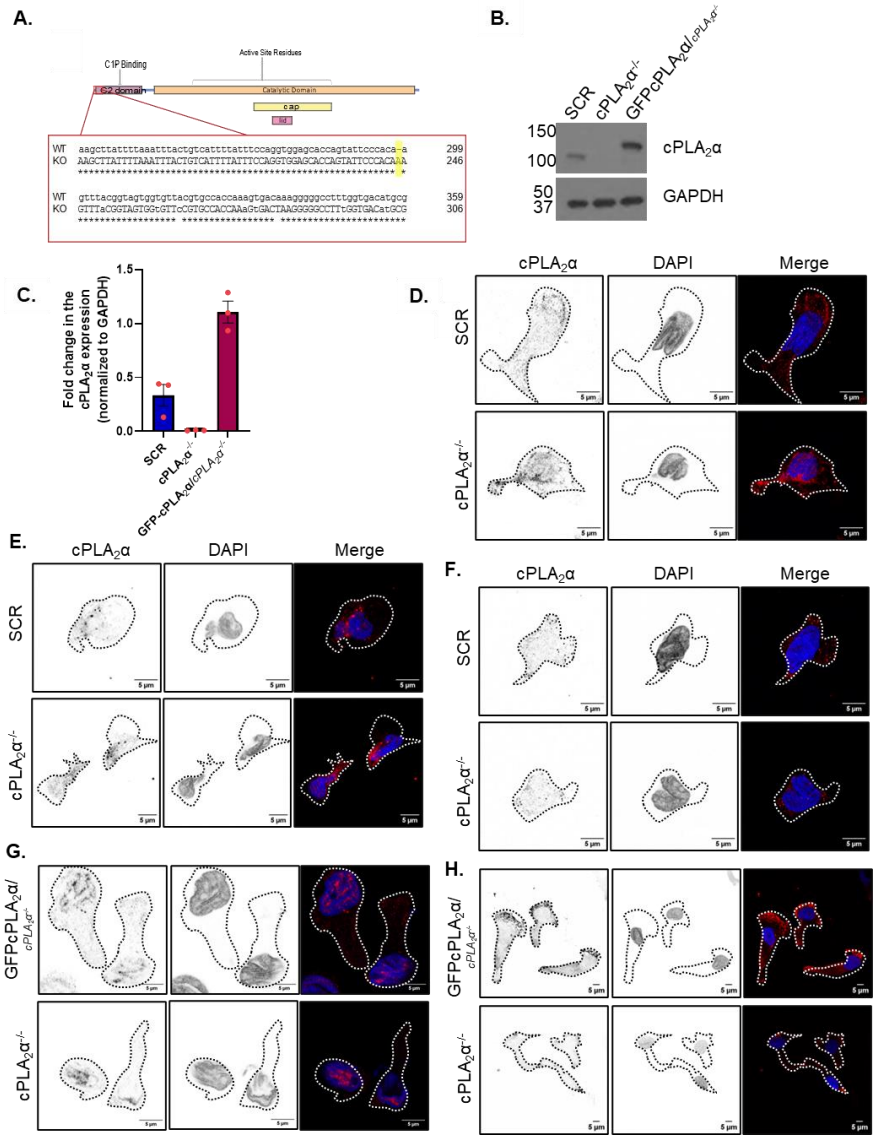

Figure 4.4: cPLA$_2$α antibodies show non-specific signal in the *cPLA$_2$α$^{-/-}$* cells.

A. Schematic representation of the cPLA$_2$α protein showing the location of the mutation (highlighted in yellow) that led to the generation of *cPLA$_2$α$^{-/-}$* cells. **B-C.** Western blot **(B)** and quantification **(C)** showing the expression of cPLA$_2$α in *cPLA$_2$α$^{-/-}$* and GFP-cPLA$_2$α/*cPLA$_2$α$^{-/-}$* cells using SCBT-E1 (ac-376618) at 1:1000 dilution. **D-H.** Representative fluorescent images of fixed SCR, *cPLA$_2$α$^{-/-}$* and GFP-cPLA$_2$α/*cPLA$_2$α$^{-/-}$* cells chemotaxing towards 100nM fMLF, stained overnight with either of the following antibodies against cPLA$_2$α: SCBT-E1 (D), Abcam KO validated (ab73406) (E), or SCBT-4-4B-4C (sc454) (F), at 1:100 dilution in DPBS; or with CST S505 Phospho-cPLA$_2$α (2831S) (G), or Abcam (ab58375) (H) at 1:200 dilution in 2% goat serum in DPBS.

We quantified the localization of GFP-cPLA$_2$α by creating regions of interest (ROI) around the whole cell (**Figure 4.5C, black outline**), the nucleus (**Figure 4.5C, red outline**) and the perinuclear regions (**Figure 4.5C, blue outline**) and found that while ~75% of the signal is present in the cytosol, we measured strong GFP-cPLA$_2$α signal in the nucleus and on islands in perinuclear regions (**Figure 4.5C, D**). Together, these results show that GFP-cPLA$_2$α localizes to three distinct regions in the chemotaxing neutrophil-like cells (**Figure 4.5D**).

4.3.2 cPLA$_2$α is not required for the formation of ceramide-rich lipid-ordered microdomains

We recently reported that NE buds that contain the LTB$_4$ synthesis machinery emerge from ceramide-rich lipid-ordered microdomains (Arya, Chen et al. 2022). Since we found that cPLA$_2$α localizes to the nucleus and peri-nuclear regions in chemotaxing neutrophils (**Figure 4.5**), we hypothesized that the clustering of cPLA$_2$α on NE microdomains is responsible for the generation of AA required for LTB$_4$ biogenesis. To test this, we isolated intact nuclei from either DMSO- or fMLF-treated differentiated GFP-cPLA$_2$α/*cPLA$_2$α*$^{-/-}$ HL-60 cells and stained with GFP- and ceramide-specific antibodies, as previously performed (Arya, Chen et al. 2022). As expected, we found distinct clusters of cPLA$_2$α on the nuclei in DMSO- and fMLF-treated neutrophils (**Figure 4.6A, top panels**). In nuclei harvested from fMLF-treated cells, we also observed an increase in the co-occurrence of GFP-cPLA$_2$α clusters with ceramide (**Figure 4.6A, bottom panels, B**) and noticed that the GFP-cPLA$_2$α positive punctae were present flanking the ceramide punctae (**Figure 4.6A, yellow arrowheads**). We envision that the lack of colocalization signals between GFP-cPLA$_2$α and ceramide (Pearson's R=0.2, **Figure 4.6C**) is due to their involvement with distinct membrane curvatures: cPLA$_2$α induce positive curvatures, whereas ceramides generate negative curvatures.

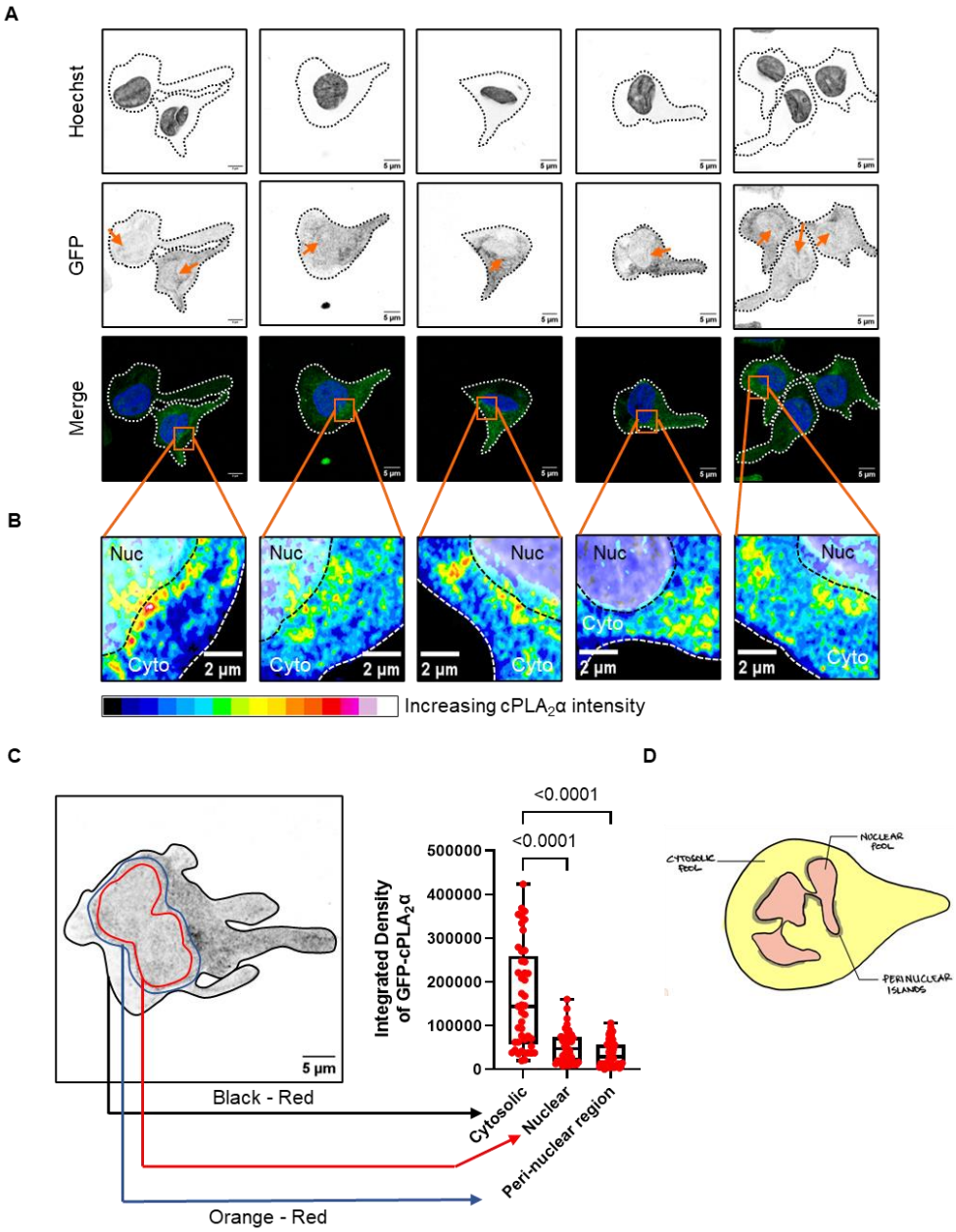

Figure 4.5: Three distinct cellular pools of cPLA$_2$α in chemotaxing neutrophil-like cells.

A. Representative fluorescent images of differentiated GFP-cPLA$_2$α/*cPLA$_2$α*$^{-/-}$ cells chemotaxing towards 100nM fMLF, fixed, and stained with the GFP antibody at 1:2000 dilution in 2% goat serum in DPBS. **B.** Zoomed sections showing the signal fluorescence intensity (scale on bottom) at the perinuclear region of the GFP signal in differentiated GFP-cPLA$_2$α/*cPLA$_2$α*$^{-/-}$ cells. **C.** Representative fluorescent image showing the ROI used for the quantification of GFP-cPLA$_2$α signal from cells in panel A. Mann-Whitney test was used to determine the statistical significance of the data. Each dot represents a cell from n=3 biological replicates. **D.** Cartoon depicting the different cPLA$_2$α pools in chemotaxing neutrophil-like cells.

As discussed in Chapter 2, lipid-ordered domains resist solubilization in non-ionic detergents (Magee and Parmryd 2003). To assess the role of cPLA$_2$α in the generation of ceramide-rich lipid-ordered domains, we next isolated nuclei from DMSO- and fMLF-stimulated SCR, *cPLA$_2$α$^{-/-}$* and GFP-cPLA$_2$α/*cPLA$_2$α$^{-/-}$* differentiated HL-60 cells and fractionated detergent-resistant (lipid–ordered) membranes (DRMs) and detergent soluble (lipid–disordered) membranes (DSMs) ((Arya, Chen et al. 2022) and Chapter 2). Corroborating the microscopy data on isolated nuclei, we detected the presence of cPLA$_2$α in the DRM fractions (**Figure 4.6D**). Interestingly, we found that cPLA$_2$α depletion did not alter fMLF-induced DRM formation as reflected by no change in levels of flotillin 2, a marker of lipid-ordered domains, in the DRMs. Similarly, both nSMase1 and FLAP maintained their presence in DRM fractions in the absence of cPLA$_2$α (**Figure 4.6D** and Chapter 2). Together, these findings demonstrate that while cPLA$_2$α localizes at the NE and nuclear folds, it is not required for the formation of ceramide-rich lipid-ordered microdomains.

4.3.3 cPLA$_2$α is present on the outer surface of LTB$_4$-containing exosomes

We previously reported that LTB$_4$, along with its synthesizing enzymes, is secreted within exosomes (Majumdar, Tavakoli Tameh et al. 2021). Since we found that cPLA$_2$α is not required for the formation of the ceramide-rich lipid-ordered microdomains (**Figure 4.6**), we next tested if cPLA$_2$α depletion regulates exosomal release by performing NanoSight NTA particle analysis of isolated exosomes. We found that fMLF-stimulated *cPLA$_2$α$^{-/-}$* differentiated HL-60 cells release a similar number and size of exosomes compared to SCR and GFP-cPLA$_2$α/*cPLA$_2$α$^{-/-}$* cells (**Figure 4.7A, B**), although we did encounter some variation between experiments. We envision that this is due to slight differences in the differentiation states of the cells. We next assessed the protein content of these exosomes by western blot analysis. We observed no significant differences in levels of CD63, FLAP, or Flotillin 2 in exosomes isolated from SCR, *cPLA$_2$α$^{-/-}$*, and GFP- cPLA$_2$α/

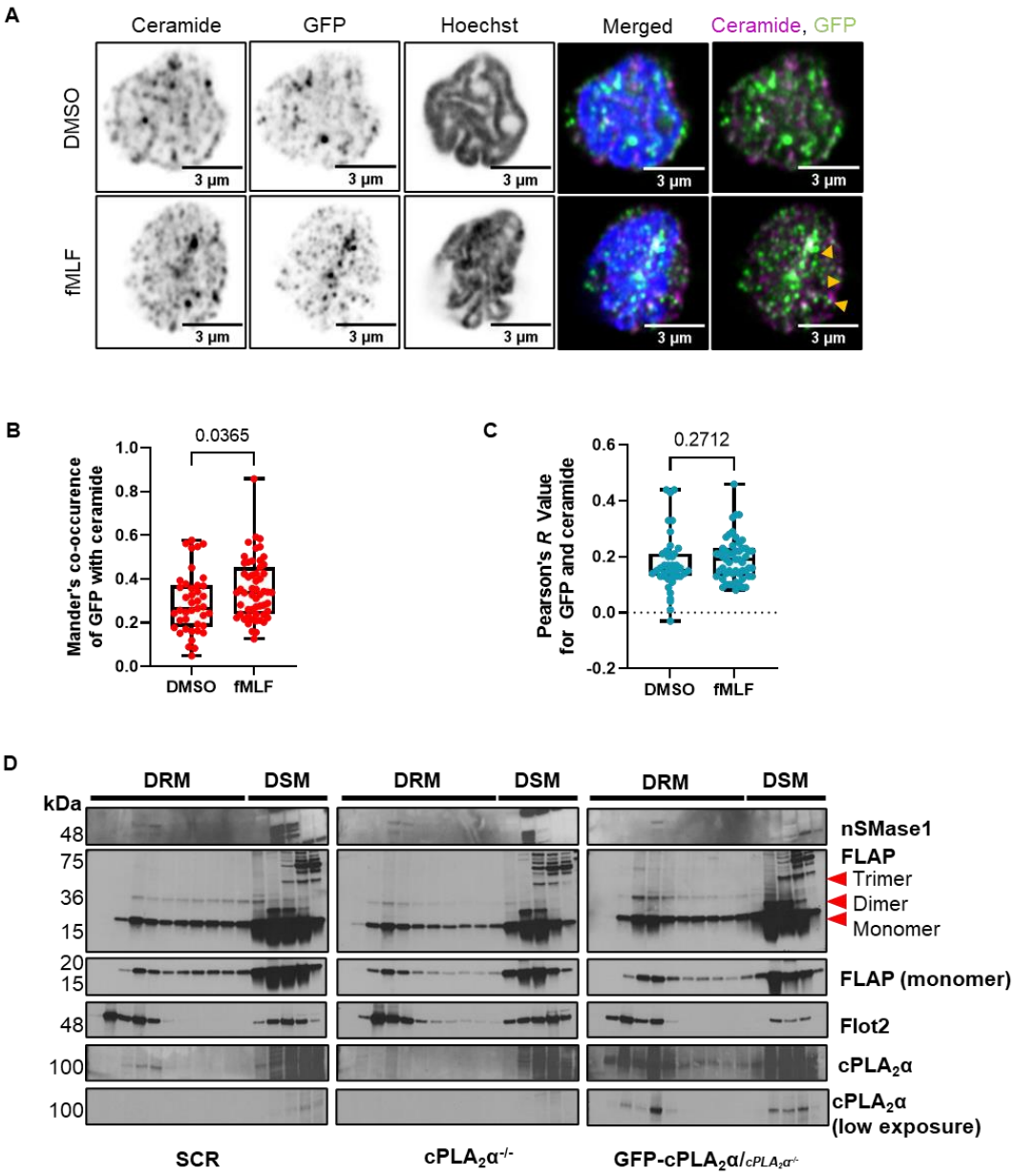

Figure 4.6: cPLA$_2$α is not required for the formation of ceramide-rich lipid-ordered microdomains. **A.** Representative fluorescent images of isolated nuclei from differentiated GFP-cPLA$_2$α/*cPLA$_2$α*$^{-/-}$ cells stimulated with either DMSO or 100nM fMLF for 15min, fixed and co-stained overnight with antibodies against GFP (1:1500) and ceramide (1:200) diluted in 2% goat serum (n=3). **B-C.** Colocalization of GFP punctae with ceramide punctae was determined using the Coloc2 plugin in FIJI. The Mander's co-occurrence factor **(B)** and Pearson's R-value **(C)** were plotted using GraphPad Prism. Mann-Whitney test was used to determine the statistical significance of the data. Each dot represents a cell from n=3 biological replicates. **D.** Representative western blots showing the presence of various proteins in the DRM and DSM fractions isolated from the NE of SCR, *cPLA$_2$α*$^{-/-}$ and GFP-cPLA$_2$α/*cPLA$_2$α*$^{-/-}$ cells stimulated with 100nM fMLF (n=3).

cPLA$_2\alpha^{-/-}$ cells (**Figure 4.7C, D**). Notably, we found the presence of cPLA$_2\alpha$ in exosomes derived from SCR and GFP-cPLA$_2\alpha$/*cPLA$_2\alpha^{-/-}$* cells (**Figure 4.7C, D**). Based on these results, we hypothesize that the presence of cPLA$_2\alpha$ in exosomes is required for the biogenesis of LTB$_4$. To test this, we performed LTB$_4$ ELISA on exosome preparations. As expected, we did not measure any detectable LTB$_4$ in exosomes isolated from *cPLA$_2\alpha^{-/-}$* cells, compared with high levels measured in either SCR or GFP-cPLA$_2\alpha$/*cPLA$_2\alpha^{-/-}$* cells (**Figure 4.7E**). Based on these results, we conclude that although cPLA$_2\alpha$ is not required for the production or secretion of NE-derived exosomes, it is required for exosomal LTB$_4$ production.

We next set out to investigate which cellular pool of cPLA$_2\alpha$ is delivered to exosomes. To test this, we partially stripped exosomes isolated from differentiated GFP-cPLA$_2\alpha$/*cPLA$_2\alpha^{-/-}$* HL-60 cells of their external cargo by limited treatment with trypsin (Cvjetkovic, Jang et al. 2016). Trypsin treatment of exosomes will degrade proteins on the outer surface of the exosome, but the proteins inside the exosomes will remain protected. As it is well established that cPLA$_2\alpha$ induces and preferentially binds to membranes with positive curvatures (Ward, Ropa et al. 2012, Ward, Bhardwaj et al. 2013, Ward, Sengupta et al. 2020), we hypothesized that exosomal cPLA$_2\alpha$ is coming from the nuclear pool, to interact with positive curvatures (see **Figure 4.7H**). In this situation, cPLA$_2\alpha$ would therefore be associated with the outer corona of exosomes and be sensitive to trypsin digestion. Indeed, we found that cPLA$_2\alpha$ was completely degraded upon trypsin treatment (**Figure 4.7F, G**), while levels of Flotillin 2, a protein known to be present in the lumen of exosomes (Cvjetkovic, Jang et al. 2016), remain unchanged after trypsin digestion. Similarly, trypsin treatment did not affect the 5-LO signal, indicating that 5-LO also resides inside

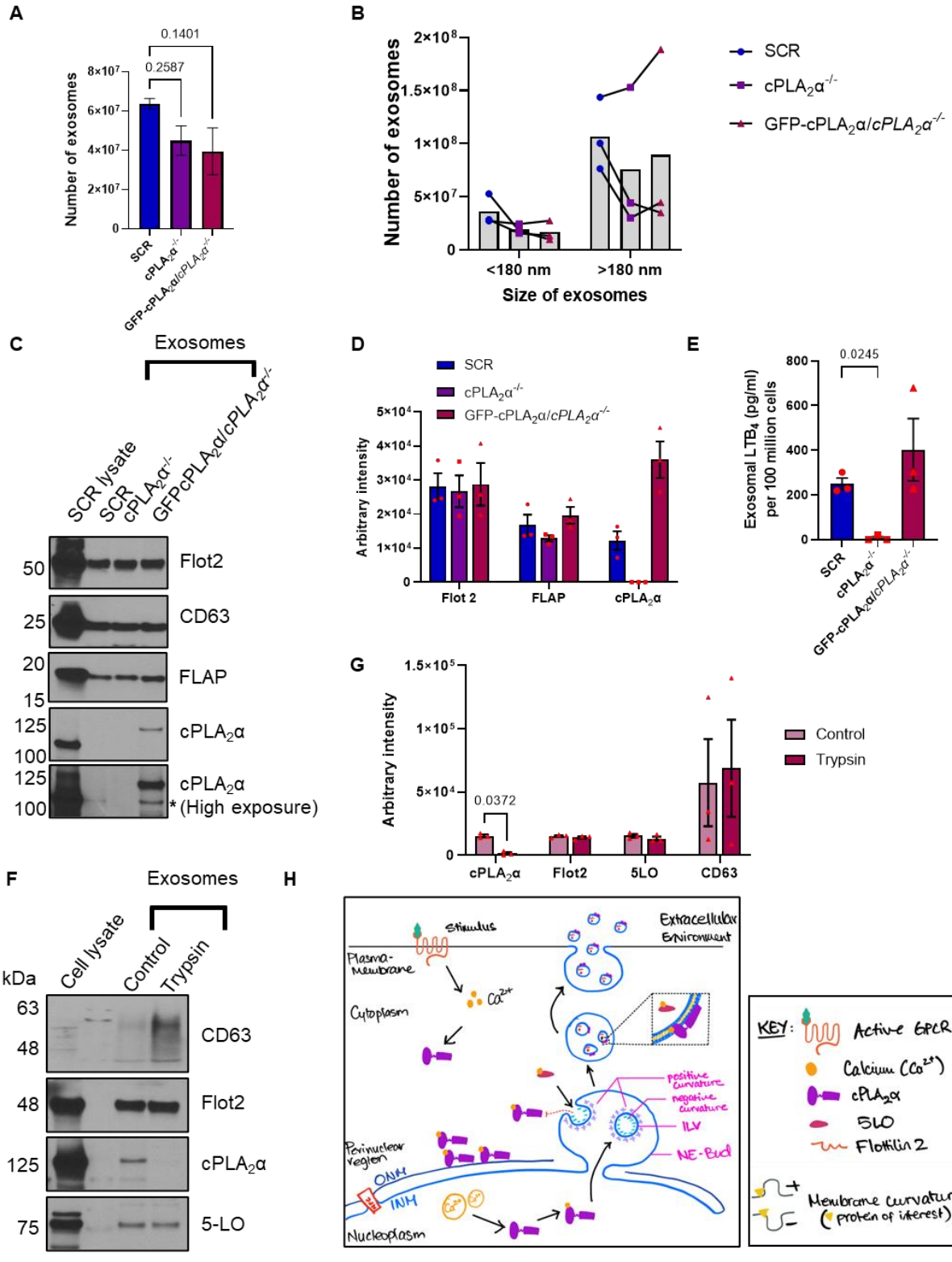
A
Number of exosomes
0.1401
0.2587
SCR
cPLA2α-/-
GFP-cPLA2α/cPLA2α-/-
B
Number of exosomes
<180 nm
>180 nm
Size of exosomes
SCR
cPLA2α-/-
GFP-cPLA2α/cPLA2α-/-
C
Exosomes
SCR lysate
SCR
cPLA2α-/-
GFPcPLA2α/cPLA2α-/-
Flot2
CD63
FLAP
cPLA2α
cPLA2α
* (High exposure)
D
SCR
cPLA2α-/-
GFP-cPLA2α/cPLA2α-/-
Arbitrary intensity
Flot 2
FLAP
cPLA2α
E
Exosomal LTB4 (pg/ml) per 100 million cells
0.0245
SCR
cPLA2α-/-
GFP-cPLA2α/cPLA2α-/-
F
Exosomes
kDa
Cell lysate
Control
Trypsin
CD63
Flot2
cPLA2α
5-LO
G
Arbitrary intensity
0.0372
cPLA2α
Flot2
5LO
CD63
Control
Trypsin
H
Extracellular Environment
Stimulus
Plasma-Membrane
Cytoplasm
Ca2+
positive curvature
negative curvature
ILV
NE-Bud
Perinuclear region
ONM
INM
Nucleoplasm
KEY:
Active GPCR
Calcium (Ca2+)
cPLA2α
5LO
Flotillin 2
Membrane curvature (protein of interest)

Figure 4.7: cPLA$_2$α is present on the outer surface of LTB$_4$-containing exosomes.

A. Bar graph showing the particle count of exosomes purified from differentiated SCR, *cPLA$_2$α$^{-/-}$* and GFP-cPLA$_2$α/*cPLA$_2$α$^{-/-}$* cells stimulated with 100nM fMLF for 30min. Data were obtained from nanoparticle tracking analysis (NTA) of isolated exosomes and are plotted from n=3 experiments as mean ± SEM. **B.** Quantification of the area under the curve from the NTA data. Data from n=3 independent experiments are presented. **C.** Representative, western blot images showing the levels of Flotillin 2, CD63, FLAP, and cPLA$_2$α in pooled fractions 4–9 of density-gradient purified exosomes isolated from differentiated SCR, *cPLA$_2$α$^{-/-}$* or GFP-cPLA$_2$α/*cPLA$_2$α$^{-/-}$* cells stimulated with 100nM fMLF for 30min. SCR cell lysates represent the amount of protein from 1/100th the number of cells used for exosome isolation (n = 3). *indicates degraded GFP-cPLA$_2$α in exosomes from GFP-cPLA$_2$α/*cPLA$_2$α$^{-/-}$* cells **D.** Bar graph showing the quantifications of the band intensity of Flotillin 2, FLAP and cPLA$_2$α in SCR, *cPLA$_2$α$^{-/-}$* and GFP-cPLA$_2$α/*cPLA$_2$α$^{-/-}$* exosomes. Three data points are plotted as mean ± SEM where each red dot represents the value from one experiment. **E.** Bar graph showing exosomal LTB$_4$ levels from the differentiated SCR, *cPLA$_2$α$^{-/-}$* and GFP-cPLA$_2$α/*cPLA$_2$α$^{-/-}$* cells stimulated with 100nM fMLF for 15 min. Data from three independent experiments are plotted as mean ± SEM. P value was obtained using two-tailed ratio paired t-test. **F.** Representative, western blot images, showing the levels of CD63, Flotillin 2, 5-LO, and cPLA$_2$α in exosomes purified from GFP-cPLA$_2$α/*cPLA$_2$α$^{-/-}$* cells stimulated with 100nM fMLF for 30min and treated with or without 50µg/mL trypsin for 30min. **G.** Bar graph showing the quantifications of panel F. Three data points are plotted as mean ± SEM where each red dot represents the value from one experiment. P values determined using two-tailed paired multiple t-test are reported. **H.** Cartoon depicting the proposed mechanism for the biogenesis of LTB$_4$-containing exosomes from stimulated neutrophils.

exosomes (**Figure 4.7E, F**). These findings suggest that exosomal cPLA$_2$α originates from the nuclear pool. Based on these results and the knowledge that cPLA$_2$α preferentially translocates to membranes with high positive curvature (Stahelin, Subramanian et al. 2007, Ward, Ropa et al. 2012, Ward, Sengupta et al. 2020), we propose that upon chemoattractant stimulation, the activated nuclear pool of cPLA$_2$α translocates to ILVs of emerging NE buds and locally releases AA required for LTB$_4$ biogenesis (**Figure 4.7H**).

4.3.4 cPLA$_2$α plays a critical role in maintaining the nuclear architecture

Our findings show that cPLA$_2$α localizes to the nucleus and perinuclear regions of neutrophils and neutrophil-like cells (**Figure 4.3 and Figure 4.5**). Since cPLA$_2$α has been shown to maintain lipid homeostasis (Brown, Chambers et al. 2003, Ha, Clarke et al. 2012) and induce membrane curvatures (Cho and Stahelin 2005, Lamour, Stahelin et al. 2007, Stahelin, Subramanian et al. 2007, Ward, Ropa et al. 2012, Ward, Bhardwaj et al. 2013, Ward, Sengupta et al. 2020), we hypothesized that cPLA$_2$α is involved in maintaining nuclear architecture in chemotaxing neutrophils. To test this, we allowed differentiated SCR, *cPLA$_2$α$^{-/-}$* and GFP-cPLA$_2$α/*cPLA$_2$α$^{-/-}$* cells to directionally migrate under agarose towards 100nM fMLF. The cells were fixed and stained with an LBR antibody to visualize nuclear architecture. Similar to human primary neutrophils, differentiated HL-60 cells have irregularly shaped nuclei with multiple folds. This feature can be observed in our SCR and GFP-cPLA$_2$α/*cPLA$_2$α$^{-/-}$* HL-60 cells (**Figure 4.8A**, Top and bottom panels). However, the nuclei of *cPLA$_2$α$^{-/-}$* HL-60 cells were strikingly different (**Figure 4.8A, middle panel**). Whereas SCR and GFP-cPLA$_2$α/*cPLA$_2$α$^{-/-}$* nuclei showed multiple distinct nuclear folds, *cPLA$_2$α$^{-/-}$* nuclei appeared larger and showed a reduced number of nuclear folds. Using the Imaris 9.91 software to quantify changes in nuclear morphology, we found that *cPLA$_2$α$^{-/-}$* nuclei were significantly larger and flatter compared with control nuclei (**Figure 4.8B,**

C). These results lead us to conclude that cPLA$_2$α is required to maintain the nuclear architecture in chemotaxing neutrophil-like cells.

4.3.5 cPLA$_2$α is not required for chemotaxis within engineered fiber mats

The nucleus is the largest organelle in the cell and has been shown to be involved in the ability of cells to sense their surrounding environment (Guilluy, Osborne et al. 2014, Kirby and Lammerding 2018, Ross and Stroud 2021). Since *cPLA$_2$α$^{-/-}$* cells show altered nuclear morphology, we hypothesized that these cells would have difficulty migrating within confined environments. To test this, we assessed the ability of SCR, *cPLA$_2$α$^{-/-}$* and GFP-cPLA$_2$α/*cPLA$_2$α$^{-/-}$* cells to chemotax towards fMLF on synthetic fiber mats (DexVs fibers mats), which have been used to study cell migration in complex environments (Loesel, Hiraki et al. 2023). Surprisingly, we found no defects in the ability of the cell lines to migrate on aligned fiber mats (**Figure 4.9**). SCR, *cPLA$_2$α$^{-/-}$* and GFP-cPLA$_2$α/*cPLA$_2$α$^{-/-}$* cells were able to sense the micro-topographies as depicted by the aligned traces of cells migrating on the fiber mats (**Figure 4.9B, C**) and showed no differences in their speed, directionality or distance covered (**Figure 4.9D-F**). Furthermore, as we observed with breast cancer cell lines (Loesel, Hiraki et al. 2023), we found that all cell lines migrated faster and traveled further on glass than on fiber mats (**Figure 4.9G**). We envision that this is due to the lack of complexity and increased stiffness of glass coverslips (Lo, Wang et al. 2000, Rens and Merks 2020).

A caveat of using fiber mats is that it is difficult to control the distance between fibers and the confinement the cells are experiencing. Instead, the cells migrate through a mesh of fibers with varying sparsity. It has previously been determined that cPLA$_2$α regulates migration under very specific compressions of 3μm (Lomakin, Cattin et al. 2020, Venturini, Pezzano et al. 2020). We, therefore, decided to visualize the migration of the SCR and cPLA$_2$α$^{-/-}$ cells within the fiber mats

at higher magnification. Specifically, we compared regions where cells had to navigate fibers tightly packed (≤3μm distance between fibers) fiber mats versus sparse (>3μm distance between fibers) fiber mats. Interestingly, we found that when challenged with closely packed fiber mats, the nuclei of SCR cells were able to align along the fibers and squeeze through (**Figure 4.10A**). However, under similar conditions, the nuclei of *cPLA$_2$α$^{-/-}$* cells were unable to squeeze through and mainly stayed on top of the fibers (**Figure 4.10**B). Together, these results show that cPLA$_2$α is required for the cells to migrate through tight (≤3μm) spaces.

4.4 Discussion

Neutrophils are the first cells to respond to sites of infection or injury, and the LTB$_4$ signaling pathway has been shown to play a key role in neutrophil extravasation (Shah, Burg et al. 2017, Subramanian, Melis et al. 2020) and chemotaxis (Lammermann, Afonso et al. 2013, Majumdar, Tavakoli Tameh et al. 2021) towards damaged sites. Additionally, cPLA$_2$α activity has been implicated in LTB$_4$ generation since the early 1990s (Peters-Golden and McNish 1993). In this study, we show that cPLA$_2$α is not only involved in LTB$_4$ generation but is also responsible for maintaining nuclear architecture in neutrophils.

The cellular distribution of cPLA$_2$α differs depending on the cell type. In epithelial cells, such as Madin-Darby canine kidney (MDCK), human embryonic kidney (HEK293T), and A549 lung carcinoma cells, overexpressed human cPLA$_2$α localizes exclusively to the cytosol and translocates to the internal organelles upon ionophore stimulation (Gijón, Spencer et al. 1999, Evans, Spencer et al. 2001, Evans and Leslie 2004, Tucker, Ghosh et al. 2009, Leslie, Gangelhoff et al. 2010, Ward, Bhardwaj et al. 2013, Ward, Sengupta et al. 2020). On the other hand, in zebrafish and mouse immature dendritic cells, cPLA$_2$α localizes exclusively in the nucleus,

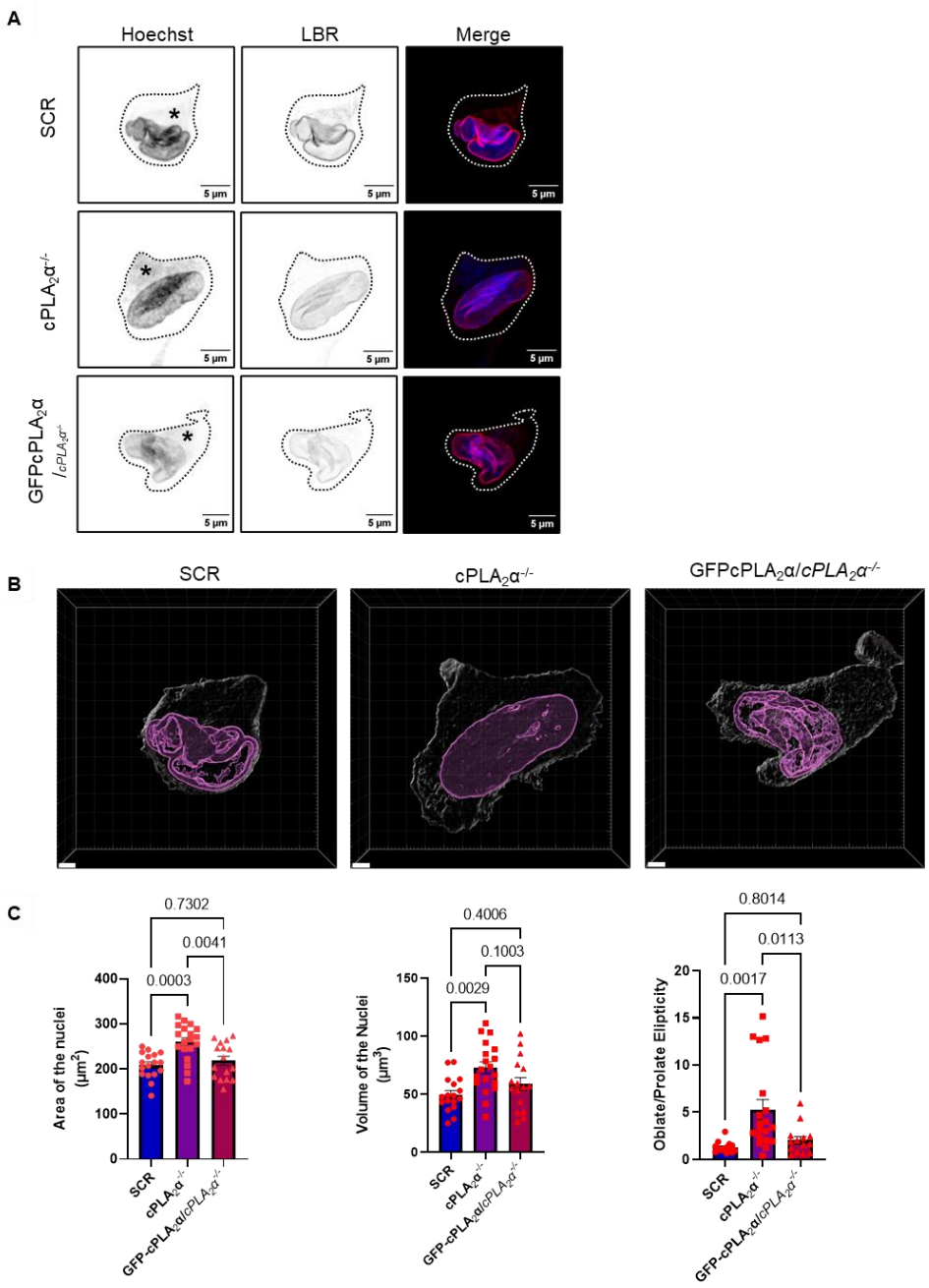

Figure 4.8: cPLA$_2$α regulates nuclear architecture.

A. Representative fluorescent images of differentiated SCR, *cPLA$_2$α$^{-/-}$*, and GFP-cPLA$_2$α/*cPLA$_2$α$^{-/-}$* cells chemotaxing towards 100nM fMLF, fixed, and stained with an antibody against LBR at 1:500 dilution in 2% goat serum in DPBS and Hoechst. *****non-specific Hoechst signal. **B.** Representative images of Imaris 3D renderings of nuclei using the LBR signal of SCR, *cPLA$_2$α$^{-/-}$* and GFP-cPLA$_2$α/*cPLA$_2$α$^{-/-}$* cells. Bar=2µm. **C.** Quantifications of nuclear area, volume, and 3D aspect ratio using Imaris surface renderings. Each dot represents individual nuclei from n=3 experiments. P values determined using ordinary one-way ANOVA are reported.

translocating to the inner nuclear envelope upon hypotonic stimulation (Enyedi, Jelcic et al. 2016, Lomakin, Cattin et al. 2020). Additionally, in rat peritoneal macrophages, cPLA$_2$α was primarily localized to the cytosol, with some staining in the nucleus (Peters-Golden and McNish 1993). While these differences in localization are potentially due to the requirement of cPLA$_2$α in other cellular functions, such as protein trafficking and maintaining lipid homeostasis, our findings also highlight that commercially available antibodies against cPLA$_2$α are potentially not suitable for IF studies.

Our findings show that cPLA$_2$α localizes to both the cytosol and the nucleus of human primary neutrophils and neutrophil-like cells (**Figure 4.3** and **Figure 4.5**). The LTB$_4$ signaling pathway is the predominant eicosanoid pathway in chemotaxing neutrophils, and LTB$_4$ secretion occurs within 1min after chemoattractant stimulation (Afonso, Janka-Junttila et al. 2012). AA release by cPLA$_2$α is the rate-limiting step in LTB$_4$ production. We hypothesize that the presence of cPLA$_2$α in the nucleus, where it can readily reach NE buds and the positive curvature of ILVs, is key in the ability of neutrophils to quickly generate and secrete LTB$_4$ upon chemoattractant stimulation. Furthermore, our findings showing that cPLA$_2$α is present on the outside of LTB$_4$-containing exosomes (**Figure 4.7**) suggest that LTB$_4$ is actively synthesized within exosomes to maintain a stable gradient and efficiently relay signals to distal neutrophils as they reach sites of inflammation or injury.

Studies from our lab have demonstrated that LTB$_4$-containing exosomes originate from ceramide-rich lipid microdomains on the NE (Arya, Chen et al. 2022). We found that cPLA$_2$α is not required for the biogenesis of LTB$_4$-containing exosomes (**Figure 4.6**). This is potentially due to the differences in curvature-inducing properties of cPLA$_2$α and ceramide. Ceramide, with its bulky fatty acid chains and small phosphate head group, induces negative curvature in the

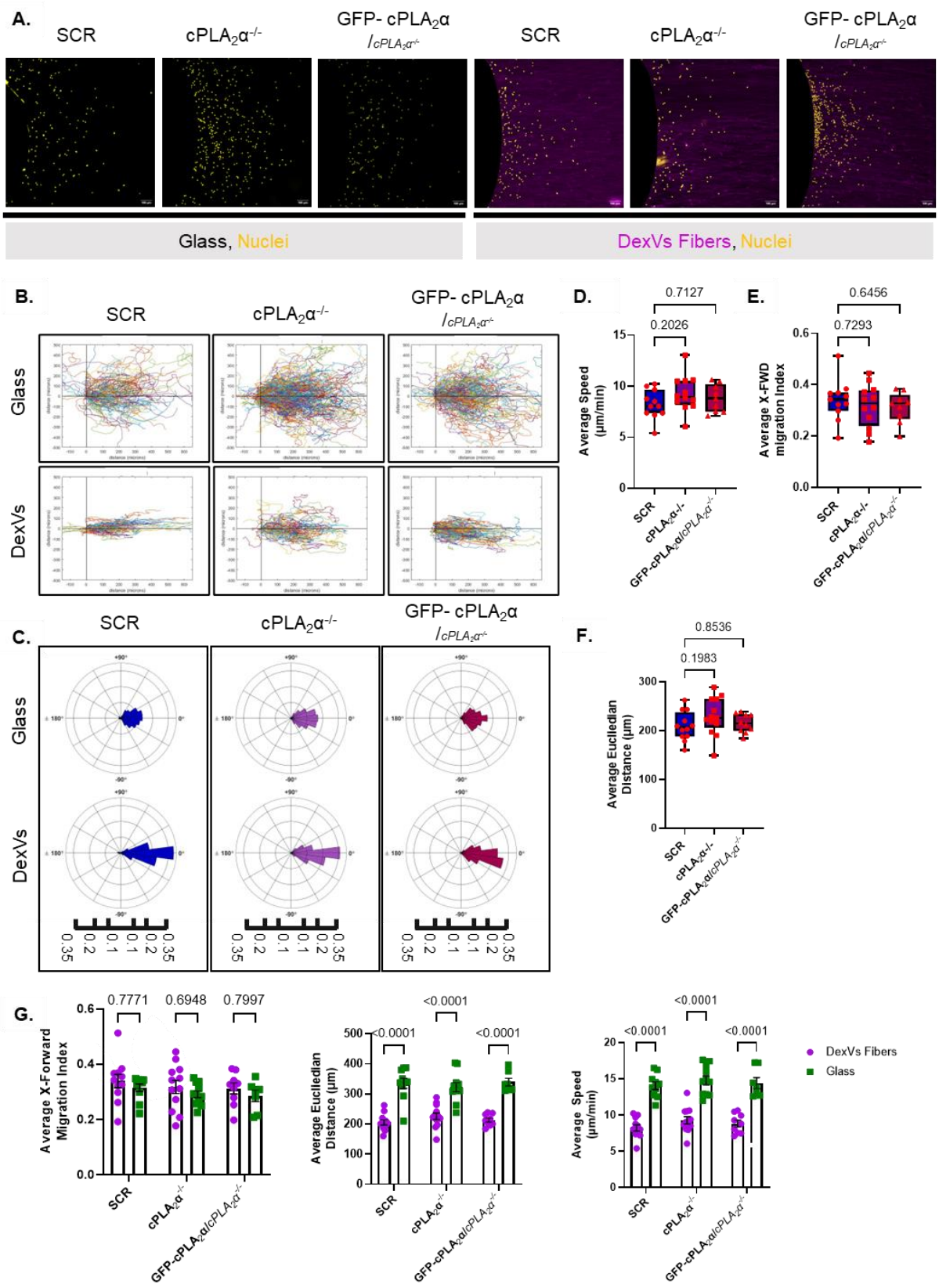
A.
SCR
cPLA2α-/-
GFP- cPLA2α /cPLA2α-/-
SCR
cPLA2α-/-
GFP- cPLA2α /cPLA2α-/-
Glass, Nuclei
DexVs Fibers, Nuclei
B.
SCR
cPLA2α-/-
GFP- cPLA2α /cPLA2α-/-
Glass
DexVs
C.
SCR
cPLA2α-/-
GFP- cPLA2α /cPLA2α-/-
Glass
DexVs
D.
0.7127
0.2026
Average Speed (µm/min)
SCR
cPLA2α-/-
GFP-cPLA2α/cPLA2α-/-
E.
0.6456
0.7293
Average X-FWD migration Index
SCR
cPLA2α-/-
GFP-cPLA2α/cPLA2α-/-
F.
0.8536
0.1983
Average Euclidian DIstance (µm)
SCR
cPLA2α-/-
GFP-cPLA2α/cPLA2α-/-
G.
0.7771
0.6948
0.7997
Average X-Forward Migration Index
SCR
cPLA2α-/-
GFP-cPLA2α/cPLA2α-/-
<0.0001
<0.0001
<0.0001
Average Euclidian DIstance (µm)
SCR
cPLA2α-/-
GFP-cPLA2α/cPLA2α-/-
<0.0001
<0.0001
<0.0001
Average Speed (µm/min)
SCR
cPLA2α-/-
GFP-cPLA2α/cPLA2α-/-
DexVs Fibers
Glass

Figure 4.9: *cPLA$_2\alpha^{-/-}$* cells can sense micro-topographies during chemotaxis.

A. Representative endpoint images of cells migrating under agarose towards 100nM fMLF on either glass or rhodamine labeled DexVs fiber mats. Scale bar 100µm. **B.** Plots showing representative tracks of individual cells migrating towards 100nM fMLF on either glass (top panel) or DexVs fiber mats (bottom panel). Each trace represents the migration path of a single cell. **C.** Matlab generated rose plots summarizing data from n=12 experiments showing the probability of cells moving in the direction of chemoattractant. (**D-F)** Graphs depicting average speed **(D)**, XFMI **(E),** and Euclidean distance **(F)** of cells migrating on DexVs fiber mats. Each dot represents the average of an experiment. One-way ANOVA test, using SCR as control, was used to test the statistical significance of the data. **G.** Plots showing average XFMI, Euclidean distance, and speed of SCR, *cPLA$_2\alpha^{-/-}$* and GFP-cPLA$_2\alpha$/*cPLA$_2\alpha^{-/-}$* cells migrating on either glass (purple) or DexVs fiber mats (green). Each dot represents the average of one experiment. A two-way ANOVA test was used to test the statistical significance of the data.

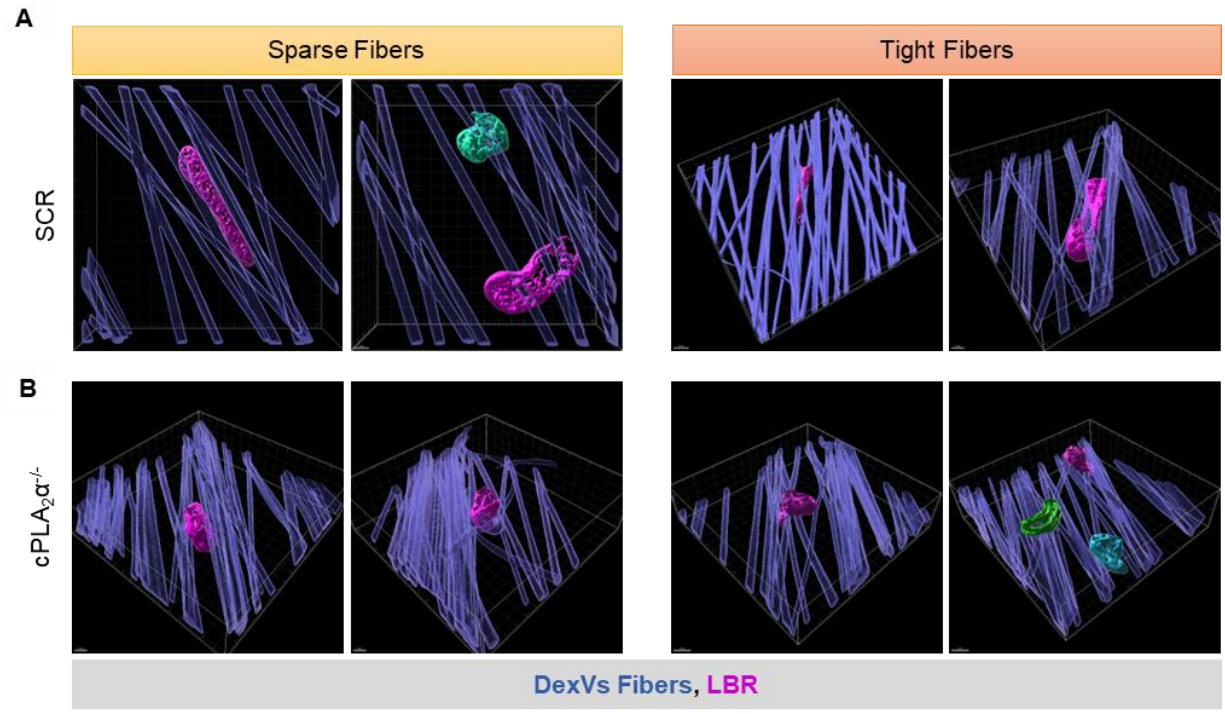

Figure 4.10: The nuclei of differentiated *cPLA$_2\alpha^{-/-}$* cells do not squeeze through tightly packed fiber mats.

Representative Imaris 3D renderings of nuclei and DexVs fibers were generated using the LBR (nuclei) and rhodamine red (fibers) signals in SCR **(A)** and *cPLA$_2\alpha^{-/-}$* **(B)** cells migrating under agarose on DexVs fiber mats towards 100nM fMLF—scale bar 2µm.

membrane due to the conical structure of ceramide. On the other hand, cPLA$_2\alpha$ activity results in the production of lysophospholipids with their bulky phosphate heady group and single fatty acid chain. This results in the generation of positive membrane curvature due to the inverted cone shape of the lysophospholipids (see chapter 1, **Figure 1.6**).

Our findings show that cPLA$_2\alpha$ regulates neutrophil nuclear morphology (**Figure 4.8**). The nucleus is the largest and most stiff organelle in the cell and has been shown to be involved in the ability of cells to sense their surrounding environment, which is mediated both by the nucleoskeleton and chromatin stiffness (Guilluy, Osborne et al. 2014, Kirby and Lammerding 2018, Ross and Stroud 2021). Neutrophils harbor distinct multilobed nuclei with little to no Lamin A/C expression at the NE, thereby enabling them to effectively squeeze through tight spaces (Saunders and Parent 2020). In contrast, the nuclei of HL-60 cells do not exhibit a multilobulated morphology, although they are irregularly shaped and have multiple folds (**Figure 4.8**). This difference in nuclear morphology could be due to the higher levels of Lamin A/C in HL-60 cells (Olins and Olins 2004). It is well established that increases in Lamin A/C expression increases nuclear stiffness (Lammerding, Schulze et al. 2004, Lammerding and Lee 2005). Additionally, it has been reported that increases in NE Lamin A/C levels decreases the translocation of cPLA$_2\alpha$ to the NE of zebrafish upon osmotic shock or confinement (Enyedi, Jelcic et al. 2016, Alraies, Rivera et al. 2022). We hypothesize that *cPLA$_2\alpha^{-/-}$* cells exhibit defects while migrating through constricted spaces due to stiffer nuclei caused by increased Lamin A/C levels. We performed pilot experiments to test this by measuring the levels of Lamin A/C in SCR and *cPLA$_2\alpha^{-/-}$* cells migrating towards 100nM fMLF and found no significant differences in the expression of Lamin A/C at the NE (**Figure 4.11**). While these findings suggest that changes in Lamin A/C are not observed in

cPLA$_2\alpha^{-/-}$ cells, the presence of Lamin A/C staining in the cytosol of these cells warrants further investigation.

cPLA$_2\alpha$ is a multifaceted protein with various cellular functions. In this study, we show that cPLA$_2\alpha$ mediates LTB$_4$ production and regulates nuclear morphology in chemotaxing neutrophil-like cells. Future studies are required to elucidate the mechanisms by which cPLA$_2\alpha$ induces nuclear stiffness and identify the various pathways activated by nuclear squeezing to facilitate neutrophil migration.

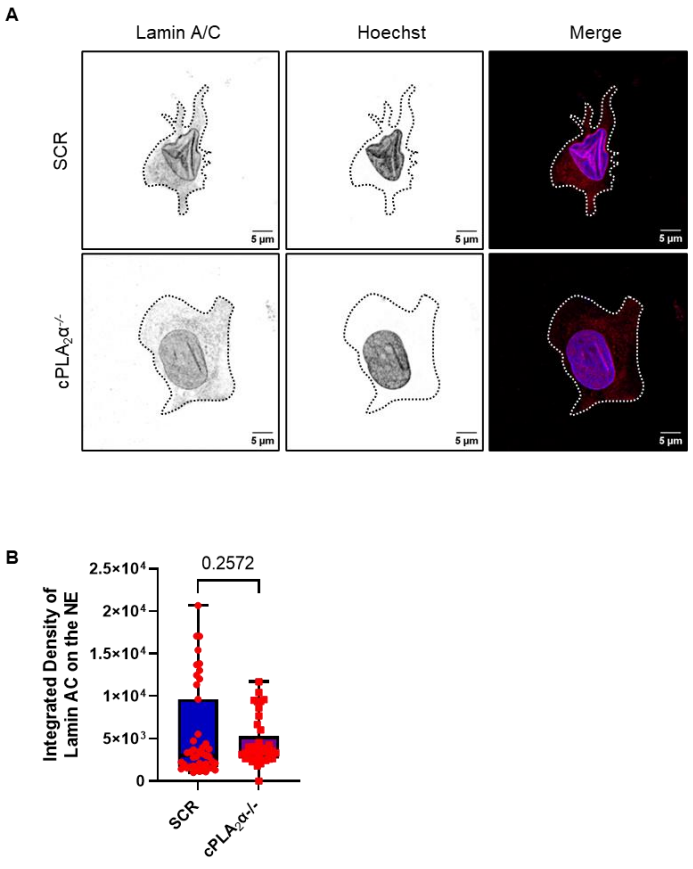

Figure 4.11: Lamin A/C levels in differentiated and chemotaxing SCR and *cPLA$_2\alpha^{-/-}$* cells.

A. Representative fluorescent images of differentiated SCR and *cPLA2$\alpha^{-/-}$* cells chemotaxing towards 100nM fMLF, fixed, and stained with an antibody against Lamin A/C at 1:200 dilution in 2% goat serum in DPBS and Hoechst. **B.** Graphs depicting the integrated density of Lamin A/C at the NE of SCR and *cPLA$_2\alpha^{-/-}$* cells migrating under agarose towards 100nM fMLF. Each dot represents nuclei from n=3 biological replicates. Mann-Whitney test was used to test the statistical significance of the data.

Chapter 5 Summary and Future Directions

5.1 Summary

5.1.1 Nuclear envelope budding is facilitated by ceramide-rich microdomains.

I started this dissertation by elucidating the mechanism by which LTB_4 is packaged and secreted from neutrophils in collaboration with Dr. Subhash Arya (Chapter 2). We showed that upon fMLF stimulation, neutrophils generate buds and multivesicular bodies (MVBs) emerging from the nuclear envelope (NE). The nuclear origin of these buds and MVBs was confirmed by the presence of lamin B receptor (LBR), an inner NE resident protein. Additionally, we showed that these buds and vesicles are positive for LTB_4 synthesizing enzymes such as 5LO, FLAP, and LTA_4H. We identified that the nuclear buds originate at ceramide-rich lipid microdomains through the activation of nSMase1, which converts sphingomyelin to ceramide. Additionally, using expansion microscopy, we demonstrated that the NE-derived buds and MVBs are distinct from canonical CD63-positive MVBs. Together, these findings identified a new mechanism where LTB_4-containing exosomes, which originate through a non-conventional path from the NE, allow the maintenance of stable LTB_4 gradients to recruit distal neutrophils. However, the mechanisms by which these non-conventional exosomes are sorted, trafficked, and secreted from neutrophils remain to be determined and are active areas of research in the Parent group.

5.1.2 cPLA$_2\alpha$ regulates neutrophil chemotaxis in a chemoattractant-dependent manner.

In Chapter 3 of this dissertation, I elucidated the impact of cPLA$_2$α inhibition and depletion on neutrophil migration. Using a cPLA$_2$α pharmacological inhibitor, Pyrrophenone, and genetic knock out (*cPLA$_2$α$^{-/-}$*) cell line, I found that inhibition or ablation of cPLA$_2$α improved the migration of human peripheral blood neutrophils or neutrophil-like cells toward fMLF. I next tested the migration phenotype of *cPLA$_2$α$^{-/-}$* towards different chemoattractants and found that *cPLA$_2$α$^{-/-}$* cells exhibited lower directionality toward C5a, LTB$_4$, and IL-8. The Parent group established that LTB$_4$ secretion is essential for the relay of chemotactic signals (Afonso, Janka-Junttila et al. 2012) and, as cPLA$_2$α is essential for LTB$_4$ production, we envision that the observed lower directionality towards C5a, LTB$_4$, and IL-8 is a consequence of the lack of signal relay. The absence of a phenotype in response to fMLF is related to the strong chemotactic activity of this chemoattractant. Indeed, it has been shown that signal relay is manifested at lower, more physiological concentrations of primary attractants like fMLF (Afonso, Janka-Junttila et al. 2012).

5.1.3 cPLA$_2$α regulates LTB$_4$ production and nuclear morphology

In Chapter 4, I explored the roles of cPLA$_2$α in neutrophil biology. First, I established that cPLA$_2$α localizes to three distinct regions in neutrophil-like cells: cytosol, nucleus, and the peri-nuclear region. Next, I demonstrated that while cPLA$_2$α is not required for the generation of the ceramide-rich lipid-ordered domains and release of exosomes, it is present within lipid microdomains and in exosomes of SCR and GFP-cPLA$_2$α/*cPLA$_2$α$^{-/-}$* cells and it is required for LTB$_4$ production. Additionally, I showed that exosomal cPLA$_2$α originates from the nuclear pool of cPLA$_2$α in neutrophil-like cells. Finally, I discovered that cPLA$_2$α regulates nuclear morphology in neutrophil-like cells and observed that nuclei of *cPLA$_2$α$^{-/-}$* cells could not squeeze through tight (<3μm) spaces. I hypothesize that these functions of cPLA$_2$α are potentially independent of one another as *cPLA$_2$α$^{-/-}$* cells can still form microdomains and generate exosomes while having

defected nuclei. We can test this hypothesis by generating a catalytically dead mutant of cPLA$_2\alpha$ (cPLA$_2\alpha$ S228A), expressing it in *cPLA$_2\alpha^{-/-}$* cells, and testing for the various functions of cPLA$_2\alpha$. **Figure 5.1** shows our current model of LTB$_4$ biosynthesis.

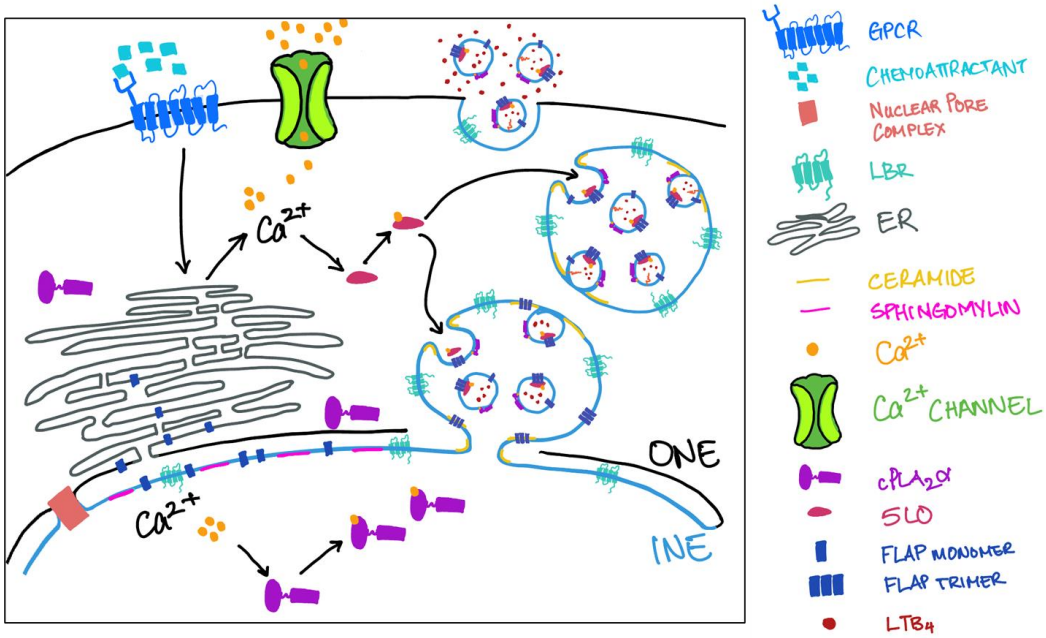

Figure 5.1 Cartoon illustrating the current model of LTB$_4$ generation and secretion in chemotaxing neutrophils (see text for details)

Considering the many other reported functions of cPLA$_2\alpha$ (Choukroun, Marshansky et al. 2000, Brown, Chambers et al. 2003, Ha, Clarke et al. 2012), it is conceivable that this multifaceted protein regulates many other neutrophil functions.

5.2 Future Directions

5.2.1 cPLA$_2\alpha$ function in receptor expression and trafficking

In Chapter 3, I demonstrated that *cPLA$_2\alpha^{-/-}$* cells show lower directionality when migrating towards C5a, LTB$_4$, and IL-8 but not fMLF. I hypothesized that this was due to defects in signal relay. However, these results could also be explained by (i) differences in downstream signaling

or (ii) diminished expression of cell surface receptors. The fact that we observed significant decreases in the chemotaxis index and the total distance covered by *cPLA$_2\alpha^{-/-}$* cells migrating towards C5a and LTB_4 suggests that these cells have defects in sensing the chemoattractant. Indeed, recent reports have suggested that cPLA$_2\alpha$ plays a role in amplifying cytokine and interleukin signaling-related genes in mouse immature dendritic cells and in mouse resident peritoneal macrophages (Suram, Silveira et al. 2013, Alraies, Rivera et al. 2022). Assessing the expression level of C5aR1 and BLT1/2, C5a, and LTB_4 receptors respectively, in chemotaxing cells would allow me to determine if chemoattractant sensing is involved in the lower directionality phenotype I observed. Unfortunately, antibodies against G-protein coupled receptors (GPCRs) are notoriously non-specific, possibly due to the complexity of the seven-pass transmembrane domains in GPCRs, and cannot be used for Western analysis or immunofluorescence studies. However, we can perform mRNA studies such as qPCR analysis and RNA sequencing to test the changes in the receptor expression levels and globally assess the role of cPLA$_2\alpha$ in gene regulation in activated neutrophils.

cPLA$_2\alpha$ has also been implicated in membrane trafficking (Brown, Chambers et al. 2003). It was shown to be involved in receptor recycling, the retrograde trafficking of itinerant membrane proteins, and the formation of bridges between the Golgi cisternae (Brown, Chambers et al. 2003, San Pietro, Capestrano et al. 2009). It is, therefore, possible that cPLA$_2\alpha$ is also involved in the trafficking of chemoattractant receptors to the plasma membrane. Studies from the Parent group established that various chemoattractant receptors endocytose and are trafficked differently when stimulated with saturating concentration of the chemoattractants (Subramanian, Moissoglu et al. 2018). They showed that FPR1 (receptor for fMLF) primarily goes through the recycling pathway, whereas C5aR1 (receptor for C5a) goes through the lysosomal degradation pathway

(Subramanian, Moissoglu et al. 2018). It is possible that the improved migration of *cPLA$_2$α$^{-/-}$* cells towards fMLF is due to a decrease in cPLA$_2$α mediated recycling of the FPR1 receptor, allowing for an increase in the FPR1 receptor at the plasma membrane. On the other hand, it is possible that depletion of cPLA$_2$α is promoting degradation of C5aR1, causing a decreased expression of receptors on the plasma membrane, leading to a decrease in migration towards C5a. We can test this hypothesis by utilizing the Alexa-Fluor 488 labeled fMLF and C5a to assess changes in endocytosis of ligand-bound receptor in SCR and *cPLA$_2$α$^{-/-}$* cells. Additionally, we can express FPR1-eGFP and C5aR1-eGFP in the *cPLA$_2$α$^{-/-}$* cells and study the trafficking of these receptors in activated neutrophils.

5.2.2 Interplay of ceramide kinase and cPLA$_2$α in LTB$_4$ biosynthesis

In Chapter 2 of this dissertation, I demonstrated that LTB$_4$-containing exosomes originate at ceramide-rich lipid microdomains at the NE and that the inhibition of ceramide generation leads to the attenuation of lipid microdomain formation and LTB$_4$ production. In Chapter 4, I demonstrated that although cPLA$_2$α is not required for the generation of the lipid microdomains, it is required for LTB$_4$ generation. Interestingly, structural analysis of cPLA$_2$α revealed that its C2 domain contains a small patch of basic residues that interact with ceramide 1-phosphate (C1-P), a bioactive sphingolipid metabolite (Pettus, Bielawska et al. 2004, Subramanian, Stahelin et al. 2005). This interaction induces a 10˚ shift in the position of cPLA$_2$α on membranes, locking it in position, bringing the catalytic site of cPLA$_2$α closer to its substrate and prolonging its residence on membranes (Subramanian, Stahelin et al. 2005, Ward, Bhardwaj et al. 2013). Additionally, this interaction is essential for the translocation of cPLA$_2$α from the cytosol to NE and peri-nuclear region in lung epithelial A549 cells (Ward, Bhardwaj et al. 2013). These data suggest that the presence of C1-P on membranes is essential for cPLA$_2$α activity.

Ceramide kinase (CERK) is the only protein known to be responsible for converting ceramides to C1-P (Gómez-Muñoz 2004). CERK was first discovered in brain synaptic vesicles and later found to be expressed in neutrophils and neutrophil-like cells (Kolesnick and Hemer 1990, Rincon, Rocha-Gregg et al. 2018). It was shown to translocate to the NE following stimulation with a calcium ionophore and has been implicated in maintaining neutrophil homeostasis as mice lacking CERK show a significant reduction in circulating neutrophils compared to WT mice (Pettus, Bielawska et al. 2003, Gomez-Munoz, Gangoiti et al. 2010). Additionally, it has been reported that CERK inhibition significantly reduces AA release in A549 cells (Pettus, Bielawska et al. 2003, Lamour, Stahelin et al. 2007). Based on these results, I hypothesize that the CERK-mediated conversion of ceramide to C1-P facilitates the translocation of cPLA$_2$α to the emerging intraluminal vesicles at the NE. This hypothesis can be tested by the generation and characterization of *CERK*$^{-/-}$ HL-60 cell line, followed by intracellular dynamic studies of GFP-cPLA$_2$α and mCherry-CERK in chemotaxing HL-60 cells.

In this dissertation, I have explored the multifaceted functions of cPLA$_2$α in chemotaxing neutrophil-like cells. I have demonstrated that LTB$_4$-containing exosomes originate from the ceramide-rich lipid-ordered microdomains at the NE and showed that cPLA$_2$α is not involved in this process. Additionally, I demonstrated that cPLA$_2$α regulates nuclear architecture and neutrophil chemotaxis in a chemoattractant-dependent manner. Further studies focused on elucidating the independence of these function will provide valuable insights into the various functions of cPLA$_2$α in chemotaxing neutrophils.

References

Afonso, P. V., M. Janka-Junttila, Y. J. Lee, C. P. McCann, C. M. Oliver, K. A. Aamer, W. Losert, M. T. Cicerone and C. A. Parent (2012). "LTB4 is a signal-relay molecule during neutrophil chemotaxis." Dev Cell **22**(5): 1079-1091.

Airola, M. V. and Y. A. Hannun (2013). "Sphingolipid metabolism and neutral sphingomyelinases." Handb Exp Pharmacol(215): 57-76.

Albi, E., R. Lazzarini and M. V. Magni (2003). "Reverse sphingomyelin-synthase in rat liver chromatin." FEBS Lett **549**(1-3): 152-156.

Alonso, F., P. M. Henson and C. C. Leslie (1986). "A cytosolic phospholipase in human neutrophils that hydrolyzes arachidonoyl-containing phosphatidylcholine." Biochim Biophys Acta **878**(2): 273-280.

Alraies, Z., C. A. Rivera, M.-G. Delgado, D. Sanséau, M. Maurin, A. Yatim, P. Saez, A. Williart, M. Gratia, N. S. De Silva, A. Moreau, B. Albaud, P. Legoix, H. Nakano, D. N. Cook, T. Lawrence, N. Manel, H. D. Moreau, G. P. F. Nader, M. Piel and A.-M. Lennon-Duménil (2022). "An Arp2/3-cPLA₂-NFκB axis acts as a Cell Shape Sensor to drive Homeostatic Migration of Dendritic Cells." bioRxiv: 2022.2008.2009.503223.

Arya, S. B., S. Chen, F. Jordan-Javed and C. A. Parent (2022). "Ceramide-rich microdomains facilitate nuclear envelope budding for non-conventional exosome formation." Nat Cell Biol **24**(7): 1019-1028.

Bäck, M., S.-E. Dahlén, J. M. Drazen, J. F. Evans, C. N. Serhan, T. Shimizu, T. Yokomizo and G. E. Rovati (2011). "International Union of Basic and Clinical Pharmacology. LXXXIV: Leukotriene Receptor Nomenclature, Distribution, and Pathophysiological Functions." Pharmacological Reviews **63**(3): 539-584.

Bonventre, J. V., Z. Huang, M. R. Taheri, E. O'Leary, E. Li, M. A. Moskowitz and A. Sapirstein (1997). "Reduced fertility and postischaemic brain injury in mice deficient in cytosolic phospholipase A2." Nature **390**(6660): 622-625.

Brown, W. J., K. Chambers and A. Doody (2003). "Phospholipase A2 (PLA2) enzymes in membrane trafficking: mediators of membrane shape and function." Traffic **4**(4): 214-221.

Burke, J. E. and E. A. Dennis (2009). "Phospholipase A(2) structure/function, mechanism, and signaling." Journal of Lipid Research **50**(Suppl): S237-S242.

Burn, G. L., A. Foti, G. Marsman, D. F. Patel and A. Zychlinsky (2021). "The Neutrophil." Immunity **54**(7): 1377-1391.

Casas, J., M. Valdearcos, J. Pindado, J. Balsinde and M. A. Balboa (2010). "The cationic cluster of group IVA phospholipase A₂ (Lys⁴⁸⁸/Lys⁵⁴¹/Lys⁵⁴³/Lys⁵⁴⁴) is involved in translocation of the enzyme to phagosomes in human macrophages." Journal of Lipid Research **51**(2): 388-399.

Cascianelli, G., M. Villani, M. Tosti, F. Marini, E. Bartoccini, M. V. Magni and E. Albi (2008). "Lipid microdomains in cell nucleus." Mol Biol Cell **19**(12): 5289-5295.

Channon, J. Y. and C. C. Leslie (1990). "A calcium-dependent mechanism for associating a soluble arachidonoyl-hydrolyzing phospholipase A2 with membrane in the macrophage cell line RAW 264.7." J Biol Chem **265**(10): 5409-5413.
Cho, W. and R. V. Stahelin (2005). "Membrane-protein interactions in cell signaling and membrane trafficking." Annu Rev Biophys Biomol Struct **34**: 119-151.
Choukroun, G. J., V. Marshansky, C. E. Gustafson, M. McKee, R. J. Hajjar, A. Rosenzweig, D. Brown and J. V. Bonventre (2000). "Cytosolic phospholipase A(2) regulates golgi structure and modulates intracellular trafficking of membrane proteins." J Clin Invest **106**(8): 983-993.
Clark, J. D., L. L. Lin, R. W. Kriz, C. S. Ramesha, L. A. Sultzman, A. Y. Lin, N. Milona and J. L. Knopf (1991). "A novel arachidonic acid-selective cytosolic PLA2 contains a Ca(2+)-dependent translocation domain with homology to PKC and GAP." Cell **65**(6): 1043-1051.
Conti, C. J. and A. J. Klein-Szanto (1973). "Nuclear multivesicular bodies in cultured hamster cells." Experientia **29**(7): 850-851.
Cryer, B. (2001). "Mucosal defense and repair. Role of prostaglandins in the stomach and duodenum." Gastroenterol Clin North Am **30**(4): 877-894, v-vi.
Cvjetkovic, A., S. C. Jang, B. Konečná, J. L. Höög, C. Sihlbom, C. Lässer and J. Lötvall (2016). "Detailed Analysis of Protein Topology of Extracellular Vesicles-Evidence of Unconventional Membrane Protein Orientation." Sci Rep **6**: 36338.
Dana, R., T. L. Leto, H. L. Malech and R. Levy (1998). "Essential requirement of cytosolic phospholipase A2 for activation of the phagocyte NADPH oxidase." J Biol Chem **273**(1): 441-445.
Dasgupta, R., M. S. Miettinen, N. Fricke, R. Lipowsky and R. Dimova (2018). "The glycolipid GM1 reshapes asymmetric biomembranes and giant vesicles by curvature generation." Proc Natl Acad Sci U S A **115**(22): 5756-5761.
Dennis, E. A., J. Cao, Y. H. Hsu, V. Magrioti and G. Kokotos (2011). "Phospholipase A2 enzymes: physical structure, biological function, disease implication, chemical inhibition, and therapeutic intervention." Chem Rev **111**(10): 6130-6185.
Dennis, E. A. and P. C. Norris (2015). "Eicosanoid storm in infection and inflammation." Nat Rev Immunol **15**(8): 511-523.
Dessen, A., J. Tang, H. Schmidt, M. Stahl, J. D. Clark, J. Seehra and W. S. Somers (1999). "Crystal structure of human cytosolic phospholipase A2 reveals a novel topology and catalytic mechanism." Cell **97**(3): 349-360.
Drexler, H. G., W. G. Dirks, Y. Matsuo and R. A. MacLeod (2003). "False leukemia-lymphoma cell lines: an update on over 500 cell lines." Leukemia **17**(2): 416-426.
Eich, C., C. Manzo, S. de Keijzer, G. J. Bakker, I. Reinieren-Beeren, M. F. García-Parajo and A. Cambi (2016). "Changes in membrane sphingolipid composition modulate dynamics and adhesion of integrin nanoclusters." Sci Rep **6**: 20693.
Elsherbini, A. and E. Bieberich (2018). "Ceramide and Exosomes: A Novel Target in Cancer Biology and Therapy." Adv Cancer Res **140**: 121-154.
Enyedi, B., M. Jelcic and P. Niethammer (2016). "The Cell Nucleus Serves as a Mechanotransducer of Tissue Damage-Induced Inflammation." Cell **165**(5): 1160-1170.
Esser, J., U. Gehrmann, F. L. D'Alexandri, A. M. Hidalgo-Estévez, C. E. Wheelock, A. Scheynius, S. Gabrielsson and O. Rådmark (2010). "Exosomes from human macrophages and dendritic cells contain enzymes for leukotriene biosynthesis and promote granulocyte migration." J Allergy Clin Immunol **126**(5): 1032-1040, 1040.e1031-1034.

Evans, J. H. and C. C. Leslie (2004). "The cytosolic phospholipase A2 catalytic domain modulates association and residence time at Golgi membranes." J Biol Chem **279**(7): 6005-6016.
Evans, J. H., D. M. Spencer, A. Zweifach and C. C. Leslie (2001). "Intracellular calcium signals regulating cytosolic phospholipase A2 translocation to internal membranes." J Biol Chem **276**(32): 30150-30160.
Fan, F., Y. Muroya and R. J. Roman (2015). "Cytochrome P450 eicosanoids in hypertension and renal disease." Curr Opin Nephrol Hypertens **24**(1): 37-46.
Fanning, L. B. and J. A. Boyce (2013). "Lipid mediators and allergic diseases." Ann Allergy Asthma Immunol **111**(3): 155-162.
Ferguson, A. D., B. M. McKeever, S. Xu, D. Wisniewski, D. K. Miller, T. T. Yamin, R. H. Spencer, L. Chu, F. Ujjainwalla, B. R. Cunningham, J. F. Evans and J. W. Becker (2007). "Crystal structure of inhibitor-bound human 5-lipoxygenase-activating protein." Science **317**(5837): 510-512.
Flamand, N., S. Picard, L. Lemieux, M. Pouliot, S. G. Bourgoin and P. Borgeat (2006). "Effects of pyrrophenone, an inhibitor of group IVA phospholipase A2, on eicosanoid and PAF biosynthesis in human neutrophils." Br J Pharmacol **149**(4): 385-392.
Fleming, I. (2001). "Cytochrome p450 and vascular homeostasis." Circ Res **89**(9): 753-762.
Frazier, A. A., M. A. Wisner, N. J. Malmberg, K. G. Victor, G. E. Fanucci, E. A. Nalefski, J. J. Falke and D. S. Cafiso (2002). "Membrane orientation and position of the C2 domain from cPLA2 by site-directed spin labeling." Biochemistry **41**(20): 6282-6292.
Gambarotto, D., F. U. Zwettler, M. Le Guennec, M. Schmidt-Cernohorska, D. Fortun, S. Borgers, J. Heine, J. G. Schloetel, M. Reuss, M. Unser, E. S. Boyden, M. Sauer, V. Hamel and P. Guichard (2019). "Imaging cellular ultrastructures using expansion microscopy (U-ExM)." Nat Methods **16**(1): 71-74.
Gijón, M. A. and C. C. Leslie (1999). "Regulation of arachidonic acid release and cytosolic phospholipase A2 activation." J Leukoc Biol **65**(3): 330-336.
Gijón, M. A., D. M. Spencer, A. L. Kaiser and C. C. Leslie (1999). "Role of Phosphorylation Sites and the C2 Domain in Regulation of Cytosolic Phospholipase A(2)." J Cell Biol **145**(6): 1219-1232.
Gijon, M. A., D. M. Spencer, A. R. Siddiqi, J. V. Bonventre and C. C. Leslie (2000). "Cytosolic phospholipase A2 is required for macrophage arachidonic acid release by agonists that Do and Do not mobilize calcium. Novel role of mitogen-activated protein kinase pathways in cytosolic phospholipase A2 regulation." J Biol Chem **275**(26): 20146-20156.
Gómez-Muñoz, A. (2004). "Ceramide-1-phosphate: a novel regulator of cell activation." FEBS Lett **562**(1-3): 5-10.
Gomez-Munoz, A., P. Gangoiti, M. H. Granado, L. Arana and A. Ouro (2010). "Ceramide-1-Phosphate in Cell Survival and Inflammatory Signaling." Sphingolipids as Signaling and Regulatory Molecules **688**: 118-130.
Guilluy, C., L. D. Osborne, L. Van Landeghem, L. Sharek, R. Superfine, R. Garcia-Mata and K. Burridge (2014). "Isolated nuclei adapt to force and reveal a mechanotransduction pathway in the nucleus." Nature Cell Biology **16**: 376.
Guo, B. B., S. A. Bellingham and A. F. Hill (2015). "The neutral sphingomyelinase pathway regulates packaging of the prion protein into exosomes." J Biol Chem **290**(6): 3455-3467.
Ha, K. D., B. A. Clarke and W. J. Brown (2012). "Regulation of the Golgi complex by phospholipid remodeling enzymes." Biochimica et Biophysica Acta (BBA) - Molecular and Cell Biology of Lipids **1821**(8): 1078-1088.

Haas, E. and D. W. Stanley (2007). Phospholipases. xPharm: The Comprehensive Pharmacology Reference. S. J. Enna and D. B. Bylund. New York, Elsevier**:** 1-3.
Haeggström, J. Z. and A. Wetterholm (2010). Chapter 151 - Leukotriene Mediators. Handbook of Cell Signaling (Second Edition). R. A. Bradshaw and E. A. Dennis. San Diego, Academic Press**:** 1229-1234.
Hanna, V. S. and E. A. A. Hafez (2018). "Synopsis of arachidonic acid metabolism: A review." J Adv Res **11**: 23-32.
Has, C., P. Sivadas and S. L. Das (2022). "Insights into Membrane Curvature Sensing and Membrane Remodeling by Intrinsically Disordered Proteins and Protein Regions." J Membr Biol **255**(2-3): 237-259.
Hefner, Y., A. G. Borsch-Haubold, M. Murakami, J. I. Wilde, S. Pasquet, D. Schieltz, F. Ghomashchi, J. R. Yates, 3rd, C. G. Armstrong, A. Paterson, P. Cohen, R. Fukunaga, T. Hunter, I. Kudo, S. P. Watson and M. H. Gelb (2000). "Serine 727 phosphorylation and activation of cytosolic phospholipase A2 by MNK1-related protein kinases." J Biol Chem **275**(48): 37542-37551.
Higham, A., P. Cadden, T. Southworth, M. Rossall, U. Kolsum, S. Lea, R. Knowles and D. Singh (2016). "Leukotriene B4 levels in sputum from asthma patients." ERJ Open Res **2**(4).
Huff, J., A. Bergter, J. Birkenbeil, I. Kleppe, R. Engelmann and U. Krzic (2017). The new 2D Superresolution mode for ZEISS Airyscan, Nature Publishing Group UK London.
Hurley, B. P., W. Pirzai, K. L. Mumy, K. Gronert and B. A. McCormick (2011). "Selective eicosanoid-generating capacity of cytoplasmic phospholipase A2 in Pseudomonas aeruginosa-infected epithelial cells." Am J Physiol Lung Cell Mol Physiol **300**(2): L286-294.
Izzo, A. A. and D. G. Deutsch (2011). "Unique pathway for anandamide synthesis and liver regeneration." Proc Natl Acad Sci U S A **108**(16): 6339-6340.
Jayadev, S., H. L. Hayter, N. Andrieu, C. J. Gamard, B. Liu, R. Balu, M. Hayakawa, F. Ito and Y. A. Hannun (1997). "Phospholipase A2 is necessary for tumor necrosis factor alpha-induced ceramide generation in L929 cells." J Biol Chem **272**(27): 17196-17203.
Kabbani, A. M., K. Raghunathan, W. I. Lencer, A. K. Kenworthy and C. V. Kelly (2020). "Structured clustering of the glycosphingolipid GM1 is required for membrane curvature induced by cholera toxin." Proc Natl Acad Sci U S A **117**(26): 14978-14986.
Kilarski, W. and A. Jasiński (1970). "The formation of multivesicular bodies from the nuclear envelope." J Cell Biol **45**(2): 205-211.
Kirby, T. J. and J. Lammerding (2018). "Emerging views of the nucleus as a cellular mechanosensor." Nature Cell Biology **20**(4): 373-381.
Kolaczkowska, E. and P. Kubes (2013). "Neutrophil recruitment and function in health and inflammation." Nat Rev Immunol **13**(3): 159-175.
Kolesnick, R. (2002). "The therapeutic potential of modulating the ceramide/sphingomyelin pathway." J Clin Invest **110**(1): 3-8.
Kolesnick, R. N. and M. R. Hemer (1990). "Characterization of a ceramide kinase activity from human leukemia (HL-60) cells. Separation from diacylglycerol kinase activity." J Biol Chem **265**(31): 18803-18808.
Kramer, R. M., G. C. Checani, A. Deykin, C. R. Pritzker and D. Deykin (1986). "Solubilization and properties of Ca2+-dependent human platelet phospholipase A2." Biochim Biophys Acta **878**(3): 394-403.
Kremserova, S. and W. M. Nauseef (2020). "Isolation of Human Neutrophils from Venous Blood." Methods Mol Biol **2087**: 33-42.

Lammerding, J. and R. T. Lee (2005). "The nuclear membrane and mechanotransduction: impaired nuclear mechanics and mechanotransduction in lamin A/C deficient cells." Novartis Found Symp **264**: 264-273; discussion 273-268.
Lammerding, J., P. C. Schulze, T. Takahashi, S. Kozlov, T. Sullivan, R. D. Kamm, C. L. Stewart and R. T. Lee (2004). "Lamin A/C deficiency causes defective nuclear mechanics and mechanotransduction." J Clin Invest **113**(3): 370-378.
Lammermann, T., P. V. Afonso, B. R. Angermann, J. M. Wang, W. Kastenmuller, C. A. Parent and R. N. Germain (2013). "Neutrophil swarms require LTB4 and integrins at sites of cell death in vivo." Nature **498**(7454): 371-375.
Lamour, N. F., R. V. Stahelin, D. S. Wijesinghe, M. Maceyka, E. Wang, J. C. Allegood, A. H. Merrill, Jr., W. Cho and C. E. Chalfant (2007). "Ceramide kinase uses ceramide provided by ceramide transport protein: localization to organelles of eicosanoid synthesis." J Lipid Res **48**(6): 1293-1304.
Larios, J., V. Mercier, A. Roux and J. Gruenberg (2020). "ALIX- and ESCRT-III-dependent sorting of tetraspanins to exosomes." J Cell Biol **219**(3).
Leslie, C. C. (2004). "Regulation of the specific release of arachidonic acid by cytosolic phospholipase A2." Prostaglandins Leukot Essent Fatty Acids **70**(4): 373-376.
Leslie, C. C. (2015). "Cytosolic phospholipase A(2): physiological function and role in disease." J Lipid Res **56**(8): 1386-1402.
Leslie, C. C., T. A. Gangelhoff and M. H. Gelb (2010). "Localization and function of cytosolic phospholipase A2alpha at the Golgi." Biochimie **92**(6): 620-626.
Leslie, C. C., D. R. Voelker, J. Y. Channon, M. M. Wall and P. T. Zelarney (1988). "Properties and purification of an arachidonoyl-hydrolyzing phospholipase A2 from a macrophage cell line, RAW 264.7." Biochim Biophys Acta **963**(3): 476-492.
Levy, R. (2006). "The role of cytosolic phospholipase A2-alfa in regulation of phagocytic functions." Biochimica et Biophysica Acta (BBA) - Molecular and Cell Biology of Lipids **1761**(11): 1323-1334.
Levy, R., R. Dana, I. Hazan, I. Levy, G. Weber, R. Smoliakov, I. Pesach, K. Riesenberg and F. Schlaeffer (2000). "Elevated cytosolic phospholipase A(2) expression and activity in human neutrophils during sepsis." Blood **95**(2): 660-665.
Lin, L. L., M. Wartmann, A. Y. Lin, J. L. Knopf, A. Seth and R. J. Davis (1993). "cPLA2 is phosphorylated and activated by MAP kinase." Cell **72**(2): 269-278.
Linkous, A. and E. Yazlovitskaya (2010). "Cytosolic phospholipase A2 as a mediator of disease pathogenesis." Cell Microbiol **12**(10): 1369-1377.
Linkous, A. G., E. M. Yazlovitskaya and D. E. Hallahan (2010). "Cytosolic Phospholipase A2 and Lysophospholipids in Tumor Angiogenesis." JNCI: Journal of the National Cancer Institute **102**(18): 1398-1412.
Lo, C. M., H. B. Wang, M. Dembo and Y. L. Wang (2000). "Cell movement is guided by the rigidity of the substrate." Biophys J **79**(1): 144-152.
Loesel, K. E., H. L. Hiraki, B. M. Baker and C. A. Parent (2023). "An adaptive and versatile method to quantitate and characterize collective cell migration behaviors on complex surfaces." Frontiers in Cell and Developmental Biology **11**.
Lomakin, A. J., C. J. Cattin, D. Cuvelier, Z. Alraies, M. Molina, G. P. F. Nader, N. Srivastava, P. J. Sáez, J. M. Garcia-Arcos, I. Y. Zhitnyak, A. Bhargava, M. K. Driscoll, E. S. Welf, R. Fiolka, R. J. Petrie, N. S. De Silva, J. M. González-Granado, N. Manel, A. M. Lennon-Duménil, D. J.

Müller and M. Piel (2020). "The nucleus acts as a ruler tailoring cell responses to spatial constraints." Science **370**(6514): eaba2894.
Luberto, C., D. F. Hassler, P. Signorelli, Y. Okamoto, H. Sawai, E. Boros, D. J. Hazen-Martin, L. M. Obeid, Y. A. Hannun and G. K. Smith (2002). "Inhibition of tumor necrosis factor-induced cell death in MCF7 by a novel inhibitor of neutral sphingomyelinase." J Biol Chem **277**(43): 41128-41139.
Lucki, N. C. and M. B. Sewer (2012). "Nuclear sphingolipid metabolism." Annu Rev Physiol **74**: 131-151.
MacKnight, H. P., D. J. Stephenson, L. A. Hoeferlin, S. D. Benusa, J. T. DeLigio, K. D. Maus, A. N. Ali, J. S. Wayne, M. A. Park, E. H. Hinchcliffe, R. E. Brown, J. J. Ryan, R. F. Diegelmann and C. E. Chalfant (2019). "The interaction of ceramide 1-phosphate with group IVA cytosolic phospholipase A(2) coordinates acute wound healing and repair." Sci Signal **12**(610).
Magee, A. I. and I. Parmryd (2003). "Detergent-resistant membranes and the protein composition of lipid rafts." Genome Biol **4**(11): 234.
Majumdar, R., M. Sixt and C. A. Parent (2014). "New paradigms in the establishment and maintenance of gradients during directed cell migration." Curr Opin Cell Biol **30**: 33-40.
Majumdar, R., A. Tavakoli Tameh, S. B. Arya and C. A. Parent (2021). "Exosomes mediate LTB4 release during neutrophil chemotaxis." PLoS Biol **19**(7): e3001271.
Mandal, A. K., P. B. Jones, A. M. Bair, P. Christmas, D. Miller, T. T. Yamin, D. Wisniewski, J. Menke, J. F. Evans, B. T. Hyman, B. Bacskai, M. Chen, D. M. Lee, B. Nikolic and R. J. Soberman (2008). "The nuclear membrane organization of leukotriene synthesis." Proc Natl Acad Sci U S A **105**(51): 20434-20439.
Manley, H. R., M. C. Keightley and G. J. Lieschke (2018). "The Neutrophil Nucleus: An Important Influence on Neutrophil Migration and Function." Front Immunol **9**: 2867.
Matsui, T., F. Osaki, S. Hiragi, Y. Sakamaki and M. Fukuda (2021). "ALIX and ceramide differentially control polarized small extracellular vesicle release from epithelial cells." EMBO Rep **22**(5): e51475.
McCullough, J., R. D. Fisher, F. G. Whitby, W. I. Sundquist and C. P. Hill (2008). "ALIX-CHMP4 interactions in the human ESCRT pathway." Proc Natl Acad Sci U S A **105**(22): 7687-7691.
McMahon, H. T. and E. Boucrot (2015). "Membrane curvature at a glance." J Cell Sci **128**(6): 1065-1070.
Meyer, A. M., L. D. Dwyer-Nield, G. J. Hurteau, R. L. Keith, E. O'Leary, M. You, J. V. Bonventre, R. A. Nemenoff and A. M. Malkinson (2004). "Decreased lung tumorigenesis in mice genetically deficient in cytosolic phospholipase A2." Carcinogenesis **25**(8): 1517-1524.
Miyabe, Y., C. Miyabe, V. Mani, T. R. Mempel and A. D. Luster (2019). "Atypical complement receptor C5aR2 transports C5a to initiate neutrophil adhesion and inflammation." Sci Immunol **4**(35).
Mizutani, Y., K. Tamiya-Koizumi, N. Nakamura, M. Kobayashi, Y. Hirabayashi and S. Yoshida (2001). "Nuclear localization of neutral sphingomyelinase 1: biochemical and immunocytochemical analyses." J Cell Sci **114**(Pt 20): 3727-3736.
Moltu, K., E. Bjørgo, T. Solstad, T. Berge, B. Thiede and K. Taskén (2013). "A proteomic approach to screening of dynamic changes in detergent-resistant membranes from activated human primary T cells." Journal of Proteomics and Bioinformatics **6**: 72-80.

Nagase, T., N. Uozumi, S. Ishii, K. Kume, T. Izumi, Y. Ouchi and T. Shimizu (2000). "Acute lung injury by sepsis and acid aspiration: a key role for cytosolic phospholipase A2." Nat Immunol **1**(1): 42-46.
Nalefski, E. A., T. McDonagh, W. Somers, J. Seehra, J. J. Falke and J. D. Clark (1998). "Independent folding and ligand specificity of the C2 calcium-dependent lipid binding domain of cytosolic phospholipase A2." J Biol Chem **273**(3): 1365-1372.
Nalefski, E. A., M. M. Slazas and J. J. Falke (1997). "Ca2+-signaling cycle of a membrane-docking C2 domain." Biochemistry **36**(40): 12011-12018.
Nebert, D. W. and T. P. Dalton (2006). "The role of cytochrome P450 enzymes in endogenous signalling pathways and environmental carcinogenesis." Nat Rev Cancer **6**(12): 947-960.
Nemenoff, R. A., S. Winitz, N. X. Qian, V. Van Putten, G. L. Johnson and L. E. Heasley (1993). "Phosphorylation and activation of a high molecular weight form of phospholipase A2 by p42 microtubule-associated protein 2 kinase and protein kinase C." J Biol Chem **268**(3): 1960-1964.
Neuber, K., R. A. Hilger and W. König (1991). "Interleukin-3, interleukin-8, FMLP and C5a enhance the release of leukotrienes from neutrophils of patients with atopic dermatitis." Immunology **73**(1): 83-87.
Nijenhuis, W., H. G. J. Damstra, E. J. van Grinsven, M. K. Iwanski, P. Praest, Z. E. Soltani, M. M. P. van Grinsven, J. E. Brunsveld, T. de Kort, L. W. Rodenburg, D. C. M. de Jong, H. H. M. Raeven, S. Spelier, G. D. Amatngalim, A. Akhmanova, M. Nijhuis, R. J. Lebbink, J. M. Beekman and L. C. Kapitein (2021). "Optical nanoscopy reveals SARS-CoV-2-induced remodeling of human airway cells." bioRxiv: 2021.2008.2005.455126.
Oikawa, Y., E. Yamato, F. Tashiro, M. Yamamoto, N. Uozumi, A. Shimada, T. Shimizu and J. Miyazaki (2005). "Protective role for cytosolic phospholipase A2alpha in autoimmune diabetes of mice." FEBS Lett **579**(18): 3975-3978.
Olins, A. L. and D. E. Olins (2004). "Cytoskeletal influences on nuclear shape in granulocytic HL-60 cells." BMC Cell Biol **5**: 30.
Owen, D. M., C. Rentero, A. Magenau, A. Abu-Siniyeh and K. Gaus (2011). "Quantitative imaging of membrane lipid order in cells and organisms." Nat Protoc **7**(1): 24-35.
Oyoshi, M. K., R. He, Y. Li, S. Mondal, J. Yoon, R. Afshar, M. Chen, D. M. Lee, H. R. Luo, A. D. Luster, J. S. Cho, L. S. Miller, A. Larson, G. F. Murphy and R. S. Geha (2012). "Leukotriene B4-driven neutrophil recruitment to the skin is essential for allergic skin inflammation." Immunity **37**(4): 747-758.
P Needleman, J Truk, B A Jakschik, a. A R Morrison and J. B. Lefkowith (1986). "Arachidonic Acid Metabolism." Annual Review of Biochemistry **55**(1): 69-102.
Peeters, B. W. A., A. C. A. Piët and M. Fornerod (2022). "Generating Membrane Curvature at the Nuclear Pore: A Lipid Point of View." Cells **11**(3).
Persaud-Sawin, D. A., S. Lightcap and G. J. Harry (2009). "Isolation of rafts from mouse brain tissue by a detergent-free method." J Lipid Res **50**(4): 759-767.
Peters-Golden, M. (1998). "Cell biology of the 5-lipoxygenase pathway." Am J Respir Crit Care Med **157**(6 Pt 2): S227-231; discussion S231-222, S247-228.
Peters-Golden, M. (1998). "Molecular mechanisms of leukotriene synthesis: the changing paradigm." Clin Exp Allergy **28**(9): 1059-1065.
Peters-Golden, M. and R. W. McNish (1993). "Redistribution of 5-lipoxygenase and cytosolic phospholipase A2 to the nuclear fraction upon macrophage activation." Biochem Biophys Res Commun **196**(1): 147-153.

Peters-Golden, M., K. Song, T. Marshall and T. Brock (1996). "Translocation of cytosolic phospholipase A2 to the nuclear envelope elicits topographically localized phospholipid hydrolysis." Biochem J **318 (Pt 3)**(Pt 3): 797-803.
Pettus, B. J., A. Bielawska, S. Spiegel, P. Roddy, Y. A. Hannun and C. E. Chalfant (2003). "Ceramide kinase mediates cytokine- and calcium ionophore-induced arachidonic acid release." J Biol Chem **278**(40): 38206-38213.
Pettus, B. J., A. Bielawska, P. Subramanian, D. S. Wijesinghe, M. Maceyka, C. C. Leslie, J. H. Evans, J. Freiberg, P. Roddy, Y. A. Hannun and C. E. Chalfant (2004). "Ceramide 1-Phosphate Is a Direct Activator of Cytosolic Phospholipase A₂*." Journal of Biological Chemistry **279**(12): 11320-11326.
Piomelli, D. (2013). Endocannabinoids. Encyclopedia of Biological Chemistry (Second Edition). W. J. Lennarz and M. D. Lane. Waltham, Academic Press**:** 194-196.
Rens, E. G. and R. M. H. Merks (2020). "Cell Shape and Durotaxis Explained from Cell-Extracellular Matrix Forces and Focal Adhesion Dynamics." iScience **23**(9): 101488.
Rincon, E., B. L. Rocha-Gregg and S. R. Collins (2018). "A map of gene expression in neutrophil-like cell lines." BMC Genomics **19**(1): 573.
Ross, J. A. and M. J. Stroud (2021). "THE NUCLEUS: Mechanosensing in cardiac disease." The International Journal of Biochemistry & Cell Biology **137**: 106035.
Rowat, A. C., D. E. Jaalouk, M. Zwerger, W. L. Ung, I. A. Eydelnant, D. E. Olins, A. L. Olins, H. Herrmann, D. A. Weitz and J. Lammerding (2013). "Nuclear envelope composition determines the ability of neutrophil-type cells to passage through micron-scale constrictions." J Biol Chem **288**(12): 8610-8618.
Sadik, C. D. and A. D. Luster (2012). "Lipid-cytokine-chemokine cascades orchestrate leukocyte recruitment in inflammation." J Leukoc Biol **91**(2): 207-215.
Samuelsson, B. (1983). "Leukotrienes: Mediators of Immediate Hypersensitivity Reactions and Inflammation." Science **220**(4597): 568-575.
San Pietro, E., M. Capestrano, E. V. Polishchuk, A. DiPentima, A. Trucco, P. Zizza, S. Mariggiò, T. Pulvirenti, M. Sallese, S. Tete, A. A. Mironov, C. C. Leslie, D. Corda, A. Luini and R. S. Polishchuk (2009). "Group IV phospholipase A(2)alpha controls the formation of inter-cisternal continuities involved in intra-Golgi transport." PLoS Biol **7**(9): e1000194.
Sarmento, M. J., J. C. Ricardo, M. Amaro and R. Šachl (2020). "Organization of gangliosides into membrane nanodomains." FEBS Lett **594**(22): 3668-3697.
Saunders, C. A., R. Majumdar, Y. Molina, B. C. Subramanian and C. A. Parent (2019). "Genetic manipulation of PLB-985 cells and quantification of chemotaxis using the underagarose assay." Methods Cell Biol **149**: 31-56.
Saunders, C. A. and C. A. Parent (2020). "Emerging roles for the nucleus during neutrophil signal relay and NETosis." Curr Opin Cell Biol **62**: 135-143.
Schievella, A. R., M. K. Regier, W. L. Smith and L. L. Lin (1995). "Calcium-mediated translocation of cytosolic phospholipase A2 to the nuclear envelope and endoplasmic reticulum." J Biol Chem **270**(51): 30749-30754.
Schmidt, J. A. and W. J. Brown (2009). "Lysophosphatidic acid acyltransferase 3 regulates Golgi complex structure and function." J Cell Biol **186**(2): 211-218.
Schuck, S., M. Honsho, K. Ekroos, A. Shevchenko and K. Simons (2003). "Resistance of cell membranes to different detergents." Proc Natl Acad Sci U S A **100**(10): 5795-5800.
Schwab, J. M., N. Chiang, M. Arita and C. N. Serhan (2007). "Resolvin E1 and protectin D1 activate inflammation-resolution programmes." Nature **447**(7146): 869-874.

Scott, W. A., J. M. Zrike, A. L. Hamill, J. Kempe and Z. A. Cohn (1980). "Regulation of arachidonic acid metabolites in macrophages." Journal of Experimental Medicine **152**(2): 324-335.
Serezani, C. H., M. Divangahi and M. Peters-Golden (2023). "Leukotrienes in Innate Immunity: Still Underappreciated after All These Years?" J Immunol **210**(3): 221-227.
Serhan, C. N., N. Chiang and T. E. Van Dyke (2008). "Resolving inflammation: dual anti-inflammatory and pro-resolution lipid mediators." Nat Rev Immunol **8**(5): 349-361.
Shah, B., N. Burg and M. H. Pillinger (2017). Chapter 11 - Neutrophils. Kelley and Firestein's Textbook of Rheumatology (Tenth Edition). G. S. Firestein, R. C. Budd, S. E. Gabriel, I. B. McInnes and J. R. O'Dell, Elsevier**:** 169-188.e163.
Sharp, J. D., D. L. White, X. G. Chiou, T. Goodson, G. C. Gamboa, D. McClure, S. Burgett, J. Hoskins, P. L. Skatrud, J. R. Sportsman and et al. (1991). "Molecular cloning and expression of human Ca(2+)-sensitive cytosolic phospholipase A2." J Biol Chem **266**(23): 14850-14853.
Song, L., X. Tian and R. Schekman (2021). "Extracellular vesicles from neurons promote neural induction of stem cells through cyclin D1." J Cell Biol **220**(9).
Stahelin, R. V., P. Subramanian, M. Vora, W. Cho and C. E. Chalfant (2007). "Ceramide-1-phosphate binds group IVA cytosolic phospholipase a2 via a novel site in the C2 domain." J Biol Chem **282**(28): 20467-20474.
Subbarao, K., V. R. Jala, S. Mathis, J. Suttles, W. Zacharias, J. Ahamed, H. Ali, M. T. Tseng and B. Haribabu (2004). "Role of leukotriene B4 receptors in the development of atherosclerosis: potential mechanisms." Arterioscler Thromb Vasc Biol **24**(2): 369-375.
Subramanian, B. C., R. Majumdar and C. A. Parent (2017). "The role of the LTB4-BLT1 axis in chemotactic gradient sensing and directed leukocyte migration." Semin Immunol **33**: 16-29.
Subramanian, B. C., N. Melis, D. Chen, W. Wang, D. Gallardo, R. Weigert and C. A. Parent (2020). "The LTB4-BLT1 axis regulates actomyosin and β2-integrin dynamics during neutrophil extravasation." J Cell Biol **219**(10).
Subramanian, B. C., K. Moissoglu and C. A. Parent (2018). "The LTB4-BLT1 axis regulates the polarized trafficking of chemoattractant GPCRs during neutrophil chemotaxis." J Cell Sci **131**(18).
Subramanian, P., R. V. Stahelin, Z. Szulc, A. Bielawska, W. Cho and C. E. Chalfant (2005). "Ceramide 1-phosphate acts as a positive allosteric activator of group IVA cytosolic phospholipase A2 alpha and enhances the interaction of the enzyme with phosphatidylcholine." J Biol Chem **280**(18): 17601-17607.
Sun, M., R. Wang and Q. Han (2017). "Inhibition of leukotriene B4 receptor 1 attenuates lipopolysaccharide-induced cardiac dysfunction: role of AMPK-regulated mitochondrial function." Sci Rep **7**: 44352.
Suram, S., L. J. Silveira, S. Mahaffey, G. D. Brown, J. V. Bonventre, D. L. Williams, N. A. R. Gow, D. L. Bratton, R. C. Murphy and C. C. Leslie (2013). "Cytosolic Phospholipase A(2)α and Eicosanoids Regulate Expression of Genes in Macrophages Involved in Host Defense and Inflammation." PLoS ONE **8**(7): e69002.
Tallima, H. and R. El Ridi (2018). "Arachidonic acid: Physiological roles and potential health benefits - A review." J Adv Res **11**: 33-41.
Tang, L. (2019). "Investigating heterogeneity in HeLa cells." Nature Methods **16**(4): 281-281.
Terradas, M., M. Martín, L. Hernández, L. Tusell and A. Genescà (2012). "Nuclear envelope defects impede a proper response to micronuclear DNA lesions." Mutat Res **729**(1-2): 35-40.

Terradas, M., M. Martín, L. Tusell and A. Genescà (2009). "DNA lesions sequestered in micronuclei induce a local defective-damage response." DNA Repair (Amst) **8**(10): 1225-1234.
Théry, C., K. W. Witwer, E. Aikawa, M. J. Alcaraz, J. D. Anderson, R. Andriantsitohaina, A. Antoniou, T. Arab, F. Archer, G. K. Atkin-Smith, D. C. Ayre, J. M. Bach, D. Bachurski, H. Baharvand, L. Balaj, S. Baldacchino, N. N. Bauer, A. A. Baxter, M. Bebawy, C. Beckham, A. Bedina Zavec, A. Benmoussa, A. C. Berardi, P. Bergese, E. Bielska, C. Blenkiron, S. Bobis-Wozowicz, E. Boilard, W. Boireau, A. Bongiovanni, F. E. Borràs, S. Bosch, C. M. Boulanger, X. Breakefield, A. M. Breglio, M. Brennan, D. R. Brigstock, A. Brisson, M. L. Broekman, J. F. Bromberg, P. Bryl-Górecka, S. Buch, A. H. Buck, D. Burger, S. Busatto, D. Buschmann, B. Bussolati, E. I. Buzás, J. B. Byrd, G. Camussi, D. R. Carter, S. Caruso, L. W. Chamley, Y. T. Chang, C. Chen, S. Chen, L. Cheng, A. R. Chin, A. Clayton, S. P. Clerici, A. Cocks, E. Cocucci, R. J. Coffey, A. Cordeiro-da-Silva, Y. Couch, F. A. Coumans, B. Coyle, R. Crescitelli, M. F. Criado, C. D'Souza-Schorey, S. Das, A. Datta Chaudhuri, P. de Candia, E. F. De Santana, O. De Wever, H. A. Del Portillo, T. Demaret, S. Deville, A. Devitt, B. Dhondt, D. Di Vizio, L. C. Dieterich, V. Dolo, A. P. Dominguez Rubio, M. Dominici, M. R. Dourado, T. A. Driedonks, F. V. Duarte, H. M. Duncan, R. M. Eichenberger, K. Ekström, S. El Andaloussi, C. Elie-Caille, U. Erdbrügger, J. M. Falcón-Pérez, F. Fatima, J. E. Fish, M. Flores-Bellver, A. Försönits, A. Frelet-Barrand, F. Fricke, G. Fuhrmann, S. Gabrielsson, A. Gámez-Valero, C. Gardiner, K. Gärtner, R. Gaudin, Y. S. Gho, B. Giebel, C. Gilbert, M. Gimona, I. Giusti, D. C. Goberdhan, A. Görgens, S. M. Gorski, D. W. Greening, J. C. Gross, A. Gualerzi, G. N. Gupta, D. Gustafson, A. Handberg, R. A. Haraszti, P. Harrison, H. Hegyesi, A. Hendrix, A. F. Hill, F. H. Hochberg, K. F. Hoffmann, B. Holder, H. Holthofer, B. Hosseinkhani, G. Hu, Y. Huang, V. Huber, S. Hunt, A. G. Ibrahim, T. Ikezu, J. M. Inal, M. Isin, A. Ivanova, H. K. Jackson, S. Jacobsen, S. M. Jay, M. Jayachandran, G. Jenster, L. Jiang, S. M. Johnson, J. C. Jones, A. Jong, T. Jovanovic-Talisman, S. Jung, R. Kalluri, S. I. Kano, S. Kaur, Y. Kawamura, E. T. Keller, D. Khamari, E. Khomyakova, A. Khvorova, P. Kierulf, K. P. Kim, T. Kislinger, M. Klingeborn, D. J. Klinke, 2nd, M. Kornek, M. M. Kosanović, F. Kovács Á, E. M. Krämer-Albers, S. Krasemann, M. Krause, I. V. Kurochkin, G. D. Kusuma, S. Kuypers, S. Laitinen, S. M. Langevin, L. R. Languino, J. Lannigan, C. Lässer, L. C. Laurent, G. Lavieu, E. Lázaro-Ibáñez, S. Le Lay, M. S. Lee, Y. X. F. Lee, D. S. Lemos, M. Lenassi, A. Leszczynska, I. T. Li, K. Liao, S. F. Libregts, E. Ligeti, R. Lim, S. K. Lim, A. Linē, K. Linnemannstöns, A. Llorente, C. A. Lombard, M. J. Lorenowicz, M. Lörincz Á, J. Lötvall, J. Lovett, M. C. Lowry, X. Loyer, Q. Lu, B. Lukomska, T. R. Lunavat, S. L. Maas, H. Malhi, A. Marcilla, J. Mariani, J. Mariscal, E. S. Martens-Uzunova, L. Martin-Jaular, M. C. Martinez, V. R. Martins, M. Mathieu, S. Mathivanan, M. Maugeri, L. K. McGinnis, M. J. McVey, D. G. Meckes, Jr., K. L. Meehan, I. Mertens, V. R. Minciacchi, A. Möller, M. Møller Jørgensen, A. Morales-Kastresana, J. Morhayim, F. Mullier, M. Muraca, L. Musante, V. Mussack, D. C. Muth, K. H. Myburgh, T. Najrana, M. Nawaz, I. Nazarenko, P. Nejsum, C. Neri, T. Neri, R. Nieuwland, L. Nimrichter, J. P. Nolan, E. N. Nolte-'t Hoen, N. Noren Hooten, L. O'Driscoll, T. O'Grady, A. O'Loghlen, T. Ochiya, M. Olivier, A. Ortiz, L. A. Ortiz, X. Osteikoetxea, O. Østergaard, M. Ostrowski, J. Park, D. M. Pegtel, H. Peinado, F. Perut, M. W. Pfaffl, D. G. Phinney, B. C. Pieters, R. C. Pink, D. S. Pisetsky, E. Pogge von Strandmann, I. Polakovicova, I. K. Poon, B. H. Powell, I. Prada, L. Pulliam, P. Quesenberry, A. Radeghieri, R. L. Raffai, S. Raimondo, J. Rak, M. I. Ramirez, G. Raposo, M. S. Rayyan, N. Regev-Rudzki, F. L. Ricklefs, P. D. Robbins, D. D. Roberts, S. C. Rodrigues, E. Rohde, S. Rome, K. M. Rouschop, A. Rughetti, A. E. Russell, P. Saá, S. Sahoo, E. Salas-Huenuleo, C. Sánchez, J. A. Saugstad, M. J. Saul, R. M. Schiffelers, R. Schneider, T. H. Schøyen, A. Scott, E. Shahaj, S.

Sharma, O. Shatnyeva, F. Shekari, G. V. Shelke, A. K. Shetty, K. Shiba, P. R. Siljander, A. M. Silva, A. Skowronek, O. L. Snyder, 2nd, R. P. Soares, B. W. Sódar, C. Soekmadji, J. Sotillo, P. D. Stahl, W. Stoorvogel, S. L. Stott, E. F. Strasser, S. Swift, H. Tahara, M. Tewari, K. Timms, S. Tiwari, R. Tixeira, M. Tkach, W. S. Toh, R. Tomasini, A. C. Torrecilhas, J. P. Tosar, V. Toxavidis, L. Urbanelli, P. Vader, B. W. van Balkom, S. G. van der Grein, J. Van Deun, M. J. van Herwijnen, K. Van Keuren-Jensen, G. van Niel, M. E. van Royen, A. J. van Wijnen, M. H. Vasconcelos, I. J. Vechetti, Jr., T. D. Veit, L. J. Vella, É. Velot, F. J. Verweij, B. Vestad, J. L. Viñas, T. Visnovitz, K. V. Vukman, J. Wahlgren, D. C. Watson, M. H. Wauben, A. Weaver, J. P. Webber, V. Weber, A. M. Wehman, D. J. Weiss, J. A. Welsh, S. Wendt, A. M. Wheelock, Z. Wiener, L. Witte, J. Wolfram, A. Xagorari, P. Xander, J. Xu, X. Yan, M. Yáñez-Mó, H. Yin, Y. Yuana, V. Zappulli, J. Zarubova, V. Žėkas, J. Y. Zhang, Z. Zhao, L. Zheng, A. R. Zheutlin, A. M. Zickler, P. Zimmermann, A. M. Zivkovic, D. Zocco and E. K. Zuba-Surma (2018). "Minimal information for studies of extracellular vesicles 2018 (MISEV2018): a position statement of the International Society for Extracellular Vesicles and update of the MISEV2014 guidelines." J Extracell Vesicles **7**(1): 1535750.

Tian, W., G. T. Wijewickrama, J. H. Kim, S. Das, M. P. Tun, N. Gokhale, J. W. Jung, K. P. Kim and W. Cho (2008). "Mechanism of regulation of group IVA phospholipase A2 activity by Ser727 phosphorylation." J Biol Chem **283**(7): 3960-3971.

Tomić, M., A. Micov, U. Pecikoza and R. Stepanović-Petrović (2017). Chapter 1 - Clinical Uses of Nonsteroidal Anti-Inflammatory Drugs (NSAIDs) and Potential Benefits of NSAIDs Modified-Release Preparations. Microsized and Nanosized Carriers for Nonsteroidal Anti-Inflammatory Drugs. B. Čalija. Boston, Academic Press**:** 1-29.

Trajkovic, K., C. Hsu, S. Chiantia, L. Rajendran, D. Wenzel, F. Wieland, P. Schwille, B. Brügger and M. Simons (2008). "Ceramide triggers budding of exosome vesicles into multivesicular endosomes." Science **319**(5867): 1244-1247.

Truckenbrodt, S., C. Sommer, S. O. Rizzoli and J. G. Danzl (2019). "A practical guide to optimization in X10 expansion microscopy." Nat Protoc **14**(3): 832-863.

Tucker, D. E., M. Ghosh, F. Ghomashchi, R. Loper, S. Suram, B. S. John, M. Girotti, J. G. Bollinger, M. H. Gelb and C. C. Leslie (2009). "Role of Phosphorylation and Basic Residues in the Catalytic Domain of Cytosolic Phospholipase A(2)α in Regulating Interfacial Kinetics and Binding and Cellular Function." The Journal of Biological Chemistry **284**(14): 9596-9611.

Tucker, K. A., M. B. Lilly, L. Heck, Jr. and T. A. Rado (1987). "Characterization of a new human diploid myeloid leukemia cell line (PLB-985) with granulocytic and monocytic differentiating capacity." Blood **70**(2): 372-378.

van Niel, G., G. D'Angelo and G. Raposo (2018). "Shedding light on the cell biology of extracellular vesicles." Nat Rev Mol Cell Biol **19**(4): 213-228.

Venturini, V., F. Pezzano, F. Català Castro, H. M. Häkkinen, S. Jiménez-Delgado, M. Colomer-Rosell, M. Marro, Q. Tolosa-Ramon, S. Paz-López, M. A. Valverde, J. Weghuber, P. Loza-Alvarez, M. Krieg, S. Wieser and V. Ruprecht (2020). "The nucleus measures shape changes for cellular proprioception to control dynamic cell behavior." Science **370**(6514).

Verweij, F. J., M. P. Bebelman, C. R. Jimenez, J. J. Garcia-Vallejo, H. Janssen, J. Neefjes, J. C. Knol, R. de Goeij-de Haas, S. R. Piersma, S. R. Baglio, M. Verhage, J. M. Middeldorp, A. Zomer, J. van Rheenen, M. G. Coppolino, I. Hurbain, G. Raposo, M. J. Smit, R. F. G. Toonen, G. van Niel and D. M. Pegtel (2018). "Quantifying exosome secretion from single cells reveals a modulatory role for GPCR signaling." J Cell Biol **217**(3): 1129-1142.

Ward, K. E., N. Bhardwaj, M. Vora, C. E. Chalfant, H. Lu and R. V. Stahelin (2013). "The molecular basis of ceramide-1-phosphate recognition by C2 domains." J Lipid Res **54**(3): 636-648.
Ward, K. E., J. P. Ropa, E. Adu-Gyamfi and R. V. Stahelin (2012). "C2 domain membrane penetration by group IVA cytosolic phospholipase A(2) induces membrane curvature changes." J Lipid Res **53**(12): 2656-2666.
Ward, K. E., J. P. Ropa, E. Adu-Gyamfi and R. V. Stahelin (2012). "C2 domain membrane penetration by group IVA cytosolic phospholipase A_2 induces membrane curvature changes." J Lipid Res **53**(12): 2656-2666.
Ward, K. E., R. Sengupta, J. P. Ropa, S. Amiar and R. V. Stahelin (2020). "The Cytosolic Phospholipase A(2)α N-terminal C2 Domain Binds and Oligomerizes on Membranes with Positive Curvature." Biomolecules **10**(4).
Willms, E., H. J. Johansson, I. Mäger, Y. Lee, K. E. Blomberg, M. Sadik, A. Alaarg, C. I. Smith, J. Lehtiö, S. El Andaloussi, M. J. Wood and P. Vader (2016). "Cells release subpopulations of exosomes with distinct molecular and biological properties." Sci Rep **6**: 22519.
Wong , D. A., Y. Kita , N. Uozumi and T. Shimizu (2002). "Discrete Role for Cytosolic Phospholipase A2α in Platelets : Studies Using Single and Double Mutant Mice of Cytosolic and Group IIA Secretory Phospholipase A2." Journal of Experimental Medicine **196**(3): 349-357.
Wu, T., C. W. Angus, X. L. Yao, C. Logun and J. H. Shelhamer (1997). "P11, a unique member of the S100 family of calcium-binding proteins, interacts with and inhibits the activity of the 85-kDa cytosolic phospholipase A2." J Biol Chem **272**(27): 17145-17153.
Yonker, L. M., M. A. Pazos, B. B. Lanter, H. Mou, K. K. Chu, A. D. Eaton, J. V. Bonventre, G. J. Tearney, J. Rajagopal and B. P. Hurley (2017). "Neutrophil-Derived Cytosolic PLA2alpha Contributes to Bacterial-Induced Neutrophil Transepithelial Migration." J Immunol **199**(8): 2873-2884.
Yun, B., H. Lee, H. Ewing, M. H. Gelb and C. C. Leslie (2016). "Off-target effect of the cPLA2α inhibitor pyrrophenone: Inhibition of calcium release from the endoplasmic reticulum." Biochem Biophys Res Commun **479**(1): 61-66.
Zizza, P., C. Iurisci, M. Bonazzi, P. Cossart, C. C. Leslie, D. Corda and S. Mariggiò (2012). "Phospholipase A₂IVα Regulates Phagocytosis Independent of Its Enzymatic Activity *." Journal of Biological Chemistry **287**(20): 16849-16859.